OPTIMIZATION OF LUMINESCENT FEATURES IN MULTICOLOR EMITTING RARE EARTH DOPED ALKALINE EARTH VANADATE PHOSPHOR FOR SOLID STATE LIGHTING APPLICATIONS

THESIS

Submitted to

Delhi Technological University

in partial fulfilment of the requirements for the degree of

DOCTOR OF PHILOSOPHY
in

APPLIED PHYSICS

by

HARPREET KAUR
Reg. No. 2K16/Ph.D./AP/06

Under the Supervision
of

Dr. M. JAYASIMHADRI
Assistant Professor

DEPARTMENT OF APPLIED PHYSICS
DELHI TECHNOLOGICAL UNIVERSITY
DELHI-110 042, INDIA

OCTOBER 2021

This thesis is dedicated to

my lovely mother who has always been a

source of inspiration & support in my life

DELHI TECHNOLOGICAL UNIVERSITY

Formerly Delhi College of Engineering

(Govt. of National Capital Territory of Delhi)

Shahbad Daulatpur, Bawana Road, Delhi-110 042

CERTIFICATE

This is to certify that the thesis entitled ***"Optimization of Luminescent Features in Multicolor Emitting Rare Earth Doped Alkaline Earth Vanadate Phosphor for Solid State Lighting Applications"*** is being submitted by ***Ms. Harpreet Kaur*** with registration number ***2K16/Ph.D./AP/06*** to the Delhi Technological University, Delhi for the award of degree of Doctor of Philosophy in Applied Physics. The work embodied in this thesis is a record of bonafide research work carried out by me in Department of Applied Physics, Delhi Technological University, Delhi under the supervision of ***Dr. M. Jayasimhadri***. It is further certified that the work embodied in this thesis has neither been partially nor fully submitted to any other university or institution for the award of any degree or diploma.

Harpreet Kaur

Harpreet Kaur
Research Scholar
Reg. No. 2K16/Ph.D./AP/06

This is to certify that the above statement made by the candidate is correct to the best of our knowledge.

07/10/2021

Dr. M. Jayasimhadri
Supervisor & Assistant professor
Department of Applied Physics
Delhi Technological University
Delhi-110 042, India

Rinku
7th October 2021

Prof. Rinku Sharma
Head, Department of Applied Physics
Delhi Technological University
Delhi-110 042, India

ACKNOWLEDGEMENTS

Gratitude is the most exquisite form of courtesy which strengthens the voice of hope and unlocks the fullness of life. Though these humble words, articulations and gratitude cannot fully convey the deep feelings of my heart. But on the occasion of summing up all the work done in last five years at Delhi Technological University (DTU) and specifically within Luminescent Materials Research Lab (LMRL), I take the opportunity to express my sincere thanks to all who have accompanied, encouraged and supported me. Prior to all, I want to offer this endeavour to the ***Almighty God****, for the wisdom he bestowed upon me, giving me strength to carry out the present study successfully and for sustaining my efforts which many a times did oscillate. The Almighty God is obviously the one, who has always guided me to work on the right part of life.*

I feel great honor in expressing an immense gratitude towards my supervisor, ***Dr. M. Jayasimhadri****, Department of Applied Physics, DTU, for his enlightened guidance and unremitting encouragement throughout the course of my study. I am thankful to him for his advices, knowledge augmenting discussion, quality enhancing inputs, constructive criticism and constant motivation. His immense knowledge of the subject, analytic gaze, farsightedness and perseverance were a constant source of inspiration during the course of this thesis work. Above all, the research ethics I learnt from him will always be a guiding light for me in choosing and practicing true ways of sciences throughout my life and career.*

I express reverence towards Honorable Vice Chancellor, ***Prof. Yogesh Singh*** *and* ***Prof. Rinku Sharma****, Head, Department of Applied Physics, DTU for providing the basic infrastructural facilities and timely quintessential support to carry out the research work. My heartfelt recognitions for* ***Prof. S.C. Sharma****, DRC Chairman, Department of Applied Physics, DTU as well as my SRC and DRC committee members for their enduring support and valuable suggestions for the thesis.*

I am genuinely grateful to ***Dr. D. Haranath****, Associate Professor, National Institute of Technology (NIT), Warangal,* ***Dr. J. Suresh Kumar****, University of Aveiro, Portugal and* ***Dr. Govind Gupta****, Senior Principal Scientist, CSIR-National Physical Laboratory (NPL), New Delhi for providing necessary facilities, giving valuable suggestions and discussion.*

My deepest regards to ***Prof. A. S. Rao*** *for his timely advice and support. I owe my sincere gratitude towards all the* ***faculty members*** *of Department of Applied Physics for their*

help during the research work. I am also grateful to ***Advanced Instrumentation Centre (AIC), technical and non-technical staff*** *for their timely support and cooperation whenever required.*

I wish to sincerely thank my former and present lab mates, ***Dr. Amit K. Vishwakarma****,* ***Dr. Kaushal Jha****,* ***Dr. Sumandeep Kaur****,* ***Dr. Shankar Subramanian****,* ***Mr. Mukesh K. Sahu****,* ***Ms. Deepali****,* ***Mr. Vikas****,* ***Mr. Indrajeet Maurya,*** *whose support helped me in accomplishment of the work. It's my pleasure to thank my colleagues from* ***MASRL*** *Lab, batchmates (****Mr. Abhishek Bhardwaj, Ms. Ardaman Kaur, Mrs. Umang Sharma and Ms. Pooja Chauhan****) and all other scholars of Department of Applied Physics for their support and enjoyable company. My special thanks for* ***Dr. Nishant Shankhwar****,* ***Dr. Kamal Kishor*** *and* ***Dr. Lucky Krishnia*** *for keeping the environment cheerful and motivating me.*

I wish to acknowledge the gratifying company and suitable help rendered by ***Mr. Gaurav Gupta****,* ***Mr. Vishu Chauhan, Ms. Ritu Verma****,* ***Mr. Vishnu Vikesh Jaiswal****,* ***Mr. Birendra****,* ***Mr. Balram Fageria*** *and* ***Dr. Lalit Goswami*** *during this tenure.*

This endeavour would not been a success without the persistent support and encouragement of my dearest friends, ***Ms. Neha Bansal****,* ***Mr. Dipankar Dhar, Dr. Divya Sachdeva****,* ***Ms. Vandana Sahdev****,* ***Dr. Naushad Ansari****,* ***Mr. Ram Niwas Tiwary, Ms. Isha Verma*** *and* ***Mrs. Surbhi Arora****. I am glad to thank for their extended support and earnest concern that help me to tide over occasional moments of stress at various stages of this tenure.*

*I am deeply indebted to my parents (****Mrs. Manjeet Kaur and S. Gurmeet Singh****) and lovely sister* ***Ms. Paramjeet Kaur*** *for always having faith in me and motivating me for perseverance during tough times. Especially, the love, pamper, support, encouragement, understanding and blessing of my mother that gave me the strength to take up this work and complete it to the best of my ability.*

I wish to express my sincere gratitude towards ***Delhi Technological University*** *for extending all the necessary facilities and also for providing financial assistance in the form of Junior Research Fellowship and Senior Research Fellowship during the period of my Ph.D. course. I extend my gratitude to staff in Administration, Accounts, Store & Purchase, Library, and Computer Centre for their help and services during this tenure.*

Finally, I wish to thank one and all for their timely interference into my life and making it happier and meaningful!!

Harpreet Kaur

Harpreet Kaur

LIST OF PUBLICATIONS

Thesis Work:

1. **Harpreet Kaur**, M. Jayasimhadri, "Color tunable photoluminescence properties in Eu^{3+} doped calcium bismuth vanadate phosphors for luminescent devices", **Ceramics International** 45 (2019) 15385-15393 **(Impact Factor: 4.527)**.

2. **Harpreet Kaur**, M. Jayasimhadri, "Optimization of structural and luminescent properties with intense red emitting thermally stable Sm^{3+} doped $CaBiVO_5$ phosphors for w-LED applications", **Optical Materials** 107 (2020) 110119 **(Impact Factor: 3.080)**.

3. **Harpreet Kaur**, M. Jayasimhadri, "Development of deep red emitting $CaBiVO_5$:Pr^{3+} phosphor for multifunctional optoelectronic applications", **Journal of the American Ceramic Society** 104 (2021) 5764-5775. **(Impact Factor: 3.784)**.

4. **Harpreet Kaur**, M. Jayasimhadri, "Spectroscopic and color tunable studies in Dy^{3+}/Eu^{3+} co-doped calcium-bismuth-vanadate phosphor for lighting applications", **Solid State Sciences** (communicated-2021) **(Impact Factor: 3.059).**

Other than thesis work:

1. **Harpreet Kaur**, M. Jayasimhadri, Mukesh K. Sahu, P. Koteswara Rao, N. S. Reddy, "Synthesis of orange emitting Sm^{3+} doped sodium calcium silicate phosphor by sol-gel method for photonic device applications", **Ceramics International** 46 (2020) 26434-26439 (**Impact Factor: 4.527**).

2. Mukesh K. Sahu, **Harpreet Kaur**, B. V. Ratnam, J. Suresh Kumar, M. Jayasimhadri, "Structural and spectroscopic characteristics of thermally stable Eu^{3+} activated barium zinc

orthophosphate phosphor for white LEDs", **Ceramics International** 46 (2020) 26410-26415 (**Impact Factor: 4.527**).

3. Deepali, Ruchira Bisi, Vandana, **Harpreet Kaur**, M. Jayasimhadri, "Structural and spectroscopic properties of Sm-doped $NaBaB_9O_{15}$ phosphor for optoelectronic device applications", **Journal of Materials Science: Materials in Electronics** 32 (2021) 1650-1658 **(Impact Factor: 2.487).**

4. Subhajit Pradhan, **Harpreet Kaur**, M. Jayasimhadri, "Photoluminescence and thermal sensing properties of Er^{3+} doped silicate based phosphors for multifunctional optoelectronic device applications", **Ceramics International (In press; Published online-2021) (Impact Factor: 4.527).**

5. **Harpreet Kaur**, Vishesh Tiku, Aditya Prasad, Y. Abhishek Singh, Vishnu Vikesh Jaiswal, M. Jayasimhadri, D. Haranath, "Luminescent and Colorimetric properties of the sol-gel derived mono-phase Dy^{3+} doped silicate based phosphor for w-LED applications", **Journal of Sol-Gel Science and Technology** (communicated-2021) **(Impact Factor: 2.326)**.

ABSTRACT

Recent advances in solid state lighting (SSL) technology have encouraged its utilization in versatile applications. SSL technology based on phosphor converted light emitting diodes (pc-LEDs) are acting potentially as a substitute for traditional incandescent and fluorescent lamps on an account of their unprecedented luminous efficiency, low energy consumption, less emission of harmful gases, high brightness, compact design, fast switching and long working lifetimes. The pc-LEDs utilize phosphors coated on the LED chip capable of emitting light in desirable spectral regions upon an appropriate excitation. In the light of the above mentioned advantages, pc-LEDs are believed to be the next generation SSL technology and will bring a revolutionary changes in the lighting industry. For example, the white pc-LEDs have been the most preferred lighting devices for general illumination due to effective energy utilization, long lifetime, safety and so on. Moreover, pc-LEDs can be harnessed for indoor agricultural lighting owing to their excellence in controlling the spectral composition and lighting intensity to mimic the changes of sunlight during the day. Therefore, all the above mentioned fascinating features like effective energy saving and desirable light emission have enabled pc-LEDs to become economically feasible choice for general illumination and large scale indoor agricultural lighting applications around the corners of the world.

The phosphor based w-LEDs can be developed by (i) coating of appropriate mixture of red, green and blue (RGB) phosphors excited with UV LED chip (ii) single yellow phosphor by a blue LED chip. However, reabsorption of blue color by RG phosphors in the former approach and lack of red component in later approach may lead to shortcomings like low color saturation, deteriorated color rendering index (CRI) and low color temperature stability. To overcome the above mentioned shortcomings, it is necessary to develop single phase phosphor doped with appropriate combination of rare earth ions (such as Dy^{3+}/Eu^{3+}, Tb^{3+}/Eu^{3+}, Tb^{3+}/Sm^{3+}, Dy^{3+}/Sm^{3+} etc.) providing white light emission via energy transfer or new red

phosphor for the improvement of performance factors like luminous efficiency, CRI and correlated color temperature (CCT). Further, for plant growth under controlled environment fitted with smart pc-LEDs, it is necessary to conduct a widespread research for deep-red, far-red and blue light emitting phosphors that can be utilised to best drive photosynthetic metabolism and photo-morphogenesis as per the literature survey. Therefore, the ascending demand of energetically efficient lighting devices for general illumination and plant growth applications has led to a significant interest in the development of novel high quality phosphors with superior brightness, multiple emission color and excellent color purity. Besides lighting, the phosphors facilitate their utilization in diverse applications such as solar cells, bio-sensing and other optoelectronic devices due to their versatile physical, chemical and luminescent properties. In general, phosphor consisting of a host matrix (crystalline host) and an activator (luminescent center) have been pondered as a technologically significant components for the development of w-LEDs and agricultural lighting systems. In the past few decades, inorganic phosphors activated with rare earth (RE) ions have remained the prevalent protocol for fabricating pc-LEDs due to unique luminescence properties of RE ions. In such phosphors, the intermixing of oxygen atomic orbitals of host with orbitals of RE ion creates a specific crystal field environment around it such that transitions between incompletely filled 4f energy levels of RE ions deliver distinctive luminescence features. Also, the efficient energy transfer from the host crystal to the RE activators have been investigated to comprehend interesting optical phenomena. Among all the various inorganic oxides, vanadates have attracted acquiescent utilization in the wide-spread of luminescent device applications due to their wide-range of excitation wavelengths with abundant luminous colour, good physical and chemical stability. In addition, the vanadate materials are cost-effective and their preparation methods are energy efficient. The vanadate based phosphors give a broadband emission originating from inherent $[VO_4]^{3-}$ group. The broadband emission in the visible range by vanadate hosts can bring

improvement in CRI and CCT values. Recent investigations have been established the possibility of achieving tunable visible emissions in RE activated vanadate phosphors via controlling $[VO_4]^{3-}$ to RE ions energy transfer. To harness the above mentioned precedencies, an investigation on a new ternary vanadate ($CaBiVO_5$) phosphor doped with RE ions has been done for general and agricultural lighting applications. By incorporating suitable RE ions, the present host ($CaBiVO_5$) can be tuned to emit different colors in the visible region suitable for pc-LEDs used in general illumination and agricultural lighting applications.

Based on the extensive structural, morphological and photoluminescence characterizations, the outcome of the research work for accomplishing the research objectives has been organized in seven chapters. The brief summary of each chapter is as follows:

Chapter 1 highlights the brief history, motivation, an outlook on the recent developments, potential challenges and great opportunities in white light generation and agricultural lighting. This chapter explains the basic concepts related to luminescence, spectroscopic features of RE ions, theoretical models implemented for examining the observed spectral data, and possible energy transfer processes. This chapter also present a brief viewpoint on the various characteristics and indices such as chromaticity coordinates, color purity, CCT and activation energy describing the color quality, thermal stability and performance of pc-LEDs. The importance of the present work and selected vanadate host have been discussed briefly in this chapter. At the last, the objectives of the thesis based on literature review have been included.

Chapter 2 makes a thorough discussion about the different synthesis methods opted for the synthesis of single phase calcium bismuth vanadate ($CaBiVO_5$: CBV) phosphors activated with different RE ions (Eu^{3+}, Sm^{3+}, Pr^{3+} and Dy^{3+}). It also explicates the basic principle and working of experimental techniques employed to explore structural, morphological, optical and luminescent properties of CBV phosphors. The thermal and structural properties are studied by thermogravimetric analysis (TGA) and X-ray Diffraction (XRD) method, respectively. The

scanning electron microscopy (SEM) reveals the morphology of the as synthesized phosphors. The optical properties are determined from diffuse-reflectance (DR) spectral measurements, while photoluminescence properties, thermal stability and decay kinetics of the CBV phosphors doped with different RE ions were investigated using spectrofluorophotometer. All these characterization techniques have been discussed in this chapter.

Chapter 3 describes about the synthesis of single phase Eu^{3+} activated calcium bismuth vanadate ($CaBiVO_5$) phosphors using solid state reaction method. X-ray diffraction (XRD) analysis confirms the pure phase formation and scanning electron microscope (SEM) micrographs exhibit inhomogeneous particle formation with irregular morphology of Eu^{3+} doped $CaBiVO_5$ (CBV) phosphor. The photoluminescence excitation (PLE) spectrum indicates significant absorption in the ultraviolet (UV) and near ultraviolet (n-UV) spectral regions for un-doped CBV sample, whereas Eu^{3+} doped CBV phosphors reveal various sharp absorption bands in n-UV and blue region along with host absorption bands. Trivalent europium activated CBV phosphors under 342 nm excitation exhibit dominant red emission peak at 613 nm wavelength accompanied by weak broadband originating from VO_4 groups, whereas the phosphors under 464 nm excitation, exhibit similar emission profile with most intense one centered at 613 nm by excluding host emission bands. The energy transfer mechanism and the probable cause for concentration quenching beyond 4.0 mol% of Eu^{3+} ions concentration have been discussed in detail. The CIE chromaticity coordinates for the optimized phosphor, (0.551, 0.398) and (0.639, 0.358), situated in the reddish-orange and red region under 342 and 464 nm excitations, respectively. The CIE coordinates calculated based on the emission spectra measured under 464 nm excitation are close to the commercial phosphor Y_2O_2S: Eu^{3+} (0.622, 0.351). All the above mentioned results support the utilization of Eu^{3+} doped CBV phosphor as a potential red emitting component for luminescent devices.

*The research work described in this chapter has been published in "**Ceramics International 45 (2019) 15385-15393" (Impact factor =4.527)***

Chapter 4 describes the optimization of synthesis procedure for Sm^{3+} doped $CaBiVO_5$ phosphor by preparing through it via three different synthesis methods, solid-state reaction (SR), combustion (CB) and citrate sol-gel (SG) method to enhance the luminescent properties. The pure phase formation of CBV: Sm^{3+} phosphors via diverse routes (SR, CB and SG) is confirmed as diffraction peaks for all prepared phosphors correspond to the standard data (JCPDS card no: 81-1775). The SEM results reveal that CBV: Sm^{3+} phosphors are synthesized with improved homogeneity and shape regularity at lower reaction temperature via SG method. The excitation spectra measured by monitoring the emission at 649 nm for CBV: Sm^{3+} phosphors reveal significant absorption in ultraviolet (UV), near (n)-UV and blue spectral regions. The comparative photoluminescence (PL) spectra measured under 343 nm excitation for differently synthesized CBV: Sm^{3+} phosphors, which exhibit significantly enhanced emission intensity for SG derived phosphor than other adopted methods. The PL spectra for SG derived 1.0 mol% Sm^{3+} doped CBV phosphor at λ_{ex} = 275 and 343 nm exhibit sharp peaks located at 566, 606 and 649 nm along with weak host emission broadband and for λ_{ex} = 406 nm, similar sharp peaks of Sm^{3+} transitions are observed without any host emission. Unlike mostly explored Sm^{3+} doped phosphors, emission peak in red spectral region (649 nm) is more intense as compared to the emission peak in orange region (599 nm) in the present work. The energy transfer mechanism responsible for concentration quenching in CBV phosphors is discussed in detail. The CBV: Sm^{3+} phosphors manifest color tunability from orange to orange-red region by modulating excitation from 275 nm (0.567, 0.404) to 343 nm (0.591, 0.399) and finally to 406 nm (0.620, 0.376). The temperature-dependent PL studies indicate appreciable thermal stability of as-prepared phosphor. Above mentioned results suggest that CBV: Sm^{3+} phosphor has great potential for use in white light-emitting diode (w-LED) applications.

*The research work described in this chapter has been published in "**Optical Materials 107 (2020) 110119" (Impact factor =3.080)**.*

Chapter 5 describes the citrate sol-gel synthesis of Dy^{3+} activated and Dy^{3+}/Eu^{3+} bi-activated calcium bismuth vanadate (CBV) phosphor to achieve white light emission and color-tunability. The phase purity and quasi-spherical particle with few agglomerations of the as-prepared CBV phosphors are indicated by structural and morphological characterizations, respectively. The emission spectral properties and energy transfer in Dy^{3+} doped and Dy^{3+}/Eu^{3+} co-doped CBV phosphors have been examined extensively. The Dexter and Reisfeld's approximation applied to emission spectra specifies electric dipolar-dipolar interaction to be accountable for Dy^{3+} to Eu^{3+} energy transfer. In CBV: Dy^{3+} phosphors, co-doping with Eu^{3+} ion facilitates red component that ensues warm white light emission as well as flexible color tunability with increasing Eu^{3+} ion concentration under different excitations. The significant findings like warm white light emission and controllable spectral composition in Dy^{3+}/Eu^{3+} co-doped CBV phosphor by altering the excitation energy and co-dopant (Eu^{3+}) concentration potentiate it as a suitable candidate in the domain of lighting and display devices.

*The research work described in this chapter is communicated to an Internationally reputed Journal "**Solid State Sciences (2021)" (Impact factor = 3.059)***

Chapter 6 describes about orthorhombic Pr^{3+}-doped calcium bismuth vanadate (CBV: Pr^{3+}) phosphors synthesized via citrate-gel method. The single-phase formation of CBV: Pr^{3+} phosphor has been endorsed by XRD analysis. The SEM image reveals dense-particle packaging with the quasi-spherical shape for the prepared CBV: Pr^{3+} phosphors. Under blue light excitation, CBV: Pr^{3+} phosphors exhibit intense red emission bands located at 608 and 656 nm wavelengths, overlapping with the absorption spectrum of P_R phytochrome, which is present in plants. To achieve the maximum red intensity, the Pr^{3+} ion concentration is optimized

to be 1.25 mol% in the CBV host, after which the emission intensity ceases due to the concentration quenching. Dexter's theory disclosed the possibility of d-d multipolar interaction among Pr^{3+} ions at higher concentrations of Pr^{3+} ions in the CBV host. The CIE coordinates are found to be positioned in the pure red region for CBV: Pr^{3+} phosphor and in the proximity of red-emitting commercial phosphor. The temperature dependent spectral studies manifest substantial thermal stability of the as-synthesized phosphor. All the studies mentioned above specify the tremendous potentiality of thermally stable CBV: Pr^{3+} phosphor in agricultural lighting and w-LED applications.

*The research work described in this chapter has been accepted to publish in "**Journal of the American Ceramic Society 104 (2021) 5764-5775" (Impact factor =3.784)**.*

Chapter 7 summarizes the research outcomes of the work described in chapters 3 to 6 and outline the future scope of the thesis work for the expected applications.

CONTENTS

LIST OF TABLES

LIST OF FIGURES

Chapter 1

Introduction

In recent years, phosphor based lighting technology can be envisioned in versatile applications such as white light emitting diodes (w-LEDs), display devices and indoor agricultural systems due to its enhanced luminous efficiency, better color quality, low power consumption and cost effectiveness. Moreover, this revolutionary lighting technology further demands research for the development of novel multicolor emitting phosphors featuring thermally stable luminescence. This chapter embraces the description of fundamentals accompanying luminescence mechanisms, phosphors, white light generating methods and solid state lighting technology. Moreover, the role of phosphor in agricultural lighting has been discussed. This chapter also describes the importance of chosen host material ($CaBiVO_5$) and objectives of the accomplished research work.

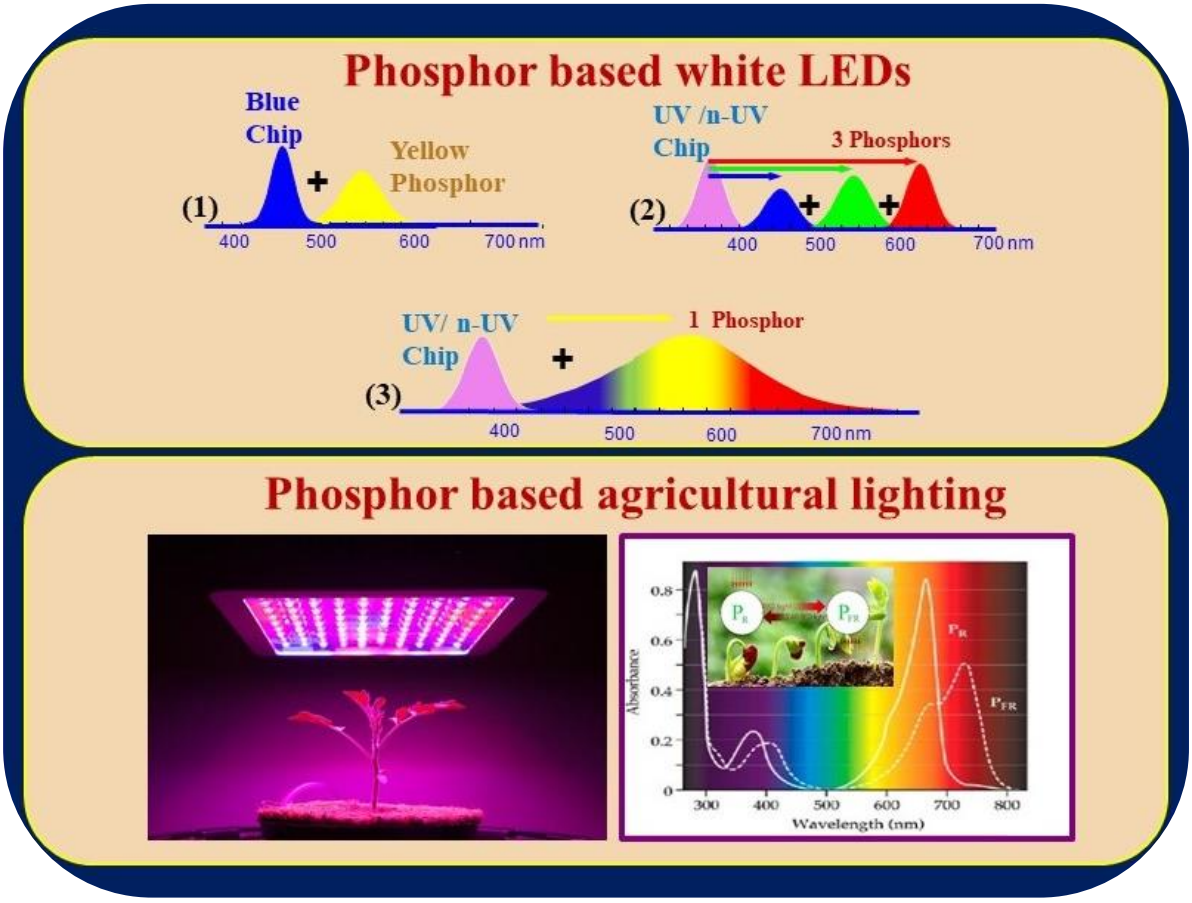

1.1. Luminescence

Artificial lighting system has always been the substantial component of life to illuminate indoor and outdoor places even beyond sunset. For lighting, initially incandescent bulbs were utilized by folks which nowadays being substituted by luminescent sources such as light emitting diodes (LEDs). The *luminescence* is a process in which a material absorbs any kind of energy from an external source and subsequently emit mostly in the visible region [1]. In case of luminescence, light has not ensued from thermal agitation of constituent particles in the material (cold process), which happens in the case of incandescence (hot process) [1, 2]. The photon emission from incandescent bulbs is due to heating of filament to a very high temperature, which leads to an enormous loss of energy that can be conserved by LEDs [3]. Moreover, the life span of these incandescent bulbs is approximately 1000 h which is very short when compared with that of LEDs (50,000 h) [4]. Luminescence occurs when the atoms of a material are excited to a higher state without the application of heat and while relaxing to its ground state, the material emit radiation preferably in the visible region [5-7]. Sometimes, the emitted radiation in luminescence might lie in near-ultraviolet (n-UV)/near infrared (NIR)/IR region.

1.1.1. Classification of Luminescence

Based on the type of excitation source, the luminescence can be categorized into different ways given as follows:

***(a) Photoluminescence*:** The emission exhibited by the atoms, which are excited by the absorption of photons is known as photoluminescence. This phenomenon is most commonly utilized in the lighting technology (i.e. fluorescent lamps and phosphor based LEDs). This process can be categorized further into two types according to lifetime of the excited level:

(i) *Fluorescence*: A process in which a rapid emission of photons occurs until the material is excited by an appropriate radiation. Customarily, the lifetime of the excited state is of the order of 10^{-8} s.

(ii) *Phosphorescence*: A process of delayed emission of photons, which continued even after the excitation source is ceased. Customarily, the decay time of excited state is greater than 10^{-3} s that may be for few hours or days. This process is also called as afterglow [8, 9].

(b) Electroluminescence: The emission triggered by the electric field is known as electroluminescence. When a forward DC voltage is applied across the *p-n* junction of a semiconductor device, the electrons are injected in the junction layer. The luminescence due to recombination of electron hole pairs in junction layer is called as electroluminescence [10, 11]. A semiconductor LED chip is a common example for electroluminescence.

(c) Cathodoluminescence: In this type of luminescence, the material exhibit emission due to striking of electrons on it. A common example is light generated at the phosphor coated surface of the television screen employed with cathode ray tube due to impacting electron beam on it. The cathodoluminescence process is contrary phenomenon of photoelectric effect.

(d) Thermoluminescence: This is basically a thermally triggered luminescence. Initially, the luminescent material is irradiated by some radiation like UV, γ, β or X-rays, which create defects that followed by thermal triggering and emit light in visible region [12, 13]. This phenomenon is exploited in dating archaeological artifacts.

(e) Chemoluminescence: The emission resulted due to chemical reaction. The chemo-luminescence reaction yield unstable products, which are called as intermediates. The

intermediates release its excess energy as light and acquires the ground state to deliver more stable products [14]. A glow tube is a basic example of this effect.

(f) ***Bioluminescence****:* It is a type of chemoluminescence, in which the emission is provided by bio-chemical reactions occurring in living organisms. In certain living organism, the biomolecules inside the cells get excited to higher states because of chemical reactions occurring inside their body. These biomolecules while relaxing to their ground state release visible light. The glow worms, luminescent jelly fishes and fire flies show bioluminescence.

(g) ***Radioluminescence:*** This type of luminescence is triggered when a substance is bombarded with an ionizing radiation (for example: alpha or beta particles). At first, the Nobel Laureate Marie and Pierre Curie had observed and reported the phenomenon of radioluminescence. The radioluminescence find applications in watches, clock dials and also in 'continuous' phosphorescent devices in which light is required to be emitted for long hours devoid of any external energy sources.

(h) ***Sonoluminescence****:* In this phenomenon, the emission of light is due to the violently collapsing bubbles in a liquid induced by sound waves of appropriate intensity.

(i) ***Mechanoluminescence:*** The emission of light due to application of some external mechanical energy on solid substances to cut, grind, rub, or compressed or deformed materials through some impulse reaction.

1.1.2. Basic concepts of photoluminescence

Photoluminescence is a phenomenon associated with absorption of energy in the form of photons by the activators and subsequent emission of light preferably in the visible region [15, 16]. The activators possess abundant energy levels to which they can be excited by absorbing photons and act as luminescence centres. Generally, the photoluminescence takes place in the following sequence:-

- Absorption of energy (photons) by the activator, raising it to an excited state.
- Relaxation of the activator to the specific emitting state.
- Subsequent emission of radiation due to de-excitation of activator to the ground state.

Initially, the incident photons are absorbed by the activators ions, which trigger the activators to their excited states/levels. The relaxation to emitting states from the higher excited levels is non-radiative and mediated by phonons (heat or lattice vibrations) as levels higher from emitting state are closely spaced such that radiative relaxation is not possible. Also, the lifetime of these excited states above emitting state is very short for emitting radiatively. Following that, the de-excitation of activator from emitting state to ground state emits photon (radiative). The emitting state is one far away from the consecutive lower state, which ceases the probability of non-radiative transition. The radiative emission leads to photoluminescence. The schematic diagram to understand photoluminescence is given in Fig. 1.1.

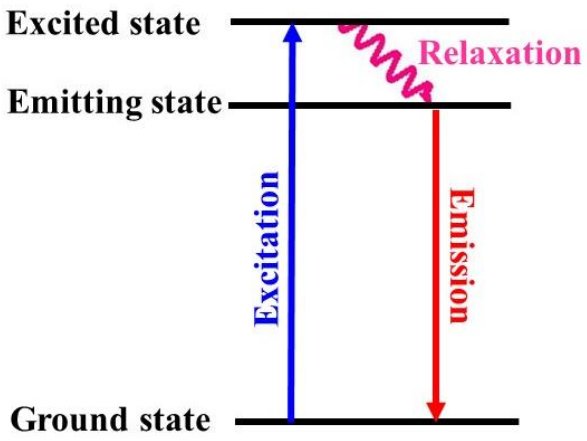

Figure 1.1. *Schematic diagram for photoluminescence*

The photoluminescence can be of two types based on the emission time even after the removal of excitation source namely (i) *fluorescence* and (ii) *phosphorescence* as discussed already in previous section. In simple terms, fluorescence is emission from the sample when it is exposed to excitation source of radiation, whereas in phosphorescence, the emission persists for long times even after the removal of the excitation source. The fluorescence is essentially

independent of temperature, whereas decay of phosphorescence exhibits strong temperature dependence [17]. As mentioned above, the process of relaxation to the ground state may be either radiative or non-radiative. The radiative process leads to emission of light while the non-radiative process does not yield any visible emission [18]. In order to generate efficient radiative emission (luminescence), it is necessary to suppress this non-radiative process. The non-radiative energy is either in the form of phonons (lattice vibrations of solid) and/or to electronic states of atoms by energy transfer (ET). Such ET processes will be discussed in the succeeding sections. As discussed above, in the process of photoluminescence, when radiation in the form of high energy photon (in UV or n-UV range) is incident on a material, some of its energy is absorbed and then material re-emit the energy in the form of low energy photons (in visible or NIR range), which is governed by Stokes law. This process is also called as down-conversion. The energy gap between excitation and emission wavelength due to prior non-radiative loss of excitation energy is called the Stokes shift. However, it may be possible that two or more low energy photons (in NIR range) are absorbed and high energy photons (in visible or UV range) are being emitted, then the process is termed as up-conversion or anti-Stokes emission [19-21]. The down-conversion and up-conversion processes are depicted in Fig. 1.2(a) and (b).

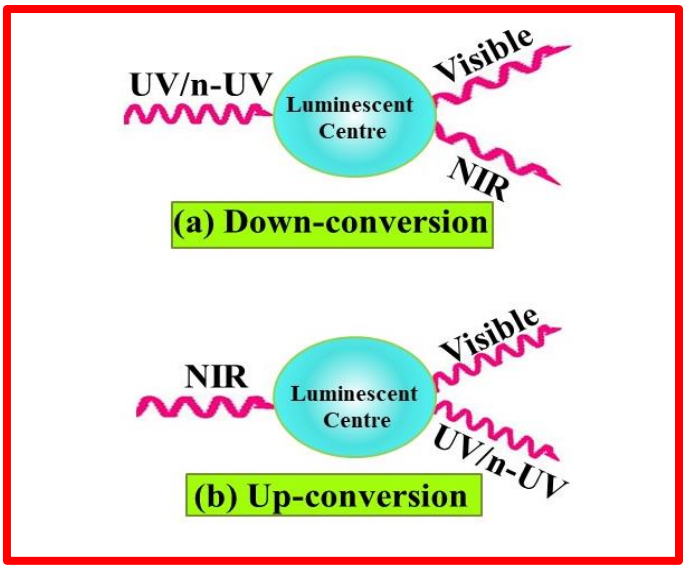

Figure 1.2. *(a) Down-conversion and (b) Up-conversion processes*

1.2. Phosphors and luminescence mechanism

Phosphors or luminescent materials exhibit the phenomenon of luminescence, when excited by an external energy source [1]. The word "phosphor" is derived from Greek language, stands for "light bearer". Generally, the phosphors are mostly inorganic solid materials composed of a host lattice and an activator. The activator ions, which act as luminescent centers are the impurities doped in small quantities intentionally in the host material. Sometimes the activator ions may not absorb the incident energy efficiently, then another kind of appropriate impurities can be incorporated in the host material, termed as sensitizers. The sensitizers absorb the energy from the incident radiation and subsequently transfers the absorbed energy to the activator ions. In some special cases, the host material itself has the capability of absorbing excitation energy and hence the host material behaves as the sensitizers. For example, self-luminescent YVO_4 (vanadate) phosphor in which VO_4 absorbs energy in the UV range via charge transfer from oxygen to vanadate and finally ET can take place to activator ions after its incorporation into the host [22, 23]. The fundamental processes that are involved in luminescence can be further categorized as discussed below:

1.2.1. Excitation process

The emission of photons from the phosphor takes place only when the system is excited to higher state which can be possible via either of the following ways:

- Indirect excitation followed by the transfer of energy from the host lattice or sensitizer to the activator.
- Direct excitation of the activator ions.

When absorption take place in the host lattice, it may release the absorbed energy and give emission in visible range. The emission taking place via host excitation is termed as host sensitized/self-luminescence and is usually observed in vanadates, molybdates and tungstates (Fig. 1.3(a)) [23]. The host may also release its absorbed energy non-radiatively, which can be

lost as heat in the lattice. Another possibility is that the host material can acts as a sensitizer and migrate the absorbed energy to the activator ion (Fig. 1.3(b)). The activator ion then gets excited to higher levels and subsequently de-excite to ground state by providing visible emission.

Moreover, the activator can be indirectly excited by the energy released from sensitizer (another ion doped in the host). In this, sensitizer after absorbing incident energy, transfers it to the activator and hence emission from activator is observed (Fig. 1.3(c)) [24]. In the case of direct excitation, the activators directly absorb the excitation energy and then undergoes radiative and non-radiative relaxation (Fig. 1.3(d)) [25].

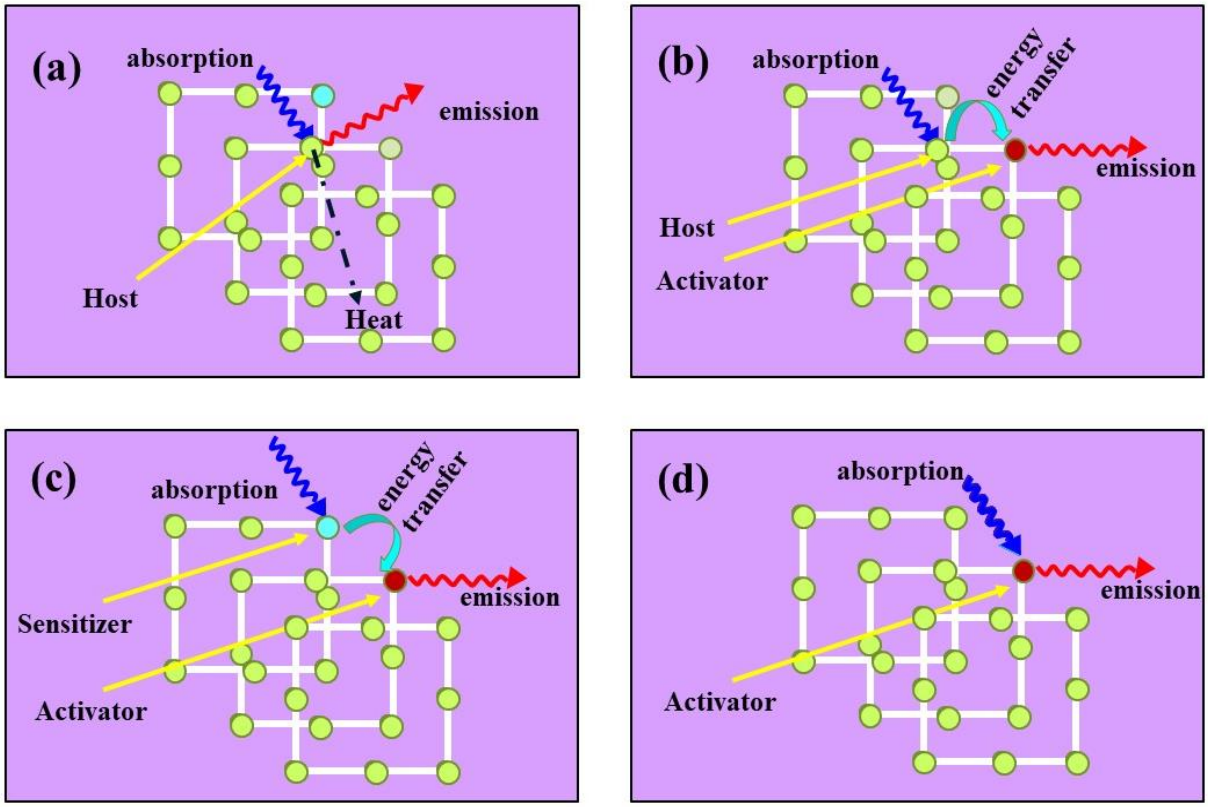

Figure 1.3. *Absorption of incident energy, energy transfer, and emission (a) Host sensitized luminescence, (b) Host + Activator type luminescence, (c) Host + Sensitizer + Activator type luminescence and (d) Direct excitation of activator ions*

1.2.2. Energy transfer mechanism

In general, there are four fundamental mechanisms constituting the ET processes from sensitizer to activators (i) Resonant radiative ET via emission of sensitizer and re-absorption of

emitted energy by the activator (Fig. 1.4(a)) (ii) Non-radiative ET associated with resonance amid sensitizer and activator ions (iii) Multi-photon facilitated ET and (iv) Cross relaxation among two indistinguishable adjoining luminescent centres. The radiative ET efficiency is influenced from the efficiency of activator's excitation through the sensitizer emission. The significant overlap between the sensitizer's emission and activator excitation may lead to efficient radiative ET. The indication for predominance of the radiative ET process is that the lifetime of the sensitizer's fluorescence does not alter with the increasing activator ion concentration. While in the case of the non-radiative ET (Fig. 1.4 (b)), as the activator ion concentration is increased, significant reduction can be observed in the decay time of sensitizer fluorescence. The non-resonant ET can be facilitated by the phonons, if the difference between the ground state of sensitizer and excited state of activator is large. Then the ET will be through phonon-assisted non-radiative transitions (Fig. 1.4 (c)). The ET process in phosphors majorly dependent on the characteristic transitions resulted from competitive interaction between sensitizer and activator due to precise difference between their energy levels. In some cases, ET may take place between two indistinguishable adjoining luminescent centers and they may attain an intermediate level by giving off the excess energy to another nearby centre, which after absorbing the energy rises to the same intermediate or some other level having the same energy difference. This process is known as cross-relaxation Fig. 1.4 (d)) [26, 27].

In the case of direct excitation, the activator directly absorb the excitation energy and de-excite in the form of radiative and non-radiative relaxations. In some cases, the activator energy migrates among large number of centers and then these centers exude their energy by relaxing to the ground state via multiphonon emission. These are the centres from where the probability of radiative transition is low. These quenching centres serve as an energy sink for the energy migration chain that leads to the quenching of luminescence.

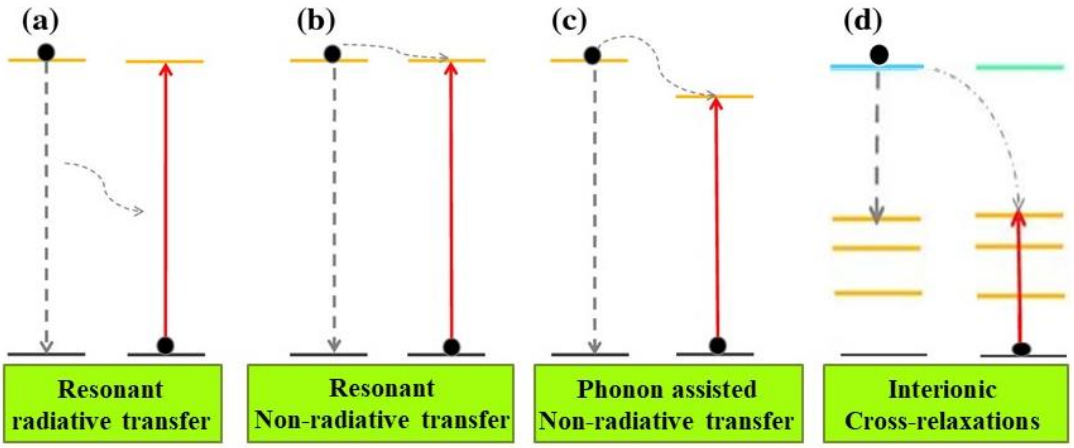

Figure 1.4. *Schematic diagram for different energy transfer processes between two ions*

The decline of emission intensity after a certain amount of dopant concentration (concentration quenching) can also be better understood in terms of energy transfer. Each phosphor exhibits maximum luminescence output at an optimum concentration of dopant ions. As all the activator ions possess identical excited states and with the increasing activator contents in the phosphor there are more probabilities for non-radiative energy transfer to take place between neighbouring activator ions as they are close enough [28].

1.2.3. Emission process

To understand the different processes involved in the emission of light, configurational coordinate model of characteristic luminescence is pretty much informative. The configurational coordinate model typically describes the luminescent mechanism including absorption and emission process along-with lattice vibrations (Fig. 1.5). This model also clarifies the influence of crystal relaxation after an electronic transition. Here, vertical axis represents the potential energy curves of an ion in the ground and higher excited electronic state while the horizontal axis gives the deviation from the bond distance. A potential curve traces a plot of binding (electronic) energy with associated vibrational levels of an ion versus its inter-nuclear distance from neighbouring ions [29]. The vibrational energy is quantized in a bound system and quantized vibrational states are designated as $\nu = 0, 1, 2$ in the ground state whereas $\nu' = 0', 1', 2'$ in the excited state. It is worthy to note that the shape of the potential curves may

vary and the positions of their minima with respect to the equilibrium inter-nuclear distance may not also coincide. The Franck-Condon principle governs absorption and emission processes involved in the luminescence, which states that an electronic transition in a molecule takes place much more rapidly than a vibrational motion of the nuclei that the instantaneous internuclear distance and the velocity of the nuclei can be considered remain unchanged during the electronic transition [30]. Therefore, the electronic transitions i.e. absorption and emission transitions can be represented as vertical lines. On the absorption of energy in the form of photons, the bound activator ion from its equilibrium ground state is excited vertically at a constant configuration coordinate to a higher energy state (non-equilibrium). Within the excited electronic state, the activator ends up in a high vibrational level as potential curves of two states are unsymmetrical. Some energy is lost as vibrational energy on relaxation of excited state to its lowest vibrational state. From here, the system returns back to its ground electronic state by releasing the energy difference as photons (luminescence). As shown in configurational coordinate model, the energy required to excite the system is more than the energy of emitted photons. Therefore, besides the nature of the excitation and emission process, configurational coordinate model also accounts for the origin of Stoke's shift [31].

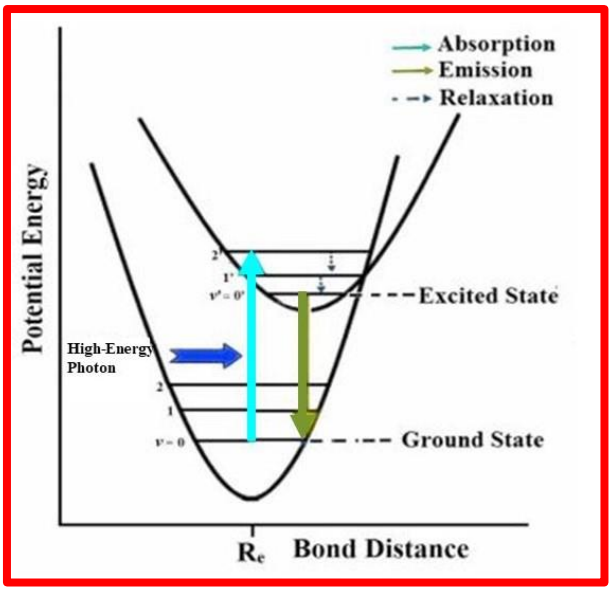

Figure 1.5. *Configurational coordinate model representing the excitation and emission proces*s

Besides luminescence, one more possibility of relaxation of excited state is non-radiative de-excitation. Non-radiative relaxation occurs when the luminescent centre can reach its ground state by a process different from photon emission. It is worthy to discuss the important processes that can compete with the direct radiative relaxation from an excited state. The most important non-radiative relaxation process that suppress the radiative de-excitation is multiphonon relaxation. Fig. 1.6 (a) illustrates the configurational coordinate diagram that can be employed to understand this de-excitation process. The crossover point of the ground and excited states is shown in the Fig. 1.6 (a). The line AB corresponds to excitation with its endings lying at the vibrational level (B) that is much below the shown crossover point. Then a rapid non-radiative relaxation that ends to C. The emission spectrum arises due to line CD. The multiphonon relax down the system from D to the initial point A. In case of Fig. 1.6 (b), where the crossover point lies at lower energy than point B, the activator can be de-excited to the vibrational state matching with the crossover point via multiphonon relaxation. The vibration level matching with crossover point also belongs to ground state parabolas. Hence, the de-excitation possibility from this vibrational level to ground state is most likely to be through the phonons. Therefore, the radiative emission does not occur at all. The system comes back to the ground state by means of a full non-radiative multiphonon relaxation through ground state parabola [32]. The concepts of configurational coordinate diagram can also be used to provide a rational explanation for the suppression of the luminescence at elevated temperatures. This process is commonly called as thermal quenching. At elevated temperatures, the vibrational levels lying higher than the point A in the ground state and point B in the excited state can be thermally populated. This grants the possibility of populated level at the crossover point. Thus, non-radiative relaxation cause de-excitation of a system to ground state which can also be called as thermally quenched luminescence [32]. The various processes involved in luminescence

properties discussed above are dependent on crystal field around the activator ions. The extent of crystal field depends on both host lattice and activator.

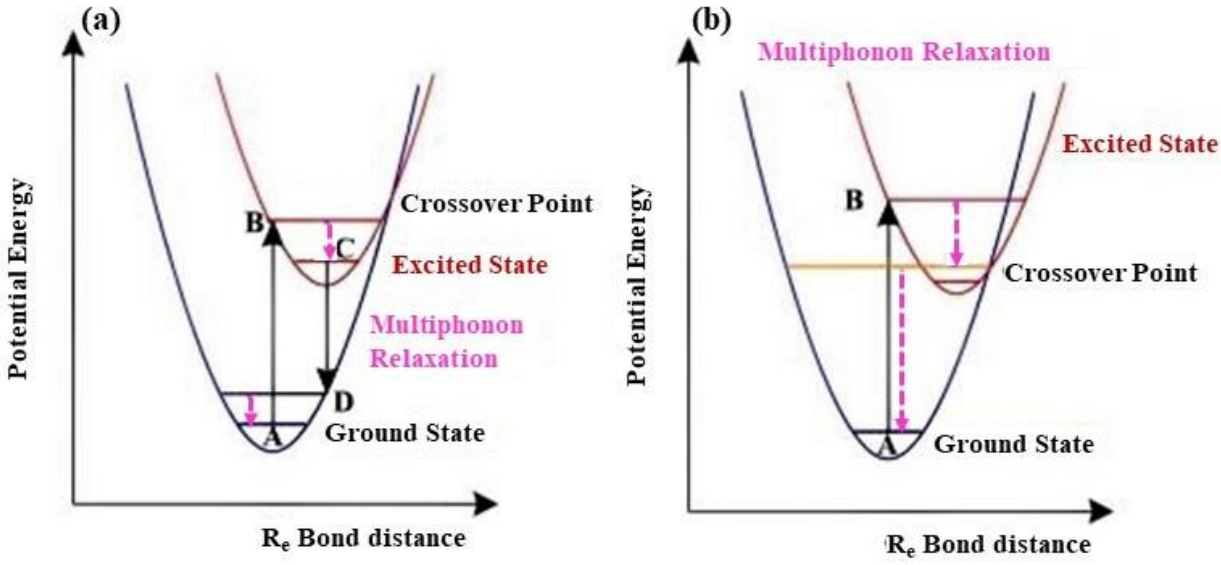

Figure 1.6. *Configurational coordinate model showing (a) partial multiphonon relaxation process and (b) full multiphonon relaxation process*

There are majorly two types of activator ions namely transition and rare earth (RE) metal ions. The present work is limited to the study of luminescence properties of phosphor activated by RE ions.

1.3. Fundamentals of RE ions

The RE elements are the members of lanthanide series starting from Lanthanum (La) to Lutetium (Lu) along with Scandium (Sc) and Yttrium (Y) [33]. However, these elements are plentiful in environment, but not available as dense minerals in economically exploitable ore deposits, hence named as rare earths. Scandium and Yttrium are also included in the list of RE due to their occurrence in the same ore and show similar properties as lanthanides. Although these elements are alike in terms of chemical behaviour, yet their physical properties are unique such as color and luminescence behaviour. Due to their fascinating properties, RE elements are utilized in the versatile fields of material science, applied chemistry and physics and basically in almost all the disciplines of science and technology.

The general electronic configuration of RE elements is $[Xe]4f^n$ (n=0-14). These configurations can give various electronic levels specified by term symbol called as spectral term ($^{2S+1}L_J$), in which three quantum number L, S, and J values ensued from spin-orbit coupling. These levels are very well defined, and their energy is fixed since 4f electrons remain unaffected by the external electronic field due to $5s^2$ and $5p^6$ electrons serve as protective shielding to 4f electrons and also these levels are independent of environment [34-36]. Some of the RE ions show $4f^{n-1}5d$ state, in which electron transfer may takes place from 4f to 5d orbital. The $4f^{n-1}$-5d transitions gets affected by the local environment around these RE ions [37, 38]. Therefore, most of the RE ions show +3 oxidation state in general and few RE ions exhibit +2 oxidation state. Moreover, these RE ions exhibit large stokes shift which is a prerequisite for designing a phosphor. In RE doped solids, photoluminescence is observed due to the presence of partially filled 4f subshell and either due to intra-configurational $4f^n$ transitions or inter-configurational $4f^n$-$4f^{n-1}5d^1$ transitions or charge transfer transitions [39, 40]. When RE ions are incorporated into the host, accommodate energy levels within the optical band gap of host.

1.3.1. Types of interactions in RE ions

Among RE ions, there are basically three types of optical transitions i.e., characteristic transitions in-between various 4f levels, $4f^{n-1}5d^1$ transitions and charge transfer transitions as discussed below in detail:

(a) Intra-configurational f-f transitions: The RE ions doped materials exhibits various narrow lines attributed to the electronic transitions between $^{2S+1}L_J$ to free ion level or J-manifolds in 4f subshell. They are spin forbidden. In f-f transition, excitation and emission energies remain independent of the host material doped with the activator ions as they are effectively shielded from 5s and 5p shells. Due to the shielding effect, these spectra exhibit

narrow line width. The interaction of the RE ions in the host with the light give rise to different types of transitions as mentioned below:

(i) Magnetic dipole (MD) transitions: When the magnetic field factor of the incident light have interaction with the RE ion through a magnetic dipole, a weakly intense transition is observed and termed as magnetic dipole (MD) transition. When the charges get displaced rotationally and direction of rotation remains same under inversion through a point, MD transition occurs. The MD transition has even transformation under inversion and it exhibits even parity which means it allows transition between states having same parity. Therefore, a MD transition is endorsed by the Laporte's selection rule ($|\Delta l| = \pm 1$, $|\Delta s| = 0$, $|\Delta L| \leq 0$, $|\Delta J| = 0$; $J = 0 \leftrightarrow 0$ transition is forbidden) [41, 42]

(ii) Forced electric dipole (ED) transitions: An ED transition takes place when the RE ion interacts with the electric field factor of the incident electromagnetic radiation via an electric dipole. The electric dipole results in linear movement of charges. The forced ED transition has odd transformation properties under inversion and has odd parity. This transition is forbidden in RE ion doped materials, since the start and end states of $4f^n$ transition have the same parity. Hence, these ED transitions are restricted by the Laporte's selection rule ($|\Delta l| = \pm 1$, $|\Delta s| = 0$, $|\Delta L| \leq 6$, $|\Delta J| \leq 6$). However, the non-centro symmetrical interactions of the electronic states allow the mixing of states of opposite parity that induces the ED transition and therefore known as induced ED transition. Certain induced ED transitions are sensitive to the environment around RE ions and therefore also known as hypersensitive transition that follow the selection rules ($|\Delta S| = 0$, $|\Delta L| \leq 6$, $|\Delta J| \leq 6$). These hypersensitive transitions are also termed as pseudo quadrupole transitions as they obey same selection rules as followed by quadrupole transitions [43]. These hypersensitive transitions originate from an asymmetrical distribution of dipoles induced by the electromagnetic radiation in the

surrounding of the RE ions. The intensity of these transitions gets effected by the local field symmetry and inhomogeneity in the dielectric medium around RE ions.

(iii) Electric quadrupole transitions: The electric quadrupole transition becomes apparent with the displacement of quadrupole charges. An electric quadrupole is composed of four-point charges or two dipoles arranged in such a way that their net dipole moments is zero. An electric quadrupole has even parity. Electric quadrupole transitions are frail in correlation with MD and induced ED transitions [44].

(b) Inter-configurational ($4f^n5d^0$-$4f^{n-1}5d^1$) transitions: The transfer of 4f electrons into 5d subshell is parity allowed. Since d orbitals get greatly influenced by the ligand field effect, the intensity of such transitions highly susceptible to the surrounding of RE ions and their intensity is high [45]. The transitions between $4f^{n-1}5d^1$ and $4f^n5d^0$ levels give rise to a broad range of excitation and emission wavelengths compared with the very narrow peaks from transitions between 4f-4f levels. The broad range of f-d transitions can be described on the basis of two phenomena: the Franck-Condon principle and breaking of the degeneracy of the 4f ground state. Furthermore, the 4f degeneracy breaks due to spin-orbit coupling into multiple levels. Moreover, activator ion in a host crystal may undergo centroid shift and/or crystal field splitting. The centroid shift is defined as shift in 5d energy levels to lower side due to decrease in the inter-electronic repulsion. The crystal field splitting, as the name suggests, is the splitting of 5d energy levels due to the environment provided by the host to the activator ion in which it is doped. The factor on which the magnitude of crystal field effect depends include bond length between activator ion and the ligand, the overlapping of molecular orbital or nature of bond (ionic or covalent), the surrounding environment, and the site symmetry of the activator ion. The crystal field splitting reciprocates to the change in bond length, or polyhedral volume in opposite manner [46].

(a)***Charge Transfer Transitions:*** The excitation and emission spectra can largely be influenced by the charge transfer transitions occurring in the host or dopant. This type of transitions are usually very intense and can easily outshine the *f-f* absorption of the activator. These type of absorptions can occur in the host such as vanadate or tungstate; but also in the activator itself for example, the charge transfer from $O^{2-} \rightarrow RE^{3+}$ [47].

1.3.2. Unique properties of RE ions

On the basis of distinctive interaction discussed above, RE ions exhibit unique properties that discriminate between REs and other optically active ions are as follows:

- RE ions exhibit luminescence in various spectral regions such as in visible and NIR regions of the electromagnetic spectrum.
- RE ions exhibit narrow spectral lines and have long emission lifetimes.
- They exhibit large stoke shift upon ligand excitation (gap between excitation and emission wavelength is large).
- Their 4f-4f transitions (intra-configurational) in RE ions have small homogeneous linewidths.
- They possess several energy levels suitable for optical pumping.
- Well-developed theoretical models are available for systematic study of the energy levels, transition intensities and excited state dynamics.

The above-mentioned enthralling properties of these divalent and trivalent RE ions facilitate their utility in various applications especially in bio-sensing, bio-medical treatments, display devices, solar cells, fingerprint sensing, indoor plant cultivation and solid-state lighting [45, 48-50].

1.4. Solid state lighting

Artificial lighting has achieved multipurpose opportunities in indoor and outdoor systems for expanding the prolific day into non-sunlit hours of night and thus contributed immensely to enlarge the productivity of human life. Globally, artificial lighting production includes immense amount of energy. Earlier, the conventional lighting sources such as fire lamps (first generation), incandescent bulbs (second generation) and fluorescent lamps (third generation) were used for artificial lighting which rely either on heat or discharge of gases. These lighting devices involve high temperature that leads to large energy losses. Moreover, these devices release toxic substances and more CO_2 into the environment [51]. In recent years, the escalating demand for the annual energy consumption and other environmental issues force the population to shift towards the energy saving and environmental friendly alternatives of conventional lighting sources [52]. In this regard, solid state lighting (SSL) sources are currently serving as a fourth generation lighting device since it has remarkably reduced annual energy consumption. SSL is the light emitted by a solid, which can be a piece of semiconductor or an insulator. In this new lighting technology, the visible light comes from the solid state light-emitting diodes (LEDs), which efficiently and directly convert electricity to light. The introduction of the LEDs has hampered the usage of incandescent and fluorescent lamps as it outshines on the benchmark of energy efficiency, affordability, proficiency, cost effectiveness and color-balanced white light [53, 54]. Predominantly, there are two approaches which have been availed to fabricate w-LEDs. The first one includes using phosphor free RGB-LEDs in which monochromatic light from red, green and blue LEDs are mixed directly to get white light emission [52, 54, 55]. These integrated LEDs need to have different driving currents for the individual LED to produce constant white light emission which is difficult to obtain and made it less accessible. Also, different driving currents lead to degradation of different color LEDs and results in instability of color temperature [56].

Another approach includes the accomplishment of white light emission via combination of blue light emitting InGaN chip and yellow phosphor (YAG: Ce^{3+}), which is presently used in most of the commercial w-LEDs [57, 58]. Despite of its several advantages over RGB-LEDs like low cost, simplicity in fabrication and high brightness, such w-LEDs have some drawbacks like low color rendering index (CRI < 70), high correlated color temperature (CCT >7765 K), halo effect and low efficiency due to lack of the red component [59, 60]. Therefore, researchers over the globe proposed alternative approaches to deal with this obnoxious problem such as "blue LED coated with green and red phosphors" and "n-UV LED coated with an appropriate mixture of RGB phosphor". Apparently, both the above mentioned approaches obligate the synthesis of a promising red emitting phosphor. However, a multi-phase phosphor approach leads to depreciated efficiency because of the re-absorption of blue emission by RG phosphors [61]. All such shortcomings can be resolved by adopting another sophisticated approach of coating co-activated single-phase phosphor that can provide warm white light emission. All the above mentioned approaches for white light generation have been displayed in Fig. 1.7. Also, the pros and cons of different methods have been listed in Table 1.1. As-prepared co-activated single-phase phosphor can offer excellent color reproducibility, sufficient CCT, spectral tunability and soothing perception to eyes.

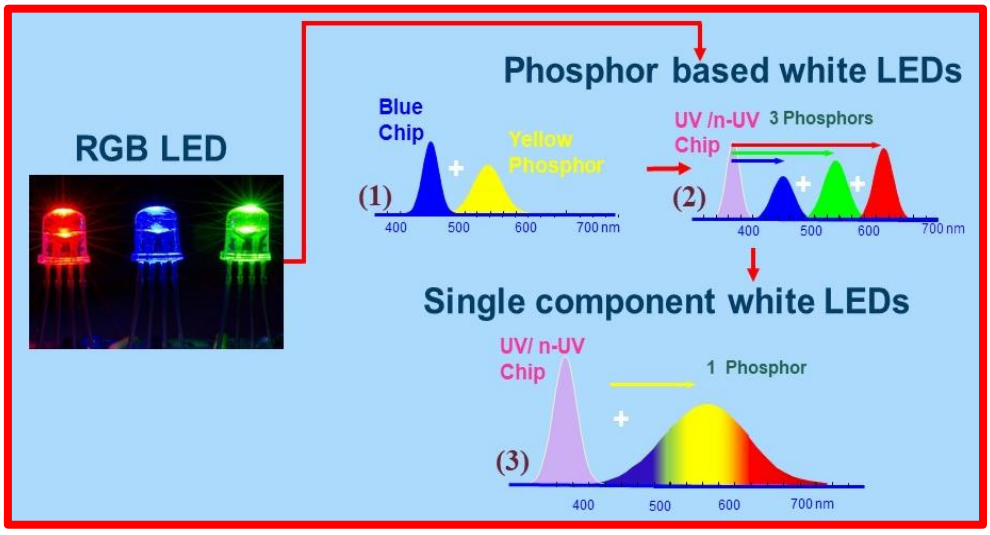

Figure 1.7. *Different approaches for white light generation*

Table 1.1. *The pros and cons of different methods to generate white light*

	RGB LEDs	**Blue LED + Yellow Phosphor**	**UV/n-UV LED + Multiphase RGB Phosphor**
Pros	• Light source with variable color point • High efficiency	• Low cost • Easy fabrication	• High efficiency • High CRI • High chromatic stability
Cons	• Need variable driving current to operate red, green and blue LEDs • Instability of color temperature	• Low efficiency • Low CRI • Low chromatic stability • Lack of red component • Halo effect	• Complex blending of different phosphors

Moreover, In recent times, phosphor converted light emitting diodes (pc-LEDs) are being perceived as smart lighting sources with the capability of controlling spectral composition via phosphor coated over the LED chip in indoor cultivation systems [61-64]. For plant growth under such controlled systems, lighting devices emitting specifically in blue (B), red (R), and far-red (FR) spectral region is an indispensable requirement. Such an advanced lighting system may drive photosynthesis and also beneficial for germination, flowering, fruitages and other crucial morphogenesis of plants [65-67]. Apart from chlorophyll (a photosynthetic pigment), two photo-interconvertible phytochromes/photoreceptors (P_R and P_{FR}) exhibiting different absorption spectra are also present in plants. The P_R absorbs red light in the daytime to convert into P_{FR}, whereas in the night, P_{FR} absorbs FR light to convert into P_R. The P_R and P_{FR} play crucial roles in plant growth and flowering. For instance, the red light absorption by P_R could alter flowering process ahead of scheduled time in long-day plants. In contrast, sensitization of P_{FR} via FR illumination could alter gene expression of plant structure and stimulate the growth. The different red to FR light ratios usually led to various physiological variations in plants from vegetative to floral development. Therefore, artificial

lighting with an adjustable R to FR light ratio is paramount for controlling the flowering and physiological changes in plants [67-69].

The emission from pc-LED matching well with plant photoreceptors (P_R and P_{FR}) can offer ideal production in plant growth systems. Besides this, pc-LED delivers numerous advantages over prevailing lighting sources (incandescent, metal halide and high-pressure lamps) such as environmental protection, improved energy efficiency, smaller size, advanced control capabilities, longer service time and reduced radiated heat [70, 71]. In general, pc-LEDs fabricated by coupling with FR emitting Mn^{4+}-doped phosphors and other red phosphors may exhibit an emission overlapped with the absorption spectrum of phytochromes. Such fabricated pc-LEDs can aid to control the duration of sunlight sensed by plants, which can regulate the flowering time of plants [72, 73]. Therefore, it is of a great significance to develop eco-friendly phosphors emitting red light under n-UV/blue light excitation for promoting regulated plant growth.

1.4.1. Color rendering index (CRI)

The CRI is a unit-less index measured as the difference in perceiving the color of object under source of illumination and a reference source such as natural light source/sunlight. CRI can be indexed as integral value from 0 to 100. The low CRI ratings suggested that less accurate color will be reproduced. The CRI value of 100 would signify that the perceived color of all the samples illuminated by a light sources and incandescent light source have high CRI since all colors in their spectrum are rendered equally [2, 46].

1.4.2. CIE color chromaticity coordinates & color purity

The Commission International de L'Eclairage (CIE) 1931 uses the color matching functions $\bar{x}(\lambda)$, $\bar{y}(\lambda)$ and $\bar{z}(\lambda)$ to characterize or express the color of any object (self-luminous or reflecting). The chromaticity coordinates (x, y) can be determined from the emission spectral

data and the color matching functions. The evaluated chromaticity coordinates plotted on a chromaticity (CIE 1931) diagram specifies the color of illuminant (object). The formula to evaluate chromaticity coordinates (x, y) is given below [74]:

$$x = \frac{X}{X+Y+Z} \tag{1.1}$$

$$y = \frac{Y}{X+Y+Z} \tag{1.2}$$

where, X, Y and Z are tristimulus values provides degree of stimulation for each of the primary (red, green and blue) color required to match the color of power spectral density (P(λ)) according to the following equations [74]:

$$X = \int \bar{x}(\lambda)P(\lambda)d\lambda s \tag{1.3}$$

$$Y = \int \bar{y}(\lambda)P(\lambda)d\lambda \tag{1.4}$$

$$Z = \int \bar{z}(\lambda)P(\lambda)d\lambda \tag{1.5}$$

The value of CIE coordinates along the perimeter of the CIE diagram signifies the monochromaticity. Therefore, to ascertain monochromaticity of the material under consideration using as obtained CIE coordinates, the color purity can be evaluated using the expression as follows [73]:

$$\text{color purity} = \frac{\sqrt{(x-x_{ee})^2+(y-y_{ee})^2}}{\sqrt{(x_d-x_{ee})^2+(y_d-y_{ee})^2}} \tag{1.6}$$

where, (x, y) represents the color coordinates of the phosphor, (x_{ee}, y_{ee}) are the coordinates of standard white point in the CIE diagram and (x_d, y_d) are the coordinates of dominate wavelength point. The color purity of the monochromatic emitters should be 100%. The standard CIE 1931 diagram is represented in Fig. 1.8.

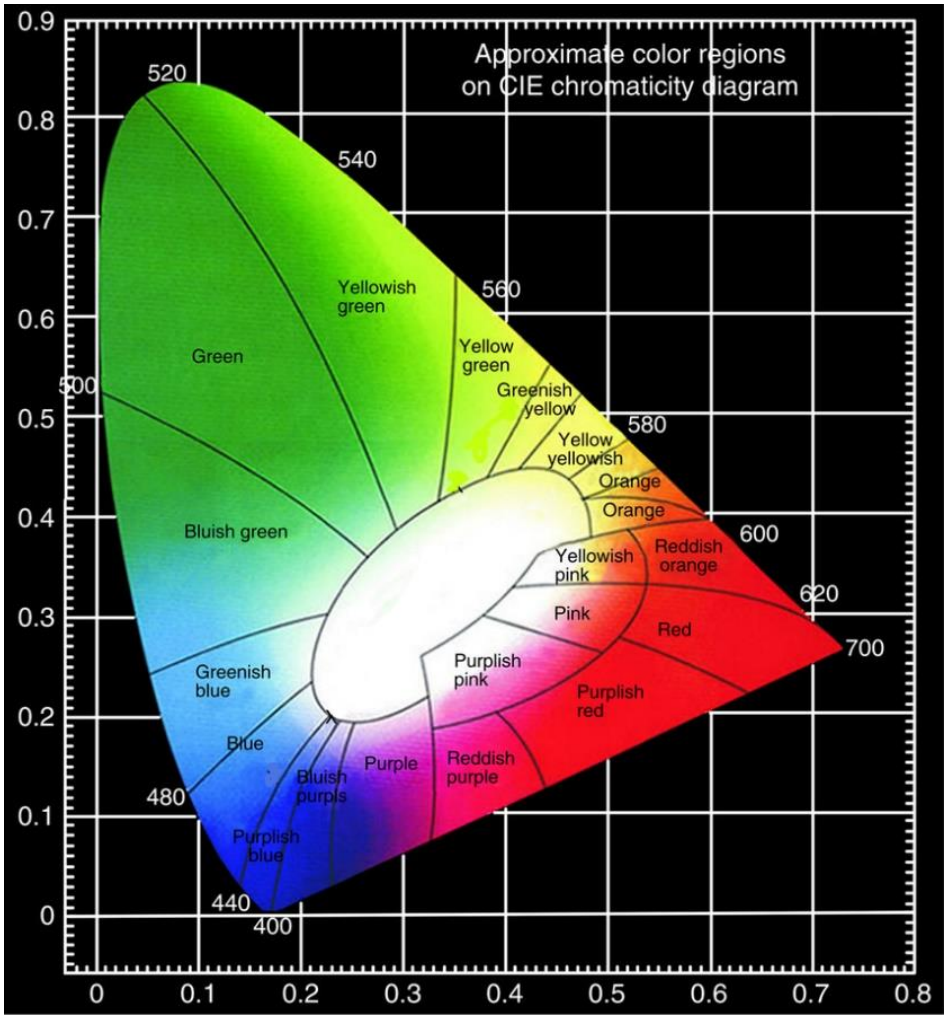

Figure 1.8. *The standard CIE 1931 diagram*

1.4.3. Correlated color temperature (CCT)

It is defined as the absolute temperature of a blackbody, whose chromaticity resembles the same color as that of the light source [51]. As the temperature increases, hot objects will subsequently glow in red, orange, and yellowish white and bluish white. CCT is a method that manifest the color characteristics of light, such as low CCT indicate warm light with more of yellow and red perception while high CCT appears to be a more blue light indicates cold white light, by measuring it in degrees Kelvin (K) [46]. Typical CCT of the white region diagram is in the range between 2000 and 10000 K. The CCT can be calculated using the equation given by McCamy [73]:

$$CCT = -449n^3 + 3525n^2 - 6823.3n + 5520.33 \quad (1.7)$$

where, $n = \frac{x-x_e}{y-y_e}$ represents inverse slope line; (x, y) are the CIE coordinates obtained for the sample under consideration and (x_e = 0.3320, y_e = 0.1858) are the coordinates for epicentre. It has been speculated that the CCT value>5000 K indicate cool white light emission, whereas the CCT value<5000 K indicate warm white light emission.

1.4.4. Excited state dynamics of RE ions

The PL decay is a non-linear optical process described by non-linear polarization of the incident light beam. Nonlinear emission responses of luminescent materials manifest excited state dynamics such as radiative and non-radiative relaxation, inter-system crossing of a molecule from singlet to triplet state, conformational properties such as trans-cis isomerisms and ET mechanism of samples under investigation. The intensity in PL decay spectroscopy is monitored at different time delays after excitation, allowing for high temporal resolution. Temporal resolution should be fast in comparison with the excited-state lifetime of the RE ions on the appropriate time scale. The fluorescence decay time evaluated from decay profiles provides valuable information about the excited state decay dynamics of RE ions, ET, molecular interaction with the surroundings, and optical gain of the samples for advancement in optoelectronics, photosynthetic systems, nano-electronics and biological applications [11]. The decay profiles of the as-synthesized phosphor may show appropriate fitting with either single or bi-exponential equations. Single exponential fit can be obtained at very low concentrations of activator ions in the host lattice, indicating very less probability of ET among them. Bi-exponential fit indicate the probability of ET between them. The single and bi-exponential equation can be given as [73]:

$$I = I_0 + A \exp\left(-\frac{t}{\tau}\right) \tag{1.8}$$

$$I = I_0 + A_1 \exp\left(-\frac{t}{\tau_1}\right) + A_2 \exp\left(-\frac{t}{\tau_2}\right) \tag{1.9}$$

For single exponential equation fit, τ represents the decay time for the emitting level of an activator, whereas in case of bi-exponential fit τ_1 and τ_2 represent the fast and slow components of lifetime. By using τ_1 and τ_2, the average decay time (τ_a) of the emitting level can be evaluated using formula given below [73]:

$$\tau_a = \left[\frac{A_1\tau_1^2+A_2\tau_2^2}{A_1\tau_1+A_2\tau_2}\right] \quad (1.10)$$

Fluorescence lifetime depend on the rate of radiative and non-radiative relaxations. The lifetime value decreases with increase in non-radiative relaxation rates due to increased surface defects or quenching centres.

1.4.5. Thermal stability

Among major essential requisites for phosphors to be applicable in LED applications, sustaining the emission intensity even at higher temperatures is also an essential requirement such as 423 K (operating temperature of the LED). The temperature dependent emission spectra provide temperature dependence of the relative intensity of phosphors at dominant excitation with respect to the intensity at 303 K. Generally, a decreasing trend with a rise in temperature is observed owing to thermal quenching phenomenon. The thermal quenching phenomenon takes place as a result of non-radiative relaxations in phosphors. The temperature dependence on the non-radiative emission rate (R_{nr}) can be expressed as:

$$R_{nr} = K \exp\left(-\frac{\Delta E_a}{k_B T}\right) \quad (1.11)$$

where, k_B is well known Boltzmann's factor having value 8.61733×10^{-5} eV/K; K is a constant; ΔE_a represents the activation energy related to thermal quenching. The activation energy (ΔE_a) is the energy separation between the lowest point in the excited state parabola and the crossover point for the excited and ground states. It is clear from the equation (1.11), that increase in temperature will increase the non-radiative relaxations rate, which leads to a decrease in emission. The alterations in relative emission intensity with rising temperature can

be employed to evaluate the activation energy (ΔE_a) of the phosphor as mentioned in the Arrhenius equation given below [75]:

$$I_T = \frac{I_O}{1+\alpha \exp\left(-\frac{\Delta E_a}{k_B T}\right)} \quad (1.12)$$

where, I_O and I_T correspond to the luminescent intensity at initial and testing temperature, respectively, while α is a constant factor. The graph between $\ln[(I_O/I_T)-1]$ and $1/(k_BT)$ for the most intense emission peak of phosphor is a linear graph with some slope, which provides the value of ΔE_a. The obtained value of ΔE_a in eV demonstrate the thermal stability of the phosphor. More the value of activation value, better is the thermal stability of the phosphor.

1.5. Theoretical models to understand ET process

In general, each phosphor exhibits maximum luminescence output at an optimum concentration of dopant ions. This optimum concentration depends upon a number of factors from phase prototype of the host to nature of the activator. The decline of emission intensity after a certain amount of dopant concentration is known as *concentration quenching*. As all the activator ions possess identical excited states and with the increasing activator contents in the phosphor there are more probabilities for ET to take place between neighbouring activator ions as they are close enough. ET between two neighbouring ions take place only if resonance occurs in their ground and excited states energy difference and if suitable interaction exists between the two. Generally, the energy can be transferred among the neighbouring activator ions by three major processes namely (i) exchange interaction, (ii) reabsorption and (iii) multipolar interactions [26]. For radiation reabsorption, the excitation and emission band must overlap, which can be ruled out in most of the cases. Furthermore, to recognize the actual mechanisms (exchange interaction or multipolar interactions), the critical distance of ET (R_c) must be estimated which is given by Blasse [73]:

$$R_c = 2\left[\frac{3V}{4\pi X_c N}\right]^{\frac{1}{3}} \quad (1.13)$$

where, X_c symbolize the optimum concentration of activator ions at which the luminescence intensity is maximum, V and N signify the volume and number of host cations corresponding to crystallographic unit cell, respectively. The condition for exchange interaction is that the value of R_c should be less than 5Å [75]. If not, the last possibility (due to high value of R_c) for ET is via multipolar interactions, which can be determined using Dexter's theory.

(a) Dexter theory: The multipolar interactions can be of three types namely dipole-dipole (d-d), dipole-quadrupole (d-q), and quadrupole-quadrupole (q-q) interactions, which can be determined using Dexter's ET equation [75]:

$$\log\left(\frac{I}{x}\right) = -\frac{Q}{3}logx + A \quad (1.14)$$

where, I is the luminescent intensity and x represents the activator ion concentration. Q determines the type of multipolar interactions, i.e. Q = 6, 8 and 10 corresponds to d-d, d-q and q-q interactions, respectively [75].

Further, to identify the type of multipolar interaction between sensitizer and activator system, Dexter and Reisfeld's approximation can be employed on emission spectra or Inokuti-Hirayama (I-H) model on PL decay curves.

(b) Dexter and Reisfeld's approximation: To recognize the multipole-multipole interaction type in between activator and sensitizer, Dexter and Reisfeld's approximation can be used. It delivers the general dependence of quantum efficiency viz. η_{s0} and η_s of sensitizer without and with activator ion, respectively on the total (sensitizer and activator) ion concentrations (C) [74]:

$$\frac{\eta_{s0}}{\eta_s} \propto C^{n/3} \quad (1.15)$$

where the ‘n’ signifying the multipolar interaction type, may take values as 6 (d-d), 8 (d-q) and 10 (q-q). The ratio of quantum efficiencies ($\frac{\eta_{s0}}{\eta_s}$) of sensitizer ions without and with activator can be estimated using emission intensities ratio ($\frac{I_{s0}}{I_s}$). Here, I_{s0} and I_s are the intensities of the most intense emission peak due to sensitizer without and with activator, respectively. Therefore, the above equation can be expressed as [76]:

$$\frac{I_{s0}}{I_s} \propto C^{n/3} \tag{1.16}$$

The graphs of $\frac{I_{s0}}{I_s}$ versus $C^{n/3}$ corresponding to the value of *n* to be 6, 8, and 10 are plotted. The best linear fit provides the value of n which indicate the type of interaction involved in ET. The associated ET efficiency (η_{ET}) from sensitizer to activator can be evaluated by using the below mentioned relation [76]:

$$\eta_{ET} = 1 - \frac{I_s}{I_{s0}} \tag{1.17}$$

(c) Inokuti-Hirayama (I-H) model: The ET mechanism between adjoining luminescent ions can be well understood using I-H model [57,58]. As per the I–H model, ET via multipolar interaction between neighbouring ions is leading to non-exponential nature of decay curves and decay intensity and time can be related as [78]:

$$I_t = I_0 * \exp\left[-\frac{t}{t_0} - Q * \left(\frac{t}{t_0}\right)^{\frac{3}{s}}\right] \tag{1.18}$$

where, and I_t and I_0 are the luminescence intensity at time ‘t sec’ and ‘0 sec’ after excitation, respectively. The values of s = 6, 8 and 10 represents d-d, d-q and q-q type of multipolar interaction and Q is the ET parameter [78].

1.6. Importance of the present host material

Phosphors are the essential components, which are mainly used in lighting, imaging and display applications. In the process of developing an efficient single-phase phosphor based LED, the adoption of host material has a remarkable influence on the luminescent properties exhibited by the phosphor. Therefore, the selection of an appropriate host material is imperative. Inorganic oxides have recently been demonstrated to be promising host materials due to special merits such as cost-effectiveness, facile preparation, environment friendly, excellent stable behavior, high chemical, thermal, and photo-stability. The above-mentioned admirable features of many inorganic oxides like vanadates, tungstates, niobates, phosphates, aluminates and silicates, etc. have held the interest of many experimentalists for further research [79-82]. Thereinto, the vanadates have been significantly researched for numerous applications such as display devices, optical-thermometry, solar cells, solid-state laser devices, pc-LEDs for indoor-cultivation and general illumination owing to their pre-requisite fluorescent properties.

The vanadates are the compounds containing oxyanions of vanadium in the form of simple groups, chains or network anions. There is an extensive family of anionic vanadate complexes depending upon the oxidation number of the vanadium in their structures. Among them, the vanadium anions with highest (+5) oxidation state (V^{5+}) forms different vanadate complexes viz. metavanadates, pyrovanadates and orthovanadates.

The orthovanadates are the simplest type of vanadates including a regular tetrahedra, VO_4^{3-} anion which has one double bond. The central vanadium cation is coordinated by four equivalent oxygen atoms in a resonance form giving tetrahedral symmetry. This coordination of ions in solid orthovanadates results in strongly bonded structures. Orthovanadate phase of a solid has empirical formula $[(VO_4)_n]^{3-}$ in which n = 1, 2, etc. with vanadium ion in +5

oxidation state. There is a structural variety of stable orthovanadates, which are formed by incorporating cations of alkali metals, alkaline earths or some transition metals (Y, La etc.) [22, 23]. The alkaline earth orthovanadates are prepared by the fusion of a mixture of vanadium pentoxide with the stoichiometric quantity of alkaline carbonates at extremely high temperature. The alkaline earth and yttrium based orthovanadate complexes doped with rare earth and transition metal ions are useful in electronic displays and laser applications [82]. Mixed cation vanadates particularly alkaline orthovanadates have been found to be economical and effective means of producing optically and physio-mechanically stable phosphors. This class of orthovanadates provides improvement over orthophosphates in regard to their structural and optical properties [79]. Most of the vanadate phosphors exhibit luminescence without the introduction of activator due to the electronic transitions in the tetrahedral anion VO_4^{3-}. The VO_4^{3-} complex in this type of activated host acts as a sensitizing unit and provides for the effective ET along the $VO_4^{3-}\rightarrow$ activator channel [82]. Vanadate hosts have strong charge transfer (CT) absorption bands from near UV to blue spectral region and their ability to entertain the trivalent rare-earth ions with their abundant energy levels to give a variety of emission wavelengths in the visible range make them potential material for preparing phosphors [82]. Therefore, we found it interesting to investigate the structural and photoluminescence properties of alkaline earth orthovanadates to explore their applications in general illumination and indoor agricultural lighting systems.

In the view of the above mentioned literature survey, an extensive investigation on a new ternary vanadate ($CaBiVO_5$) phosphor doped with RE ions has been done for general and agricultural lighting applications, which has not been explored to the best of our knowledge. By incorporating suitable RE ions, the present host can be tuned for different emission colors in the visible region for SSL applications, which has been motivating to carry out the present research work.

1.7. Objectives of the present thesis

During the past few years, the phosphor based LEDs have significantly contributed in the functionalities and success of artificial lighting systems, which are controlled, compact and sophisticated. In the present work, attempts are made to synthesize rare earth activated $CaBiVO_5$ phosphors with improved luminescent properties and finally to examine the approaches/methods to generate white light and also multicolor emission from $CaBiVO_5$ phosphor upon n-UV and blue LED excitations for agricultural lighting. Moreover, the main focus would be given for the enhancement of luminescence in rare-earth doped $CaBiVO_5$ phosphor through different synthesis procedures and after that optimizing the activator and sensitizer doping concentration. The extensive thermal, structural, morphological and photoluminescence characterizations are investigated to discuss significant research outcomes to accomplish the research objectives of the thesis. The main objectives of the present thesis work are:

- ❖ To synthesize single phase host lattice.
- ❖ To study structural, morphological, thermal and luminescence properties of the synthesized RE ions doped phosphors.
- ❖ To enhance the emission intensity by various techniques such as:
  - ➢ employing different chemical synthesis routes
  - ➢ co-doping various activators/sensitizers ions.
- ❖ To optimize the luminescence intensity in specific spectral regions required for the general lighting and photosynthesis applications.
- ❖ Finally, to develop environmental friendly phosphors desired for phosphor based solid state and agricultural lighting applications.

Chapter 2
Sythesis and characterization techniques

The development of high quality phosphors necessitates the profound understanding of their synthesis and allied characterization techniques. The quality of phosphors is said to be excellent, if the luminescent properties of the phosphor are reproducible. This chapter includes the explanation of synthesis methods employed to prepare RE doped $CaBiVO_5$ phosphors in the present work. As-synthesized phosphors were characterized for thermal, structural, morphological, optical and photo-luminescent properties. All the above mentioned properties were characterized with the assistance of various analytic tools such as X-ray diffraction (XRD), scanning electron microscopy (SEM), thermogravimetric-differential thermal analysis (TG-DTA), UV-Vis spectrometer and spectrofluorophotometer etc. This chapter explains the basic principles as well as instrumentation of equipments used for characterization in detail.

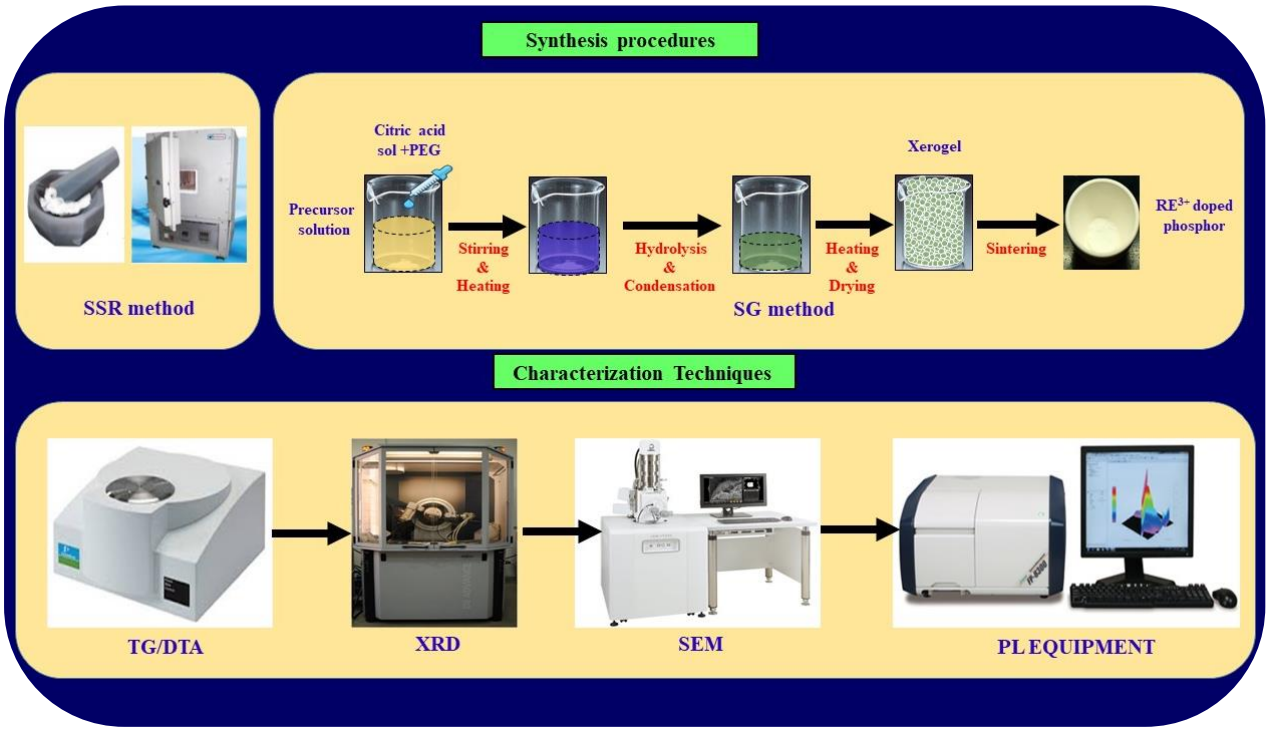

2.1. Experimental

The foremost step for the experimental research is then preparation and relevant characterizations of the material. This chapter embraces the description of various dry and wet chemical methods used to synthesize the luminescent materials (phosphors) and the appropriate characterization techniques used to understand their utilization in pc-LEDs for general illumination and agricultural lighting applications.

2.2. Synthesis methods

To prepare phosphors, many factors need to be considered meticulously such as choice of host, activator, purity of chemicals used, sintering temperature, duration of sintering, stirring of chemical solutions, choice of complexing agents, surfactants and many more [83]. There are various physical and chemical techniques to synthesize phosphors as reported in the literature, where physical synthesis methods include ball milling and chemical synthesis techniques consists of traditional solid-state reaction (SSR), citrate sol-gel (SG), combustion (CB), molten salt (MS), co-precipitation (CPT), spray pyrolysis (SPR) and hydrothermal (HT) [84]. The synthesis route is a pre-requisite constraint to govern the structure, morphology, distribution of particles and particle size. Moreover, the luminescence properties, and quantum efficiency can be enhanced by changing the method of synthesizing the phosphor. The SSR method has been prevailed in preparing most of the bulk powder phosphors as it is prototypical for solvent-free synthesis of solid products with higher yield [85]. But it demands the expanse of time as well as energy for sintering at a higher temperature and laborious grinding of the sample. Moreover, this synthesis technique suffers some serious implications such as creating defects that leave an unpropitious impact on the luminescent properties of the synthesized phosphor. When the reacting species diffuse rapidly, the reaction does not complete 100% that leads to some residue which results in some defects. To vaporize the residue and get the pure phase, grinding of raw

materials is followed by sintering. Moreover, fluxes can be added to a host material for ameliorating structure and morphology of the host matrix by providing a surface for faster diffusion of reacting species [86]. Also, the size distribution of the synthesized particles is random and lies in the micrometre range. Synthesis of phosphors employing alternating chemical route and its optimization can cause reduction in size and shape uniformity leading to appreciable enhancement in luminescent properties due to uniform mixing of the precursors in the liquid phase [87]. For instance, the purity and morphology of the sample in sol-gel method can be pre-eminently improved by controlling the pH value, inclusion of complexing agents and surfactants, which further improves the photoluminescence (PL) properties of the as-synthesized phosphors. The improved structure and morphology induces enhancement in the luminescence characteristics of the as-prepared phosphors [88, 89]. Among different wet chemical synthesis methods, combustion, and citrate sol-gel method were employed in synthesizing the phosphor to optimize the phase and luminescence behaviour of the phosphor.

2.2.1. Solid-state reaction (SSR) method

The SSR method is a dry media reaction which is used to prepare phosphors for industrial purpose where high yield and low cost are the essentials within short span of time [85]. In this method, the high purity raw material weighed in stoichiometric ratio are dispersed in volatile solvent such as acetone or ethanol, grinded and kept at higher temperatures to react via diffusion process. The temperature required for the synthesis of the phosphor is just maintained sufficient to have appropriate diffusion to accomplish the reaction on time before melting of precursor materials. There is reciprocal relation between reaction time and temperature. Sometimes, the production of such phosphors require repetitive grinding and heating steps for achieving the desired phase. After allowing natural cooling of samples to room temperature, the obtained phosphor is grinded, that is followed by further characterizations. In the present work, CBV phosphors were prepared using conventional SSR method by taking

highly pure chemicals, $CaCO_3$ (Fisher scientific, 99.9%), NH_4VO_3 (Fisher scientific, 99.9%), Bi_2O_3 (Fisher scientific, 99.0%), and RE_2O_3 (CDH, 99.99%) have been taken into stoichiometric ratio. All the chemicals have been dispersed in acetone and ground thoroughly for an hour in an agate mortar. The mixture has been taken in an alumina crucible and calcined at 950 °C for 3 h in a programmable muffle furnace to obtain a pure phase of RE^{3+} doped $CaBi_{1-x}VO_5$ (CBV: RE^{3+}) phosphor. Then, naturally cooled samples to room temperature (RT) have been powdered finely for further characterizations. The details of SSR synthesis method employed in the present work is represented in Fig. 2.1(a).

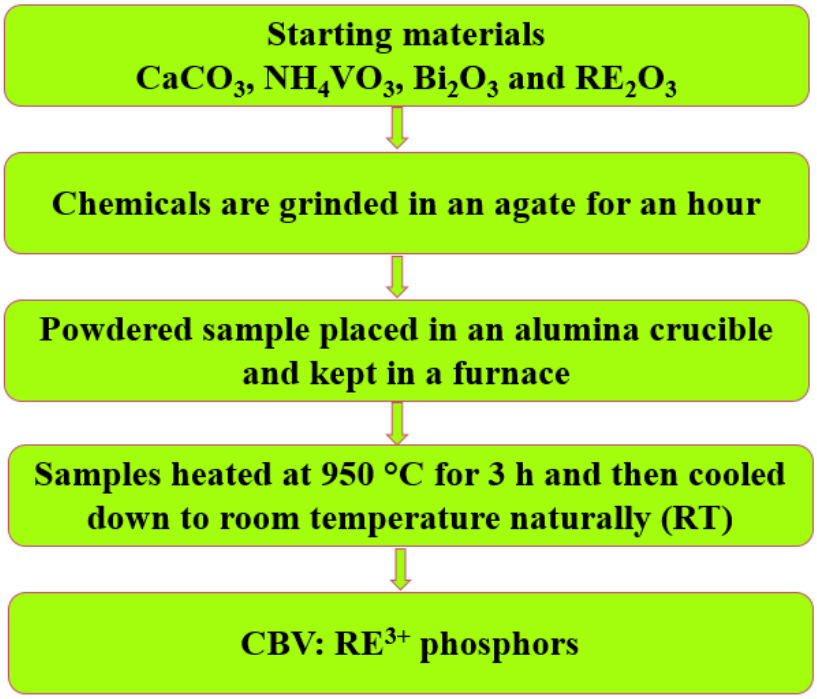

Figure 2.1. *Flow chart of SSR method used to synthesize CBV: RE^{3+} phosphor*

2.2.2. Combustion (CB) method

The CB method is a cost-effective and fast synthesis technique for the development of various industrially beneficial materials, which is the need of the hour. The CB technique is a low temperature synthesis and is a self-acting powerhouse to evolve heat which is more than that required for ignition of reactants. During CB method, the rapid decomposition of the

oxidizer (nitrate precursors) in the presence of an organic fuel (like urea, hydrazides, glycine etc.) takes place to yield the product in nano-form [90]. The important parameter to complete combustion is to maintain oxidizer to fuel ratio as 1, which can be obtained from the valences of oxidizers and fuel. In CB reaction, metal nitrates serve as oxidizing reactant and fuel as reducing reactant. The high energy released in exothermic reaction to increase the temperature of the reacting species and ignite to fire. CB reaction is self-propagating reaction that take place with evolution of gases to obtain the desired product. Some of the other advantages offered by CB are:

- Easy, fast and cost-effective
- Relatively simple equipments for sample preparation
- Highly pure product formation
- Possibility of stabilization of meta-stable phases
- Controllable size and shape of final products
- Uniform and desired dopant distribution throughout the host material

In the present work, to optimize the synthesis method for CBV phosphor, CB method was also explored. For this, the calcium nitrate tetrahydrate ($Ca(NO_3)_2.4H_2O$), bismuth nitrate pentahydrate ($Bi(NO_3)_3.5H_2O$), ammonium metavanadate (NH_4VO_3) and RE oxide (RE_2O_3) chemicals with high purity were used as starting materials. Glycine (AR grade) was used as a fuel for the synthesis of CBV: RE^{3+} by CB method. The appropriate amount of glycine was calculated by keeping the molar ratio of fuel to nitrates at unity in accordance with the concepts of propellant chemistry. The evaluated amount of glycine is dissolved in de-ionized (DI) water (referred as Sol. I). The stoichiometric quantity of NH_4VO_3 was dissolved in hot DI water (referred as Sol. A). The chemicals, $Bi(NO_3)_3.5H_2O$ and $Ca(NO_3)_2.4H_2O$ were dissolved in HNO_3 (referred as Sol. B) and mixed with Sol. A. Then, prepared nitrate solution of RE_2O_3 was added dropwise in it under continuous stirring at 80 °C for 1 h to get transparent yellow solution

(referred as Sol. C). The Sol. I was added dropwise into Sol. C and continuously stirred for 5 h at 120 °C for homogeneity and dehydration. After dehydration, the prepared resultant mixture was combusted on the hot plate maintained at 500 °C, yielding a voluminous foamy yellow powder by liberating a large amount of heat and gases. The yellow foamy solid was cooled to RT, and sintered at 850 °C for 3 h to acquire pure phase CBV: RE^{3+} phosphor.

2.2.3. Citrate sol-gel (SG) method

In SG method, the solution of a metal salt is prepared with appropriate solvents, which undergoes hydrolysis and polymerization under mild heat treatment in an acidic or alkali medium. Citric acid and PEG are added to form a polymeric network of metal citrate complex [91]. From that prepared sol, a gel is formed with an interconnected network having pores and polymeric chain. After gelation process, the wet gel is dried to get the fluffy powder. Single phase powdered oxide phosphors with better homogeneity and controlled morphology can be obtained after drying gel at an elevated temperature. Some of the advantages of SG method are:

- The control over particle size and morphology by changing solvents, pH of solution, heating conditions.
- The pure phase can be obtained without any extensive grinding and milling.
- The synthesis time is shorter than SSR method.
- The pure phase can be obtained at lower sintering temperature, hence lower agglomerations.
- Uniform distribution of desired dopant throughout the host lattice.

In the present work, CBV phosphors were prepared using SG method. In this method, the prepared yellow solution (Sol. C) as discussed in the preceding section is used as it is in this method. In SG method, citric acid employed as chelating agent and polyethylene glycol (PEG) as polymeric network former for metal citrate complex. The metal nitrates to citric acid molar

ratio was taken as 1:2 and thus calculated amount of citric acid dissolved in DI water and named as Sol. II. The Sol. II and 2 ml of PEG were added dropwise in Sol. C under continuous stirring at 120 °C for 5 h with pH value maintained at 1. On stirring, the resultant solution turns from yellow to blue and finally green gel under constant heating at 120 °C with the evaporation of solvents and thus forming gel. Apparently, color change might be due to several reactions between citrate and metal nitrates or between the decomposed products resulting from both citrate and nitrates. Subsequently, the gel is fired at 400 °C to yield dark green flakes by releasing large amount of gas and heat. Thus, prepared brown foamy solid was cooled down to RT, grinded and sintered at 800 °C for 3 h to get single-phase CBV: RE^{3+} phosphors. The details of combustion (CB) and citrate sol-gel (SG) synthesis methods employed in this thesis are represented in Fig. 2.2.

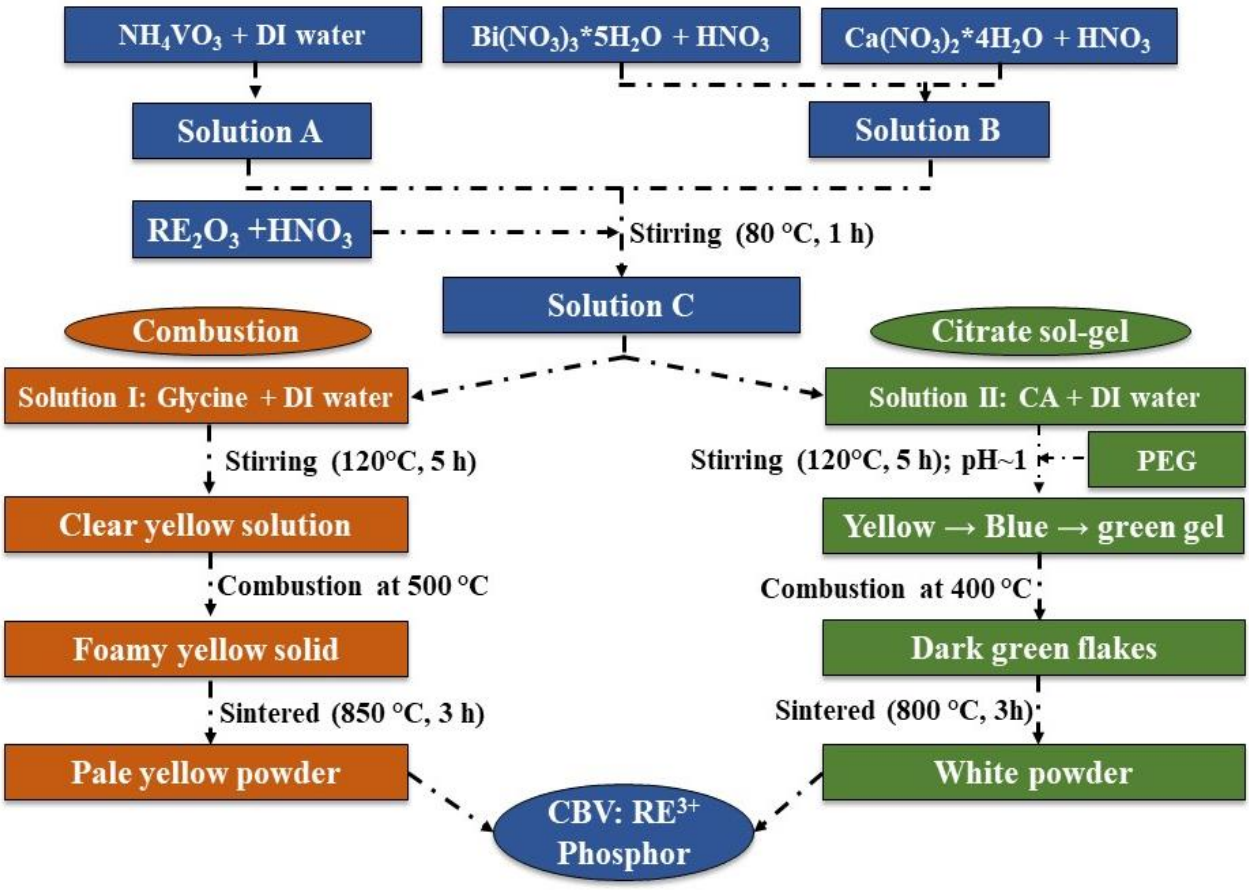

Figure 2.2. *Flow chart of CB and SG synthesized CBV: RE^{3+} phosphor*

2.3. Characterization techniques

The relevant characterization techniques are essential to know the various parameters for the optimization and effective utilization of the as-prepared phosphors in lighting devices. The as-prepared phosphors have been characterized using the standard instruments, which are utilized for the determination of the structure, morphology and luminescence behaviour of the phosphors. The experimental tools used for characterization of the as synthesized phosphors are discussed in detail in the subsequent sections.

2.3.1. Thermal analysis

The thermal behaviour of the precursors was studied via thermogravimetric and differential thermal analysis (TG-DTA) to determine physical properties of reaction products as a function of temperature, stress and environmental factors. Generally, the substance is heated in a controlled manner for the analysis of the substance. Thermal analysis provides insight of certain properties such as topography, phase transition, crystallization, adsorption, desorption, melting, enthalpy thermal capacity, weight changes, and thermal stability. However, in the present thesis work, thermogravimetric-differential thermal analysis (TG-DTA) has been done to know the crystallization temperature of the phosphor.

(i) Thermogravimetric analysis: In TGA, the mass or weight loss of a precursors is measured with gradual increase in temperature or time in a controlled atmosphere. A graph known as thermo-gram or thermal decomposition curve is plotted between weight percentage with respect to time or temperature. This plot provides the information about decomposition, oxidation, vaporization, sublimation and desorption. The weight change in TGA curve indicates adsorption or desorption of gases from the substance under observation. An increase in the mass indicates adsorption and decrease in the mass indicates desorption, whereas negligible mass change specifies stability of the substance.

(ii) Differential thermal Analysis (DTA): The first order derivative of mass versus time or temperature is termed as differential thermal decomposition curve [92]. The DTA is basically a refinement of the conventional procedure to study the phase transformations using time-temperature measurements while gradual heating of the precursors along with an inert reference material under same environment. The DTA technique involves the recording of both the temperature of sample and temperature difference between reference material and the sample under consideration as a function of time. Whenever a phase change takes place (comprise of absorption or evolution of heat), the difference between temperatures of sample and reference initiate to rise and after the completion of transformation, the difference of temperature declines. Hence, each phase transformations provides a peak in the DTA curve, which can be used to derive the information regarding temperature of each transformation, transformation heat and transformation rate. In the present thesis, TG-DTA were carried out using Perkin Elmer Pyris diamond (TGA/DTA/DSC) system as shown in Fig. 2.3.

Figure 2.3. *Perkin Elmer Pyris diamond (TGA/DTA/DSC) system*

2.3.2. X-ray diffraction (XRD)

X-ray diffraction is the standard and most significant non-destructive characterization tool used to investigate phase and structural properties of almost all the prepared materials. The X-rays are the electromagnetic waves with wavelength ranging in few Angstroms, which is comparable to interplanar spacing of atoms in the crystals. Therefore, it is technically possible to have successful diffraction of X-rays by crystal planes. The crystalline materials show periodic arrangement of atoms in three-dimensional array constituting the crystal planes, known as lattice. The smallest building block of crystal structure is known as unit cell. The translational vectors a, b and c specify the position of atoms in a lattice also known as the length of the edges, where α, β and γ are the angles between these vectors. The crystalline solids can be classified within the seven crystal systems, which are further sub-divided into 14 Bravais lattices. Every crystalline material has its exclusive diffraction pattern and the XRD data imitates the lattice structure of the unknown material and thus can be used for its phase identification. This technique was discovered in 1912 by Von Laue and can also be used in determination of crystallite size, lattice parameters, residual stress, microstrain and degree of crystallinity of materials [93]. The powdered samples are normally in the polycrystalline form, which constitute an aggregate of randomly oriented tiny crystallites. Therefore, in a powder sample, all possible orientations of lattice planes are presented with respect to a given direction.

(i) Bragg's Law: As stated earlier, the essential requirement of any diffraction experiment is that the incident X-ray must have wavelength comparable to the spacing between atoms of the target material. After incidence of a monochromatic X-ray beam on a set of lattice planes in a particular crystallite, it gets reflected from the surface and from the plane inside crystal. As shown in Fig. 2.4, these scattered waves from the top and bottom lattice planes interfere. Constructive interference and hence observable diffraction occurs when the two interfering

waves have path difference as an integral multiple of λ so that the Bragg's condition is satisfied

$$2d_{hkl} \sin \theta = n\lambda \quad (2.1)$$

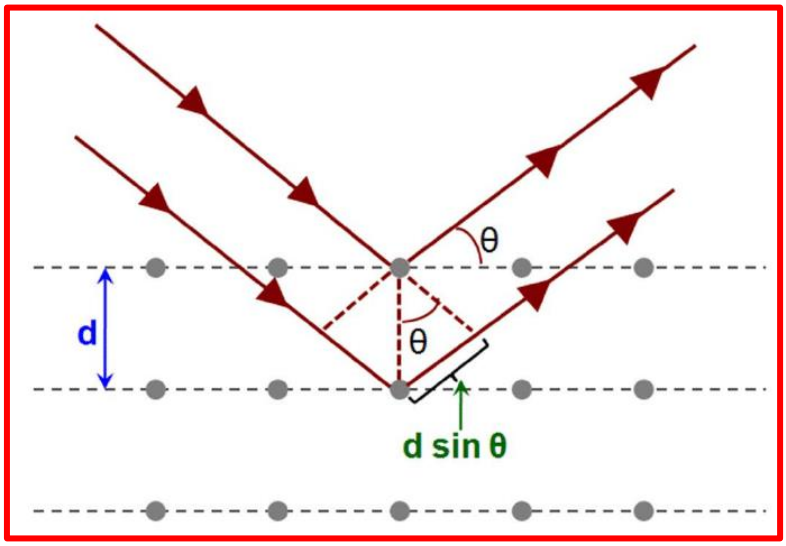

Figure 2.4. *Schematic diagram of Bragg diffraction from a set of planes/atoms*

where, θ is the angle of incident beam with lattice plane called as Bragg angle, d_{hkl} the spacing between planes labelled by Miller indices (*h k l*), λ is the incident X-ray wavelength and *n* represents an integer representing the order of the diffraction.

(ii) X-ray diffractometer*:* It has essentially three essential components viz. an X-ray tube to produce X-rays in the form of a collimated beam, a goniometer to provide a platform for sample holding and positioning and an X-ray detector which counts the number of X-rays diffracted from the crystal. Fig. 2.5 shows schematic of collecting data in the XRD. In this schematic, the collimated beam incident coming from the line focus of the X-ray tube diverges in the crystallographic plane of the sample until irradiation takes place. The receiving slit collects the diffracted X-ray beam converged from sample and send it to the detector.

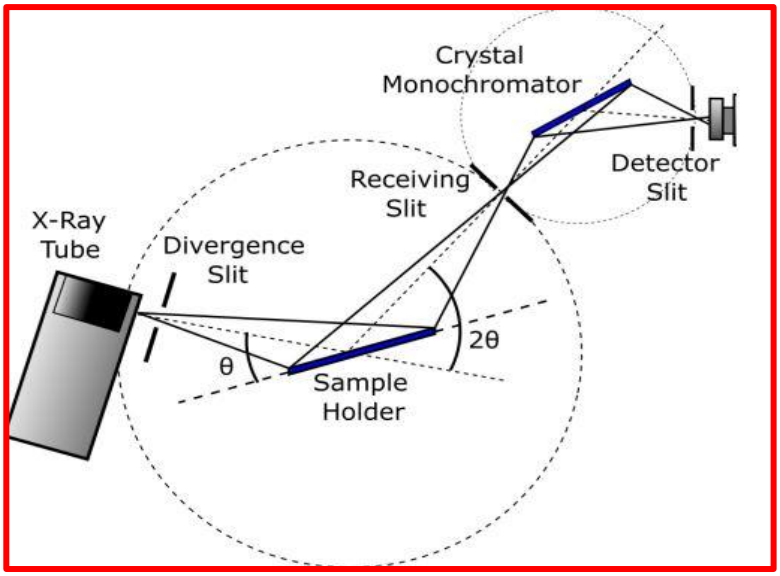

Figure 2.5. *Schematic arrangement of collecting data in the XRD*

In a typical XRD operation, data is recorded in *theta-2theta* mode. The sample stage and the detector is mounted at the θ axis and 2θ axis, respectively while keeping the X-ray tube fixed to the goniometer. The graph depicting intensities from different crystal planes with the corresponding 2θ values is called as a *diffractogram* [93].

(iii) Analysis of XRD data: The phase identification of the unfamiliar samples can be carried out by comparing the peaks of diffractogram with internationally accepted JCPDS (*Joint Committee on Powder Diffraction Standards*) database, which is a huge collection of reference patterns of known materials. This technique can also be used in estimating the crystallite size of materials by considering the peak broadening (full width at half maxima: FWHM). The crystallite size (D) can be calculated for the material using the Debye Scherrer's formula given as follows [73]:

$$D = \frac{0.9\lambda}{\beta \cos\theta} \tag{2.2}$$

where λ is the wavelength of Cu-K_α radiation (1.5406 Å) used in XRD and β symbolizes FWHM of the diffraction peak corresponding to a particular angle θ. Further, the crystallite size (D) and strain (ε) for the material can be calculated employing Williamson Hall (W-H)

equation, given by [73]:

$$\beta \cos\theta/\lambda = (k/D) + 4\varepsilon \sin\theta/\lambda, \text{ where } k = \text{shape factor} \quad (2.3)$$

In the present work, the XRD patterns have been recorded on Rigaku Miniflex 300 XRD analyzer with nickel-filtered Cu-K_α radiation as shown in Fig. 2.6(a). The accelerating voltage and tube current of the XRD machine have been set at 30.0 kV and 15 mA, respectively. Also, X-ray diffractometer (Bruker D8 Advance) providing nickel filtered X-rays (Cu-K_α radiation) is used for recording XRD data for some of the as-prepared samples, which is shown as Fig. 2.6(b).

Figure 2.6. *(a) Rigaku Miniflex 300 Analyzer and (b) Bruker D8 Advance X-ray diffractometer*

2.3.3. Rietveld analysis

It is a technique described by Hugo Rietveld to characterize crystalline materials using diffraction data obtained from powder diffraction method. The X-ray diffraction pattern is characterized by reflections obtained as intensity for certain angles. The *(h k l)* Miller indices of these reflections are useful in figuring out many facets of the structure of material.

The Rietveld method uses a least square fitting analysis to refine a theoretical line profile under "n" number of iterations to match the measured profile. This method uses predetermined parameters to minimalize the error between an experimentally observed data and a

hypothetically determined crystal structure and instrumental parameters (calculated pattern). Refinement parameters like background, peak shape, lattice parameters can be refined using a Rietveld refinement software such as Full Prof Suite. The Rietveld refinement is useful for quantitative phase analysis, microstructural analysis, texture and residual stress. For the determination of crystal structure, it requires reflection positions, cell size, space group symmetry, intensities and atomic positions. Thus, the parameters are refined to the precise values using least square fit approach.

2.3.4. Scanning electron microscope (SEM)

It is one of the versatile and resourceful equipments to provide thorough details of surface topography and microstructure of the materials over wide range of magnification. It is used to inspect topography of specimen or surface sensitive compositional information at a very high magnification.

(i) Basic principle and instrumentation: The basic principle underlying imaging process is collecting the ejected secondary electrons when surface of the specimen interacts with a finely focused electron beam that impinges on it. The sample should be conductive or by coating an extremely thin layer of gold/gold-palladium/carbon on the surface of non-conductive materials, they can be made conductive. The sample is mounted on a metallic platform after making its surface conductive and kept for scanning across the surface. In general, the electron beam is created by a thermal emission source, such as heated tungsten filament, or a crystal of lanthanum hexafluoride mounted on tungsten filament. An electron gun situated at the microscope top generates an electron beam. A vacuum vertical column in the microscope directs the electron beam. The beam travelling down towards the specimen is focussed by electromagnetic fields and condenser lenses around this vacuum column. To produce SEM image by collecting the secondary electrons, the electron probe is scanned in a raster (two dimensional) pattern across the specimen surface. The SEM image is made up of point by point and scan is accomplished by scan coils

(electromagnetic) and arc organized by scan generator. The secondary electrons are ejected from the specimen as it interacts with the primary electron beam. An electron detector (Photomultiplier tube: PMT) detects the ejected secondary electrons at each point in the scanned area. A cathode ray tube display the intensity of the emitted electron signal as brightness. The imaging can be done by two modes: first one is by secondary electron signal and the second one make use of backscattered electrons. The secondary and/or backscattered electrons are collected by detectors and amplified signal unveil on a display screen. The SEM employ electrons instead of light to produce a magnified image [94, 95]. The schematic diagram is shown in Fig. 2.7.

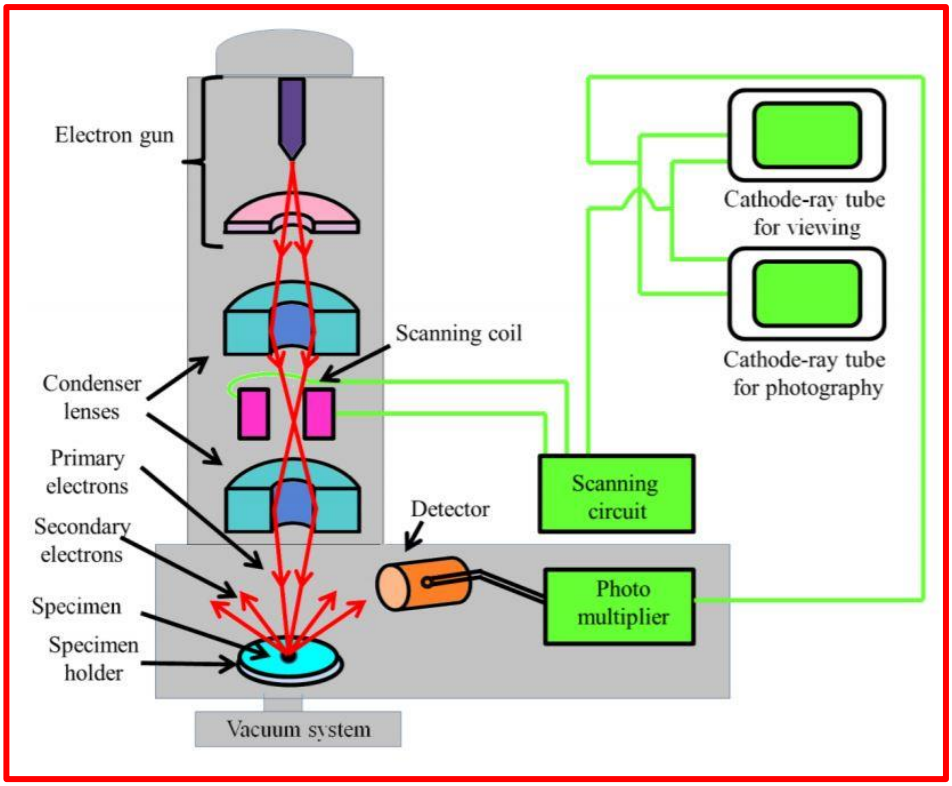

Figure 2.7. *Schematic diagram of the SEM instrument*

(i) SEM image analysis: The magnification (M) of displayed SEM image can be altered by varying the scan width of the electron probe. The magnification of the scanned image can be calculated using the expression M= D/d, where D is the width of monitor screen on which the image is displayed, and d is the scan width of the electron probe. As the size of monitor is fixed, the scan width decreases with increase of magnification and vice versa. The size distribution and other

related statistical analysis of the particles can be done by processing SEM images. The significant characteristic information such as topography (surface appearance and texture), morphology (shape, size and arrangement of particles), composition, atomic arrangement and their degree of disorder can be obtained from SEM micrographs.

The set-up used to conduct morphological observations are JEOL JSM 7100F & JEOL IT200 SEM machines shown as Fig. 2.8(a) and Fig. 2.8(b), respectively.

Figure 2.8. *(a) JEOL JSM 7100F SEM and (b) JEOL IT200 SEM*

2.3.5. Diffuse reflectance (DR) spectroscopy

DR spectroscopy is a proficient and well established technique closely linked to UV/Vis absorption spectroscopy to determine the optical and spectroscopic properties of the solids at microscopic level. For both the methods, the visible light acts as an excitation source. In the case of UV/Vis spectroscopy, the relative variation in transmitted light is measured when it travels through a transparent media/material. But in case of DR spectroscopy, relative variation in the amount of light reflected off the intractable surface or crystalline materials is measured. In general, when light is incident on the sample, some amount of light gets absorbed, some gets reflected back, and some get scattered in all possible directions within the sample as shown in Fig. 2.9.

Figure 2.9. *Incident and reflected beam through the sample under investigation*

For in-homogeneously distributed particles, the resultant of reflected, refracted, diffracted, and absorbed light in all possible directions included in diffuse (or volume) reflection, whereas in homogeneous media directional (regular) reflection is observed from the boundary of a plane phase. Ideally, the angular distribution of the reflected radiation should be independent of incidence angle to observe diffuse reflectance. A reflectance spectrum is basically collection of electromagnetic radiation reflected from the surface in correlation with the frequency or wavenumber. Reflectance is the ratio of power between the reflected radiation to the power of incident radiation [96].

(i) Working of diffuse reflectance set-up: As discussed above, in diffuse reflectance setup, there exist a light source, a trifurcated fibre optic cable with a probe cylinder, spectrometer connected to the computer equipped with portable software for data collection. A Tungsten-Halogen light source providing light in the visible range is employed. A trifurcated fiber optic-cable is connected to probe cylinder. The trifurcated fibre bundle composed of a single illuminating fibre at centre and several fibres collecting signal from the sample arranged in a ring around central fibre at an appropriate source to detector distance. The signal from collecting fibres is received by the spectrometer. Finally, the spectra in the visible range is observed with the help of computer software installed on a standard computer system attached to spectrometer. When diffuse reflection spectroscopy is used, the backscattered signal is detected and compared to the backscattered signal from a reference material [96].

Polycrystalline powder of $BaSO_4$ can be used as a reference.

In the present thesis, the diffuse reflectance (DR) measurements were carried out using optical fibre assembled system and spectrometer (FLAME) by Ocean Optics as shown in Fig. 2.10.

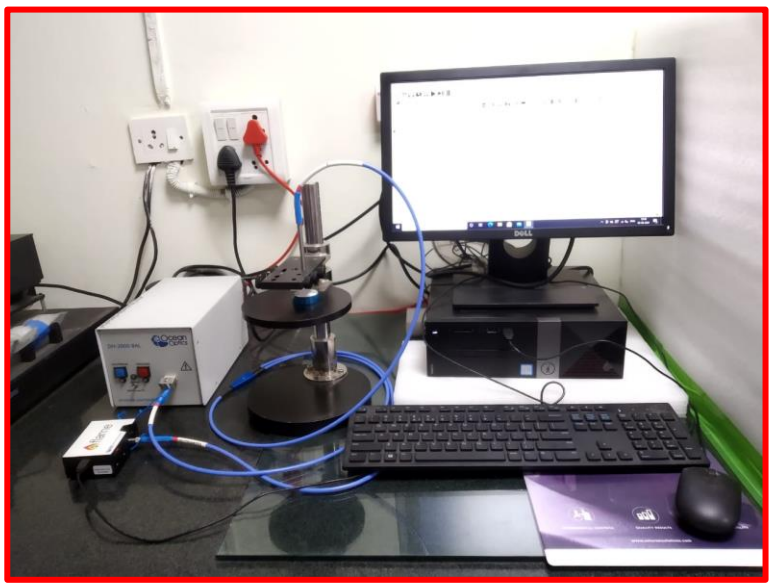

Figure 2.10. *Ocean optics diffuse reflectance set-up*

***(ii)* Analysis of DR *spectrum*:** It is obtained by collection of diffuse reflected electromagnetic radiation by mat or dull surfaces textured like powders as a function of frequency or wavelength. The DR spectrum of a solid material can be observed as the inverse of its absorbance spectra. It provides information about possible absorption wavelengths for the phosphor at which it can be excited effectively. Moreover, the optical band gap can be estimated from the DR spectra of as-synthesized samples using the relation as mentioned below [74]:

$$\alpha h\nu = A(h\nu - E_g)^n \tag{2.4}$$

where optical band gap is E_g, absorption coefficient is α, hν characterises the photon energy and A is a coefficient; the value of n can be 1/2, 2, 3/2 and 3 in accordance to direct allowed, indirect allowed, direct forbidden and indirect forbidden electron transitions, respectively. Further, reflectance data can be converted to reflection function (F(R)) known as Kulbeka-

Munk's function given as follows:

$$F(R) = \frac{(1-R)^2}{2R} = \frac{K}{S} \quad (2.5)$$

In the above expression, R, K and S are the reflection constants, molar absorption coefficient and scattering constant, respectively. Using the above equations, the following formula can be deduced:

$$[F(R_\infty)h\nu]^{1/n} = B(h\nu - E_g) \quad (2.6)$$

where B represents the coefficient. Consequently, the optical band gap can be evaluated by extrapolating the $[F(R_\infty)h\nu]^{1/n}$ straight line to zero.

2.3.6. Photoluminescence (PL) spectroscopy

PL spectroscopy is a multi-purpose, non-destructive and powerful analytical tool for exploring the luminescent properties of the proposed material. It involves the analysis of events that includes the emission of light from a sample via photoexcitation. A plot between the intensity of emitted light and wavelength provides the photoluminescence spectrum. The excitation spectrum in turn is obtained by monitoring a specific and fixed emission band in a certain range of wavelengths. The observed bands in excitation spectrum will be further employed to record the emission spectrum. In both type of spectra, the photoluminescence intensity is plotted along the ordinate while wavelength changes are displayed along the abscissa. Thus the photoluminescence spectra is composed of excitation and emission spectra.

(i) Procedure and Instrumentation: The spectrophotometer primarily consists of three basic units, excitation source, sample holder and detector. The source of excitation employed should give continuum spectrum in place of line spectra. Usually, Xenon lamp is utilized as excitation source as it can provide a relatively continuous light output of high intensity beyond 220 nm wavelength. A monochromator is associated with the assembly which allows only selected wavelength of light. The excitation monochromator includes diffraction gratings

with larger aperture to collect the brightest excitation light which contributes to higher sensitivity of the spectrofluorometer. The sample holder is filled with the phosphor sample, which is flashed with light from excitation monochromator. From the sample, the emission monochromator selectively collects luminescent light and then a light detector as photomultiplier tube (PMT) measures intensity of fluorescence. PMT is regarded as good current source with considerable spectral response. The unstable light emission and non-uniformity in radiation spectrum of light from Xenon lamps results into greater noise and signal distortion. To get off from this problem, a light-source compensation system is used in which a PMT with a reference cell is installed beside the excitation monochromator to monitor and correct the portion of excitation light and to feed the resultant signal back to the detector [97, 98]. The excitation and emission spectra were recorded at room temperature by selecting the wavelength scan mode at a low or medium scan speed, excitation and emission slit width 0.1 nm and high voltage PMT setup. The decay analysis is carried out in time scan mode. For TR-PL, the pulsed excitation source is used. For TD-PL, the temperature of sample is raised by a heating apparatus and then PL measurements are done at several higher temperature.

(ii) **Data Analysis:** With regard to luminescent materials, when energy of incident photon is equal or greater than the energy bandgap, excitation of charged carriers is produced. When these excited carriers relax radiatively, photons are emitted. Then PL spectrum can be collected and analysed and hence it can provide information about optical transitions of the electronic states and recombination mechanisms involving radiative and nonradiative transitions within the luminescent material. During the PL measurement, we can also change other external parameters like temperature, excitation power, pressure and external perturbation such as electric or magnetic field so that we can get more information about electronic states and bands.

The life time information of excited state can also be obtained if we use a pulsed excitation source. Then the setup is called time resolved (TR)-PL. Basically, the PL intensity is affected by the radiative (τ_R) and non-radiative (τ_{NR}) recombination lifetimes. The lifetime can be obtained as the sum of radiative and non-radiative decay rates. The lifetime of the excited state for a material is exponential. After fitting the TRPL data with single, bi- or tri-exponential equations, we can understand some detailed information about the nonradiative relaxations. Thus, TRPL is a very powerful tool to analyze the nonradiative process in the phosphors.

The thermal stability of the phosphor is a pre-requisite for lighting applications, which can be obtained by measuring photoluminescence spectra at elevated temperatures. Then the set-up is called as Temperature dependent PL. In general, the PL profile should not vary at elevated temperatures but the intensity may decrease due to thermal quenching. For a better phosphor, the thermal quenching should be minimum indicating more thermal stability of the phosphors at elevated temperatures.

In the present work, the luminescent features of the prepared phosphors are measured by employing various spectrofluorophotometers shown in Fig. 2.11 (a-d).

(a) Edinburgh FLSP900
(b) HORIBA Scientific-FluoroLog3
(c) JASCO FP 8300 Spectrofluorophotometer
(d) Ocean Optics FLAME-S-XR1-ES Spectrofluorophotometer for TD-PL studies

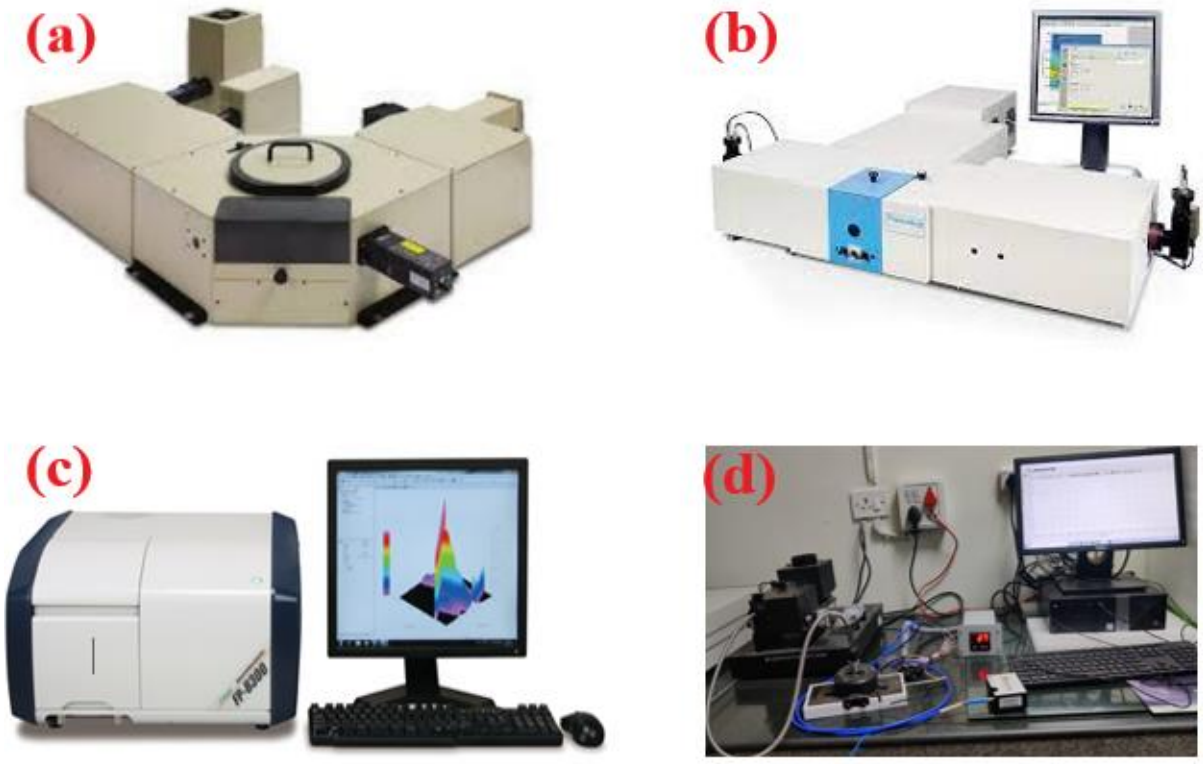

Figure 2.11. *(a) Edinburgh FLSP900, (b) HORIBA Scientific-FluoroLog3, (c) JASCO FP 8300 Spectrofluorophotometer and (d) Ocean Optics FLAME-S-XR1-ES Spectrometer*

Chapter 3
Photoluminescence properties of Eu^{3+} doped calcium bismuth vanadate phosphors for luminescent devices

Single phase Eu^{3+} activated calcium bismuth vanadate ($CaBiVO_5$) phosphors synthesized successfully using solid state reaction method. X-ray diffraction (XRD) analysis confirms the pure phase formation and scanning electron microscope (SEM) micrographs exhibit inhomogeneous particle formation with irregular morphology of Eu^{3+} doped $CaBiVO_5$ (CBV) phosphor. The photoluminescence excitation (PLE) spectrum indicates significant absorption in the ultraviolet (UV) and near ultraviolet (n-UV) spectral regions for un-doped CBV sample, whereas Eu^{3+} doped CBV phosphors reveal various sharp absorption bands in n-UV and blue region along with the host absorption bands. Trivalent europium activated CBV phosphors under 342 nm excitation exhibit dominant red emission peak at 613 nm wavelength accompanied by a weak broadband originating from VO_4 groups, whereas the phosphors under 464 nm excitation, exhibit similar emission profile with most intense one centered at 613 nm by excluding host emission bands. The energy transfer mechanism and the probable cause for concentration quenching beyond 4.0 mol% of Eu^{3+} ions concentration have been discussed in detail. The CIE chromaticity coordinates for the optimized phosphor, (0.551, 0.398) and (0.639, 0.358), situated in the reddish-orange and red region under 342 and 464 nm excitations, respectively. The CIE coordinates calculated based on the emission spectra measured under 464 nm excitation are close to the commercial phosphor Y_2O_2S: Eu^{3+} (0.622, 0.351). All the above mentioned results support the utilization of Eu^{3+} doped CBV phosphor as a potential red emitting component for luminescent devices.

3.1. Introduction

In recent years, the escalating demand for the annual energy consumption and other environmental issues force the population to shift towards the alternatives for conventional lighting sources [99, 100]. Nowadays, w-LEDs are acting potentially as a substitute for traditional incandescent and fluorescent lamps on account of their unprecedented luminous efficiency, low energy consumption, less emission of harmful gases, high brightness, compact design, fast switching and long working lifetime [101-104]. Predominantly, phosphor based w-LEDs approach has become commercial includes the accomplishment of white light emission via combination of blue light emitting InGaN chip and yellow phosphor (YAG: Ce^{3+}) [105-106]. Despite of its several advantages over RGB-LEDs like low cost, simplicity in fabrication and high brightness, such w-LEDs have some drawbacks like low color rendering index (CRI < 70), high correlated color temperature (CCT >7765 K), halo effect and low efficiency due to lack of the red component [107]. Therefore, researchers over the globe proposed alternative approaches to deal with this obnoxious problem such as "blue LED coated with green and red phosphors" and "n-UV LED coated with an appropriate mixture of RGB phosphor" [108, 109]. Apparently, both the above mentioned approaches obligate the synthesis of a promising red emitting phosphor. Currently, commercially available red phosphor (Y_2O_2S: Eu^{3+}) gives excellent red emission but lacks on account of chemical and thermal stability in comparison with green (ZnS: Cu^{+}, Al^{3+}) and blue phosphor ($BaMgAl_{10}O_{17}$: Eu^{2+}) [110, 111]. Moreover, the sulphide based phosphor is not environmental friendly phosphor that necessitates exploring new environmental friendly red phosphor with excellent thermal and chemical stability. Recently, Europium (Eu^{3+}) doped phosphors owing to characteristic *f-f* transitions, are gaining a noteworthy attention for applications as red component in luminescent devices such as plasma display panels (PDPs), lasers, photovoltaic cells, and backlight displays [112-113] . Hence, Eu^{3+} doped appropriate host lattice may be utilized as an efficient red phosphor.

In the present work, an investigation has been made on a new calcium bismuth vanadate ($CaBiVO_5$: CBV) host lattice doped with different concentrations of Eu^{3+} ions synthesized via SSR method. The prepared phosphors exhibit excitation and dopant concentration dependent tunable and intense red emission with high purity. Therefore, structural, morphological and luminescent properties of the Eu^{3+} doped CBV phosphors have been studied extensively to delve into the possibility of utilising it as a red phosphor in luminescent devices.

3.2. Sample preparation

A series of $CaBi_{1-x}VO_5$: xEu^{3+} ($1.0\ mol\% \leq x \leq 6.0\ mol\%$) phosphors with different doping concentrations of Eu^{3+} ions have been synthesized using conventional SSR technique as described in section 2.2.1 and flow chart followed while synthesizing phosphor is shown in Fig. 2.1.

3.3. Results and discussion

3.3.1. Thermogravimetric studies

Fig. 3.1 displays the thermogravimetric analysis (TGA) of the un-sintered $CaBiVO_5$ composition in the temperature range of 90-900 °C. The TGA curve depicts that weight loss during the formation of $CaBiVO_5$ sample proceeds through two distinct steps. The initial weight loss of 5.05 % occurs in the range of 90-234 °C, has been attributed to the evaporation of surface moisture and decomposition of residual organic species such as acetone used for homogeneous mixing. Then, a significant weight loss of 10.866 % takes place with an increase in temperature up to 726 °C, is ascribed to the degradation of organic material from the synthesized sample, which could possibly be due to the elimination of CO_2, NH_3, and H_2O molecules. As the temperature is further increased, a solid state reaction occurs amongst the chemicals characterized by a nominal weight loss. The mixture has been sintered at various

temperatures beyond 750 °C to identify the pure phase forming temperature for the $CaBiVO_5$ phosphors.

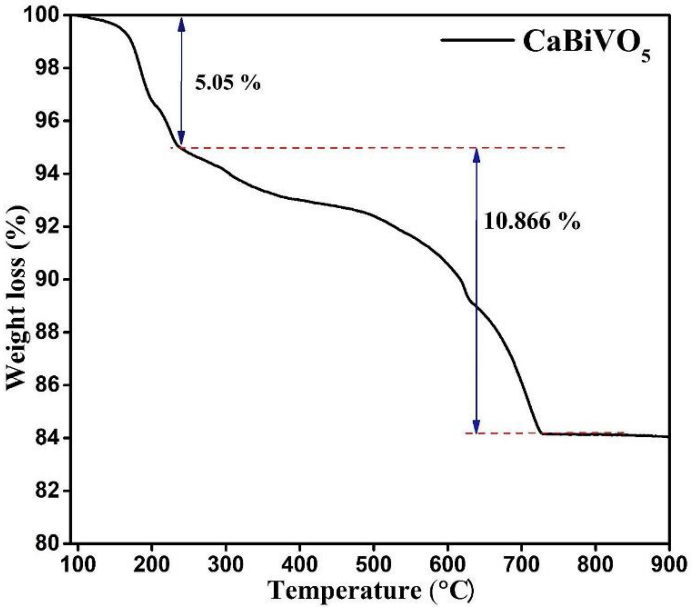

Figure 3.1. *TGA curve for $CaBiVO_5$ (CBV) sample*

3.3.2. Structural studies

Fig. 3.2(a) represents the XRD patterns for $CaBiVO_5$ (CBV) powders sintered at various temperatures by taking reference of TGA results. It is evident from Fig. 3.2(a) that the phase formation begins at 750 °C with the presence of some impurity peaks and mismatch of relative peak intensities. The impurity peaks gradually diminish with increasing the calcination temperature and pure phase of CBV sample obtained at 950 °C. All the peaks in the diffraction pattern of CBV sample sintered at 950 °C for 3 h are well matched to the standard data of $CaBiVO_5$ (JCPDS card no. 81-1775), which confirms the monophasic formation of $CaBiVO_5$ as shown in Fig. 3.2 (a). As-synthesized phosphors crystallize in an orthorhombic unit cell belong to space group D_{2h}^{15} −Pbca with lattice parameters a = 11.2022 Å, b = 5.4283 Å, c = 15.5605 Å and cell volume 946.22 $Å^3$. Based on the observed XRD patterns, the CBV structure has been refined by adopting the Rietveld powder diffraction profile fitting technique employing FullPROF suite software. For the Rietveld refinement of the as-prepared sample, we have utilized the initial values of lattice parameters, space group and Wyckoff positions of

the atoms reported elsewhere [114]. A pseudo-Voigt function, to simulate the peak shape and linear interpolation between a set background points with refinable heights parameters in the software have been adopted. Fig.3.2(b) represents the refined and experimental XRD pattern along with an acceptable deviation from refined data for the CBV samples. The refinement results are listed in Table 3.1 and confirm the pure phase formation of CBV sample as the lattice parameter values do not vary much from the initial values and also from residual factors (R_{wp}, $R_{p,}$ and χ^2) values.

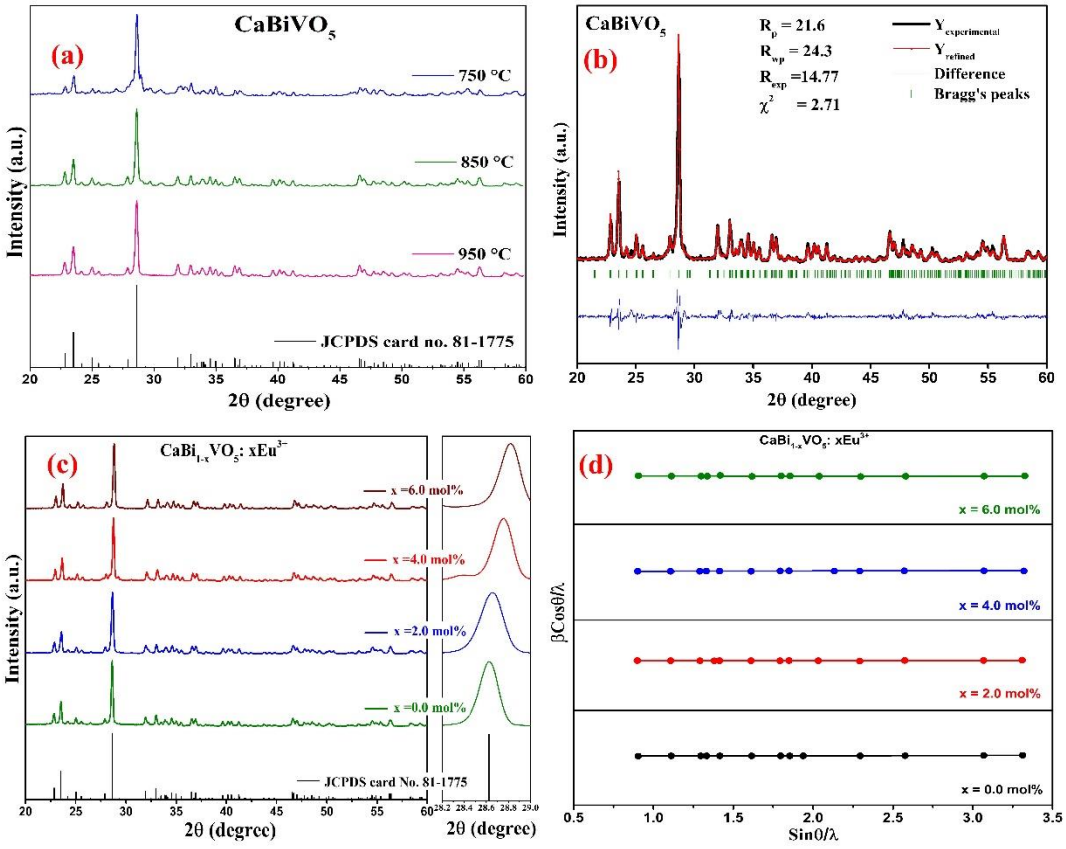

Figure 3.2. *(a) XRD patterns of CBV samples: standard data for $CaBiVO_5$, samples calcined at 750 °C, 850 °C and 950 °C for 3 h, (b) Rietveld refined data of $CaBiVO_5$ sample, (c) XRD patterns of $CaBi_{1-x}VO_5$: xEu^{3+} (x = 0.0, 2.0, 4.0, and 6.0 mol%) and (d) W–H plot of $CaBi_{1-x}VO_5$: xEu^{3+} (x = 0.0, 2.0, 4.0, and 6.0 mol%)*

The absence of any diffraction peaks corresponding to Eu_2O_3 and complete agreement with the standard XRD data also supports the successful doping as depicted in Fig. 3.2(c). The values of ionic radii for Ca^{2+} and Bi^{3+} ions are 1.06 Å and 0.96 Å, respectively. So, when the crystal structure is doped with Eu^{3+} ions ($R_{Eu^{3+}}$ = 0.947 Å), it can favorably replace Bi^{3+} ions in

the lattice due to comparable radii and same valence state. Upon keen observation, it is found that the diffraction peaks of CBV: xEu^{3+} phosphors shift towards higher angle with increasing Eu^{3+} concentration in comparison with standard data. The most intense peak present in XRD pattern is separately plotted and shown on the right side of Fig. 3.2(c) to reveal the peak shift clearly. It may be explained that the substitution of smaller Eu^{3+} ions in larger Bi^{3+} ions leads to the decrease in interatomic spacing and finally the contraction of the unit cell. It will cause strain in the host lattice and eventually yields to shifting of diffraction peaks towards larger angles [115].

Table 3.1. *Rietveld refined parameters of $CaBiVO_5$ sample*

Formula	**$CaBiVO_5$**
Structure	Orthorhombic
Space group	D_{2h}^{15} −Pbca
a (Å)	11.1973
b (Å)	5.4246
c (Å)	15.5670
α=β=γ	90 °
Z	8
R_p	21.56
R_{wp}	24.30
χ^2	2.71
V ($Å^3$)	945.61
Density (mg/m^3)	5.33

Further, the crystallite size (D) and strain (ε) for CBV :xEu^{3+} (where x = 0.0, 2.0, 4.0 and 6.0 mol%) have been calculated employing Williamson Hall (W-H) equation (2.3) [116]. Thus, the computed average crystallite size and strain values for $CaBi_{1-x}VO_5$: xEu^{3+} (x = 0.0, 2.0, 4.0 and 6.0 mol%) from W-H plot (shown in Fig. 3.2(d)) are 38.02, 37.82, 32.32 and 28.85 nm and 0.00028, 0.00033, 0.00035 and 0.00047, respectively. The decrease in crystallite

size with increasing Eu^{3+} ion concentration ascribed to the increase in strain owing to the replacement of Bi^{3+} ions by Eu^{3+} ions of comparatively smaller radii [93, 117, 118]. The obtained average crystallite size values are in good agreement with that of the values calculated using Debye-Scherrer formula given as equation (2.2) and the values for $CaBi_{1-x}VO_5:xEu^{3+}$ (x = 0.0, 2.0, 4.0 and 6.0 mol%) are found to be 45.10, 39.24, 35.78, and 31.05 nm, respectively.

3.3.3. Morphological studies

SEM images recorded for $CaBi_{1-x}VO_5$: xEu^{3+} (x= 4.0 mol%) at different resolutions have been displayed in the Fig. 3.3 (a&b). The SEM micrographs reveal the microcrystalline structure formation due to agglomeration of grains obtained by sintering the sample at high temperatures. The particle size is irregular and ranging from 1 - 20 μm. Particle size in micrometer range is adequate to utilize CBV phosphors in w-LEDs, since other commercial phosphor's particle size currently available in the market are also of few micrometers [119].

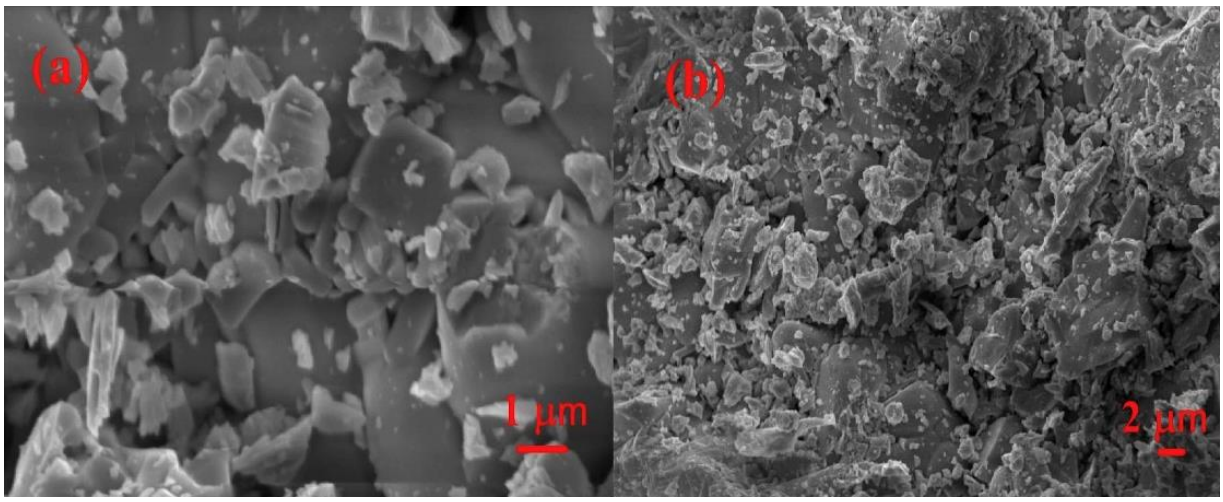

Figure 3.3. *SEM micrographs of as-synthesized $CaBi_{1-x}VO_5$, (x = 4.0 mol%) phosphor at different resolutions (a) 1 μm and (b) 2 μm*

3.3.4. Photoluminescence properties

The photoluminescence excitation (PLE) and emission spectra of undoped CBV sample have been shown in Fig. 3.4(a&b). The PLE spectral measurements have been carried out by monitoring the emission at 542 nm wavelength. The excitation band (Fig. 3.4(a)) can be

resolved into two broad peaks located at 275 and 316 nm corresponding to $^1A_1 \rightarrow {}^1T_2$ and $^1A_1 \rightarrow {}^1T_1$ transitions of $[VO_4]^{3-}$ groups, respectively [120]. The emission spectrum (Fig. 3.4(b)) for CBV excited under 316 nm wavelength, reveals a weak broad emission band ranging from 400 nm to 680 nm and centered at 542 nm corresponding to $^3T_1 \rightarrow {}^1A_1$ transition of $[VO_4]^{3-}$ groups [121, 122]. Z. Pei et al. have studied host luminescence for $CaBiVO_5$ and observed strong luminescence at liquid helium temperature in comparison to the luminescence at RT due to thermal quenching. Weak luminescence observed in $CaBiVO_5$ due to the presence of small amount of Ca/Bi disorder in $CaBiVO_5$ similar to $Ca_4BiV_3O_{13}$ and $Sr_2Bi_3V_3O_{14}$ [122].

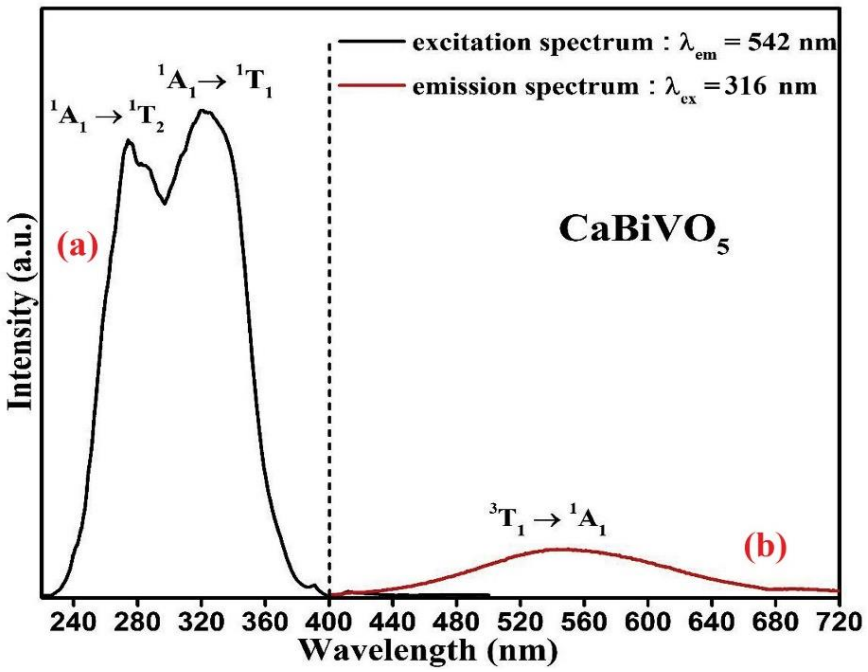

Figure. 3.4. (a) *PLE spectrum monitored at 542 nm wavelength and (b) emission spectrum under 316 nm excitation of $CaBiVO_5$ host lattice*

Fig. 3.5 represents the PLE spectra of Eu^{3+} doped CBV phosphors at various doping concentrations monitored at intense Eu^{3+} emission wavelength (λ_{em}= 613 nm). It exhibits intense broadband at 342 nm similar to the undoped sample. This intense band might be due to an overlap of $O^{2-} \rightarrow Eu^{3+}$ charge transfer (CT) transitions and transitions of the VO_4 group. Along with the broadband in the PLE spectra, five sharp excitation bands observed at 382, 393, 415, 464 and 488 nm. These bands have been attributed to the transitions of Eu^{3+} ion from its

ground state $^7F_0$ to the different excited states $^5L_7$, $^5L_6$, $^5D_3$, $^5D_2$ and $^5D_1$, respectively [123]. These results circumstantiate that the Eu^{3+} doped CBV phosphors can be efficiently excited by UV, n-UV and blue light, which further support the potentiality of CBV phosphors. Amongst these excitation bands, the broad CT band centered at 342 nm is most intense, and another located at 464 nm wavelength also exists with an appreciable intensity.

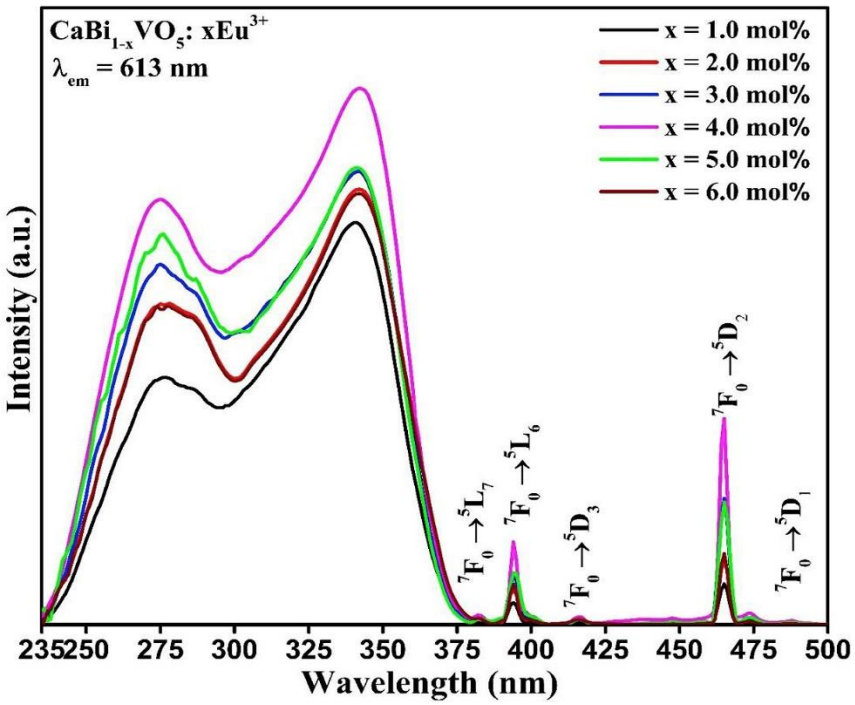

Figure 3.5. *PLE spectra of $CaBi_{1-x}VO_5:xEu^{3+}$ (1.0-6.0 mol%) monitored at 613 nm wavelength*

Fig. 3.6(a) represents the emission spectra for varying doping concentrations of Eu^{3+} ions in CBV phosphors excited under 342 nm wavelength. The emission spectra as shown in the Fig. 3.6(b) is normalized at the most intense peak of 613 nm to reveal energy transfer from host to Eu^{3+} ions. It exists in two parts, one is weak broad emission band similar to un-doped sample has been observed due to the transition of $[VO_4]^{3-}$ groups and second part is that sharp bands located at 580, 593, 613, 653 and 704 nm wavelengths attributed to the transitions between Eu^{3+} ion energy levels viz $^5D_0 \rightarrow {}^7F_J$ (where J = 0, 1, 2, 3, 4), respectively [124]. Along with these emission bands, two more peaks located at 537 and 558 nm wavelengths overlapped with host emission are corresponding to the bands originated from $^5D_1 \rightarrow {}^7F_J$ transitions (where

J = 1 and 2 respectively) of Eu^{3+} ions [125]. The inset of Fig. 3.6(a) shows the effect of Eu^{3+} ions concentration on intensity of host emission as well as Eu^{3+} emission ($^5D_0 \rightarrow {}^7F_2$)

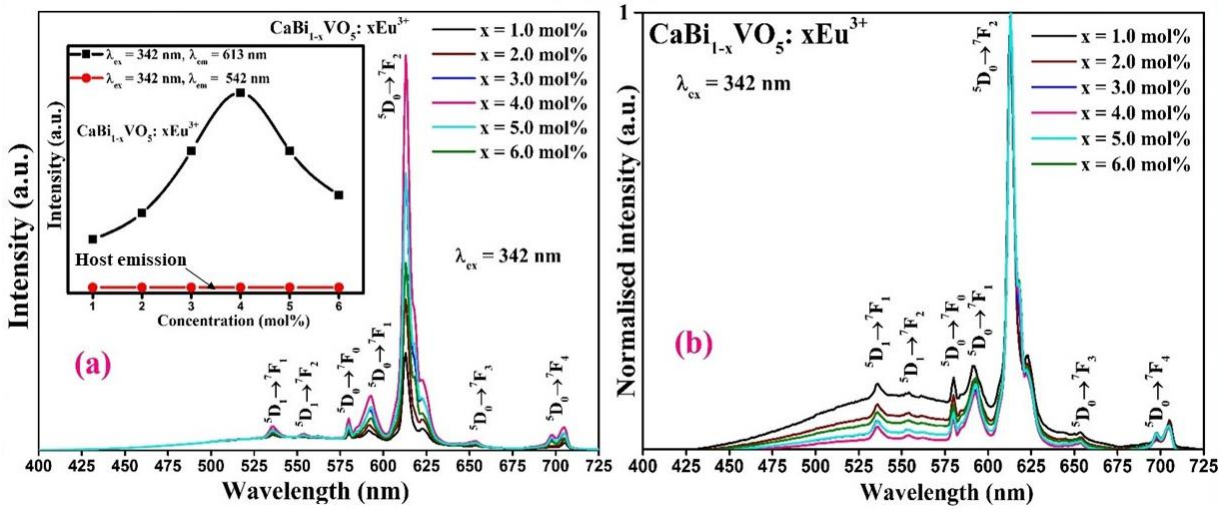

Figure 3.6. *(a) Emission spectra of $CaBi_{1-x}VO_5:xEu^{3+}$ ($1.0\ mol\% \leq x \leq 6.0\ mol\%$) under 342 nm excitation (Inset: emission intensity variation with Eu^{3+} ion concentration) and (b) Emission spectra normalized at 613 nm of all Eu^{3+} doped CBV phosphors*

It can be observed from the inset that with increasing the concentration of Eu^{3+} ions, emission intensity of the transition $^5D_0 \rightarrow {}^7F_2$ enhances appreciably up to 4 mol% of Eu^{3+} ions concentration and becomes dominant while host emission remains almost unaffected. It indicates that energy transfer from $[VO_4]^{3-}$ groups to Eu^{3+} ions may occur under 342 nm excitation wavelength. When the phosphors are excited at this wavelength, firstly $[VO_4]^{3-}$ groups may relax non radiatively to $^1T_1$ or $^3T_1$ state, and eventually, energy transfer from $[VO_4]^{3-}$ groups to the $^5D_0$ energy level of Eu^{3+} is expected to happen. However, if and only if the aforementioned process is involved, emission corresponding to Eu^{3+} ions should not enhance significantly with increasing concentration. Therefore, it can be concluded that the intense excitation band centred at 342 nm wavelength is an overlap of CT band ($O^{2-} \rightarrow Eu^{3+}$) and transition originated from VO_4 groups [125, 126].

Fig. 3.7(a) represents the emission spectra for CBV: xEu^{3+} (x = 1.0-6.0 mol%) phosphors excited under 464 nm wavelength. The emission spectra of all Eu^{3+} doped CBV phosphors represent only peaks corresponding due to Eu^{3+} ions, discussed previously.

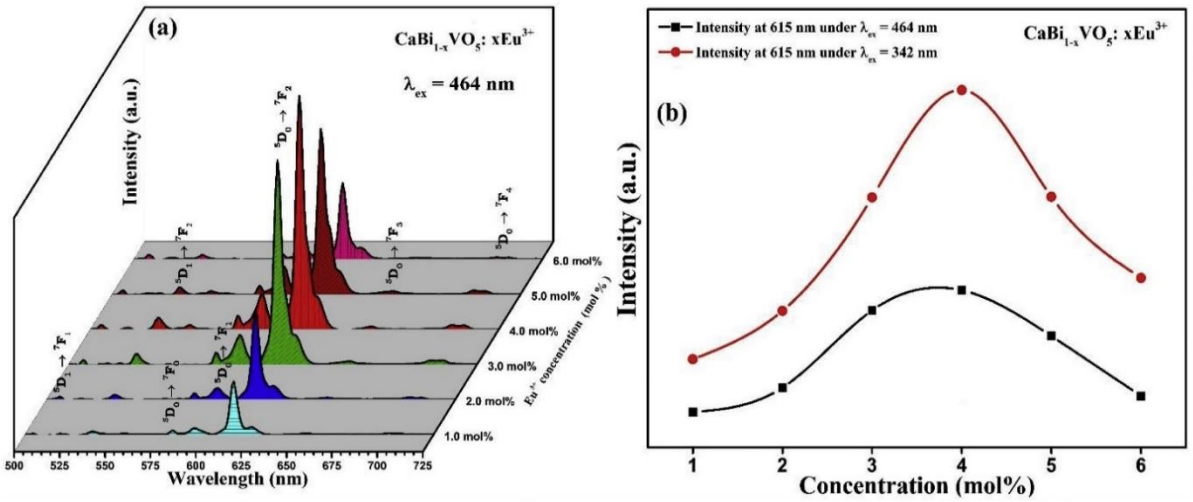

Figure 3.7. *(a) Emission spectra of $CaBi_{1-x}VO_5:xEu^{3+}$ (1.0-6.0 mol%) under 464 nm excitation and (b) Eu^{3+} ions concentration dependence on emission intensity of CBV phosphors*

The emission peak located at 593 nm in orange (O) region corresponds to the magnetic dipole (MD) allowed transition ($^5D_0 \rightarrow {}^7F_1$) and the other located at 613 nm in red (R) region corresponds to the forced electric dipole (ED) allowed transition ($^5D_0 \rightarrow {}^7F_2$). The former MD allowed transition follows the selection rule $\Delta J = 1$, while latter follows the selection rule $|\Delta L| \leq 2$; $|\Delta J| \leq 2$, which is a hypersensitive transition and highly influenced by the crystal field environment [127]. The dominance of emission energy distribution in the red region conveys that Eu^{3+} ions have been located at low symmetry sites without an inversion center [128]. The inversion symmetry distortion degree of the environment in the vicinity of Eu^{3+} ions can be represented by the integrated intensity ratio value of ED (R) and MD (O) transitions, hence termed as asymmetric ratio. The asymmetric ratio (R/O) has been calculated for optimized (4 mol%) Eu^{3+} doped CBV phosphor under 464 nm excitation, which comes out to be 6.67. The high value of asymmetric ratio for 4.0 mol% of Eu^{3+} doped CBV phosphor suggests high purity of red color emission. The emission intensity of the peaks corresponding to Eu^{3+} ions at λ_{ex} = 342 and 464 nm with varying Eu^{3+} ions concentration is shown as Fig. 3.7(b). It can be

easily seen that the emission intensity of the characteristic peaks of Eu^{3+} rises with the increase in Eu^{3+} ions concentration up to 4.0 mol%, after which the emission intensity of Eu^{3+} ions is quenched. It provides that the optimized Eu^{3+} ions concentration in CBV phosphors comes out to be 4.0 mol%. The decrease in the luminescence intensity with increasing concentration of Eu^{3+} ions beyond 4.0 mol% is due to non-radiative energy transfer among Eu^{3+} ions and is termed as concentration quenching. Blasse et al. propounded that the fluorescence quenching at higher concentration of activator occurs as the distance between luminescent centers decreases with an increase in activator ion concentration. It leads to possible non-radiative energy transfer among activator ions instead of emitting the excitation energy radiatively [46]. These non-radiative energy transfer may be explained in terms of either resonance energy transfer (RET) or cross relaxation among Eu^{3+} - Eu^{3+} ions [129]. The non-radiative energy transfer mainly depends on the critical distance (R_c) between Eu^{3+}-Eu^{3+} ions, which can be calculated according to the formula given by equation (1.13) [129]. The critical distance for the CBV host lattice is found to be 17.81 Å by considering the parameters V = 0.94622 nm^3, X_c = 0.04 and N = 8. The energy transfer through exchange interaction generally takes place when R_c is typically close to 5 Å [6, 130]. In the present system, the non-radiative energy transfer takes places through multipolar interaction, since the critical distance is far from the value (5Å). The nature of the multipolar interaction can be determined using Dexter's theory using the equation (1.14) [131, 132]. The different values of Q such as Q=6, 8 and 10 represent electric dipole-dipole, dipole-quadruple and quadruple-quadruple interaction, respectively. A graph of log (I/x) vs. log x for concentrations higher than 1.0 mol% is shown in Fig. 3.8, based on the emission spectra of $CaBi_{1-x}VO_5$: Eu^{3+} excited under 464 nm wavelength. The slope of the graph is found to be 1.834 and the calculated value of Q is 5.50, which is close to 6, confirms the energy transfer process in the present case occurs due to the electric dipole-dipole interaction [133]. The possible transitions between energy levels of Eu^{3+} ions and partial energy

transfer between $[VO_4]^{3-}$ and Eu^{3+} ions in a schematic manner have been demonstrated in Fig. 3.9. In the energy level scheme of VO_4 groups, $^1A_1$ represents the ground state while $^1T_2$, $^1T_1$ and $^3T_1$ represent the excited states.

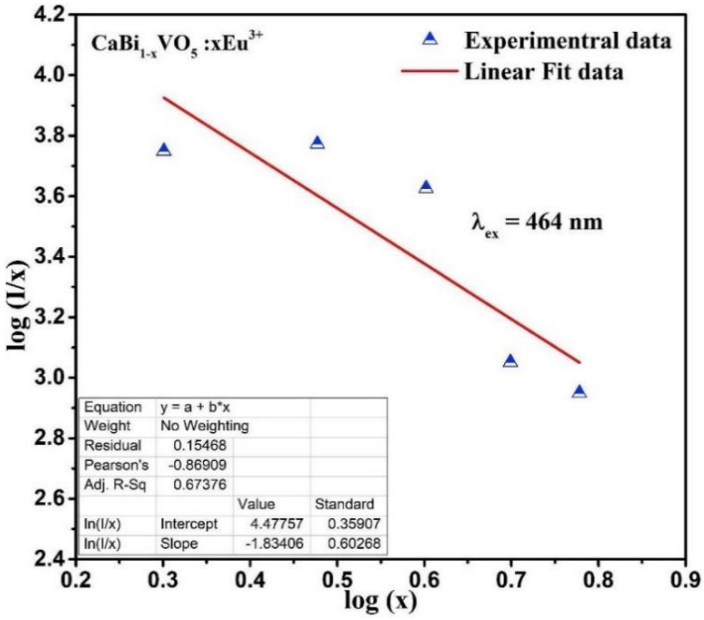

Figure 3.8. *Relationship of log(I/x) and log x for different concentration of Eu^{3+} ions*

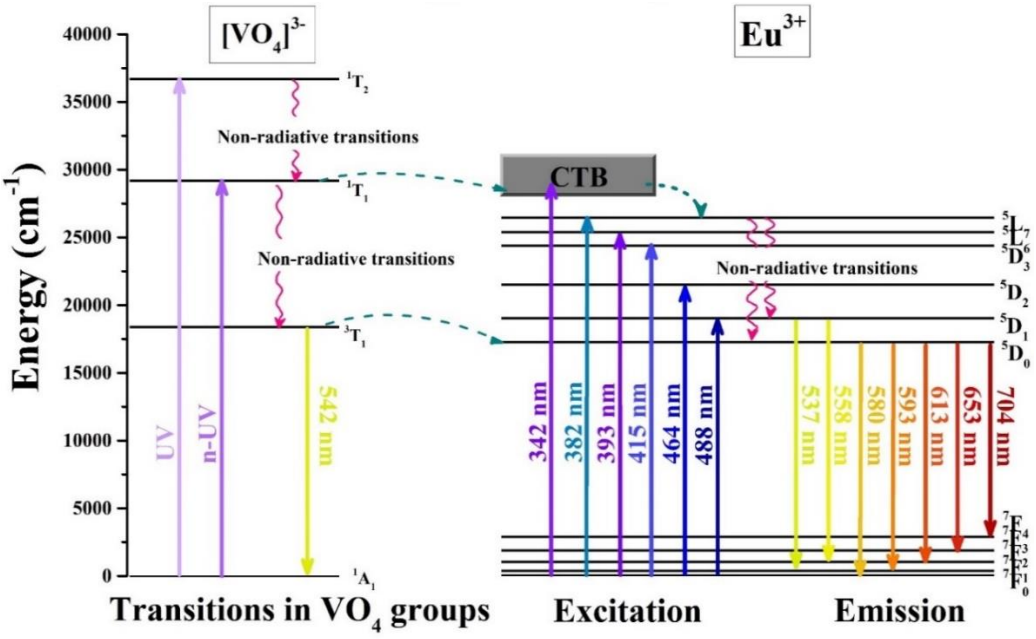

Figure 3.9. *Energy level diagram for Eu^{3+} doped CBV phosphors*

The excitation band of CBV host can be resolved into two broad bands assigned to partly spin allowed $^1A_1 \rightarrow {}^1T_2$ and $^1A_1 \rightarrow {}^1T_1$ transitions [134]. When CBV host is doped with

Eu^{3+} ions, the partial energy transfer may take place either from $^1T_1$ level of VO_4 group to Eu^{3+} CT band or from $^3T_1$ to $^5D_0$ energy level of Eu^{3+} ion. These energy transfers are shown as dashed horizontal arrows. The Eu^{3+} ions may excite by absorbing energy to CTB or various higher excited states such as $^5L_7$, $^5L_6$, $^5D_3$, $^5D_2$ and $^5D_1$ of Eu^{3+} ions as shown in upward arrows in Fig. 3.9. From the excited states ($^1T_2$ and $^1T_1$), the VO_4 groups can relax non-radiatively to $^3T_1$ and then radiatively to ground level ($^1A_1$) finally. Likewise, Eu^{3+} ions may relax non-radiatively from CTB and other excited states to $^5D_0$ or $^5D_1$ levels, followed by de-excitation of Eu^{3+} ions through radiative transitions from $^5D_0$ or $^5D_1$ level to ground state multiplet (^7F_J, where J = 0, 1, 2, 3 and 4) [124]. The non-radiative and radiative transitions are represented as curly and straight downward arrows respectively in Fig. 3.9.

3.3.5. CIE chromaticity coordinates

Using color matching functions $\bar{x}(\lambda)$, $\bar{y}(\lambda)$ and $\bar{z}(\lambda)$ defined by Commission International de I' Eclairage (CIE) 1931, the chromaticity coordinates (x, y) can be calculated from the emission spectral data of the phosphor [135]. The coordinates (x, y) marked on a chromaticity diagram specify the color of the light source. The calculated CIE chromaticity coordinates for Eu^{3+} doped CBV phosphors excited under 342 and 464 nm wavelengths are listed in Table 3.2. The CIE chromaticity coordinates for the $CaBi_{1-x}VO_5$: xEu^{3+}, x=0.0 mol% (un-doped) and x=1.0, 2.0, 3.0, 4.0, 5.0 and 6.0 mol% (doped) samples excited under 342 nm wavelength are shown in Fig. 3.10. As seen from the CIE diagram, chromaticity coordinates shift from yellowish-green (un-doped) to reddish-orange region under 342 nm excitation with increasing Eu^{3+} concentration. Hence, color tunability in Eu^{3+} doped CBV phosphors under 342 nm excitation can be obtained by appropriately adjusting Eu^{3+} ion concentration. The CIE coordinates for all the Eu^{3+} doped CBV phosphors under 464 nm excitation lie in the red region and are in proximity of each other as shown in Fig. 3.10. All the CIE coordinates calculated for emission spectra recorded under 464 nm excitation wavelength are found close to

commercial phosphor Y_2O_2S: Eu^{3+} (x= 0.622 and y= 0.351) and the coordinates designated by National Television Standard Committee (NTSC) (x = 0.670, y = 0.330). The CCT values can be calculated by employing McCamy's polynomial formula given as equation (1.7) [136]. The calculated CCT values are listed in Table. 3.2. for emission

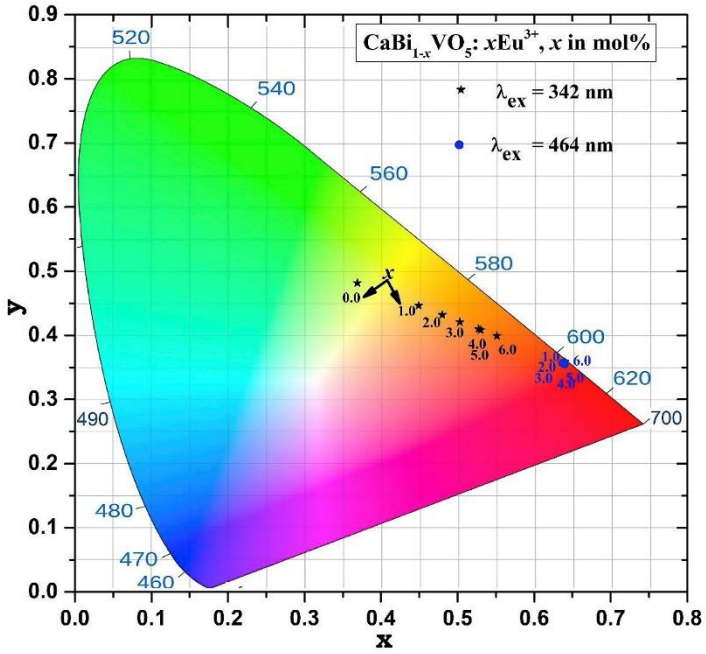

Figure 3.10. *CIE chromaticity coordinates of un-doped (λ_{ex} = 342 nm) and Eu^{3+} doped CBV phosphor (λ_{ex} = 342 and 464 nm)*

spectra recorded at λ_{ex} = 342 and 464 nm for 1.0-6.0 mol% of Eu^{3+} doped CBV phosphor. The purity of the red emission can be calculated by the equation (1.6) [137]. The calculated color purity for the optimized CBV phosphors excited under 464 nm wavelength is 99.36 %. The high value of color purity for the optimized phosphor indicates pure red emission from the proposed CBV: Eu^{3+} phosphors under 464 nm excitation. Thus, optimized phosphor can be used as a potential candidate for red component in w-LEDs under the blue light emitting excitation source.

3.3.6. Decay analysis

The decay profiles of $CaBi_{1-x}VO_5$: xEu^{3+} (1.0 mol% ≤ x ≤ 6.0 mol%) phosphors by monitoring the emission at 613 nm corresponding to $^5D_0 \rightarrow {}^7F_2$ transition excited under 342

and 464 nm wavelengths have been displayed in Fig. 3.11 (a & b), respectively. The decay curves have been fitted with various exponential equations. The decay curve for 1.0 mol% Eu^{3+} doped CBV phosphor shows best fit with single exponential function. However, for Eu^{3+} ion concentrations higher than 1.0 mol%, decay curves deviate from single exponential and the best fit is obtained for bi-exponential function. The decay profiles for the CBV phosphors excited under 464 nm also exhibit similar behavior. The single and bi-exponential functions can be given as equations (1.8 & 1.9) [138].

Table 3.2. *CIE coordinates, CCT and lifetime of CBV samples under different excitations.*

$CaBi_{1-x}VO_5$: xEu^{3+} (x in mol%)	Under 342 nm excitation			Under 464 nm excitation		
	CIE coordinates (x, y)	CCT values (K)	Lifetime (μs)	CIE coordinates (x, y)	CCT values (K)	Lifetime (μs)
0.0	(0.369, 0.481)	4719	-	-	-	-
1.0	(0.449, 0.446)	3123	498	(0.631, 0.366)	2053	469
2.0	(0.480, 0.431)	2603	478	(0.636, 0.361)	2171	449
3.0	(0.527, 0.409)	1989	463	(0.639, 0.358)	2254	438
4.0	(0.551, 0.398)	1799	450	(0.639, 0.358)	2258	422
5.0	(0.503, 0.420)	2268	447	(0.640, 0.358)	2277	391
6.0	(0.530, 0.408)	1960	441	(0.635, 0.362)	2148	384

In general, single exponential fitting indicates no energy transfer between the luminescent centers as they are separated far apart at lower concentration. While, the bi-exponential fitting indicates the probability of energy transfer via interaction between proximal Eu^{3+} ions in the host lattice. The lifetime value for the single exponential fitted plots is provided by τ, while average lifetime of the phosphors showing bi-exponential decay profiles can be

calculated by using equation (1.10) [139].The lifetime (τ_{avg}) values for the $CaBi_{1-x}VO_5$: xEu^{3+} (1.0 mol% ≤ x ≤ 6.0 mol%) excited under 342 and 464 nm wavelengths have been calculated and listed in Table 3.2. The decreasing trend of average lifetime along with increasing concentration of Eu^{3+} ions also indicates energy transfer among Eu^{3+} ions [139].

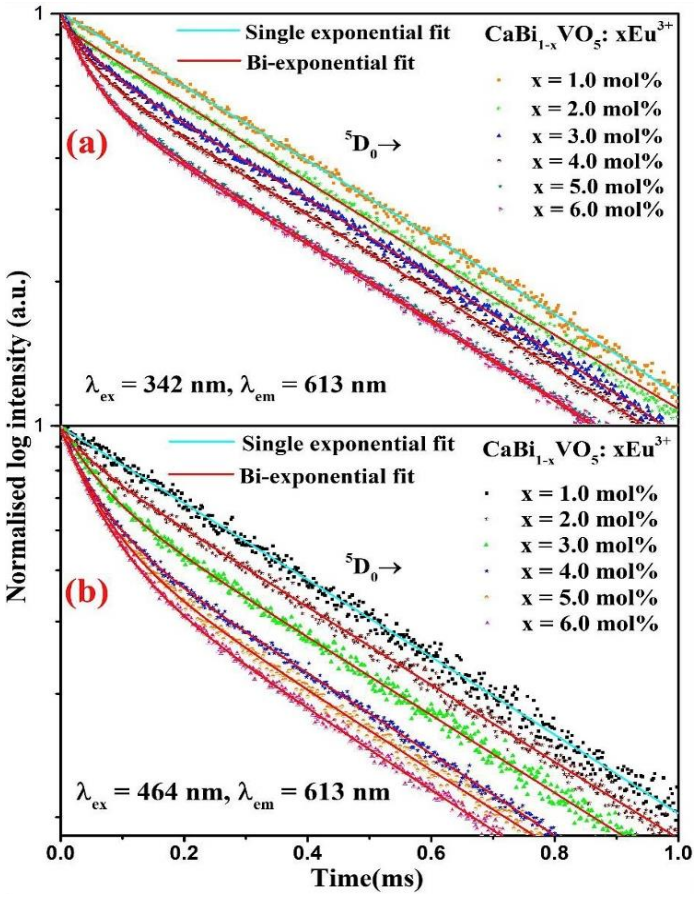

Figure 3.11. *TR-PL decay curves (λ_{em} = 613 nm) of $CaBi_{1-x}VO_5$: xEu^{3+} (1.0-6.0 mol%) under (a) 342 nm and (b) 464 nm excitation*

The calculated lifetimes for as-synthesized phosphors under 342 nm excitation asserts energy transfer from host to Eu^{3+} ions as there is only slight change in the values with varying doping concentration. Average life time value in micro-range suggests that as-synthesized phosphor can be potentially utilized for luminescent device applications.

3.4. Conclusions

Monophasic Eu^{3+} doped $CaBiVO_5$ phosphors have been successfully prepared by solid-state reaction method. The XRD patterns confirm the pure phase formation with an

orthorhombic $CaBiVO_5$ structure with the average crystallite size lies in the 28-45 nm range. The SEM micrographs depict irregular and non-uniform agglomerated morphology of microcrystalline structures. The emission spectrum of the host exhibits a weak broad emission band in the visible region from 400 to 680 nm with an approximate maximum at 542 nm, originating from $[VO_4]^{3-}$ groups under 316 nm excitation. The emission spectra of Eu^{3+} doped CBV phosphor exhibits color tunabilty under 342 nm excitation with varying dopant concentration and intense red emission under blue light excitation. The concentration quenching beyond 4.0 mol% of Eu^{3+} ion concentration is observed due to dipole-dipole interaction between proximal Eu^{3+} ions. Average lifetime values for $^5D_0$ energy level of the Eu^{3+} ions with varying concentrations in CBV phosphors were found to be in the range of microseconds under λ_{ex} = 342 and 464 nm. The CIE chromaticity coordinates calculated for the un-doped CBV sample under the excitation of 342 nm are located in yellowish-green region of CIE 1931 diagram. The CIE chromaticity coordinates (0.640, 0.354) of the most intense Eu^{3+} doped CBV phosphor excited under 464 nm wavelength are found to be close with commercial red phosphor Y_2O_2S: Eu^{3+} (x= 0.622 and y= 0.351) and with the coordinates designated by NTSC. All the above-mentioned results imply that as-synthesized Eu^{3+} activated $CaBiVO_5$ phosphors are potential to use b as a red component in w-LEDs and other luminescent devices.

Chapter 4

Optimization of synthesis procedure and luminescent properties in thermally stable red emitting Sm^{3+} doped $CaBiVO_5$ phosphors for w-LEDs

Sm^{3+} doped $CaBiVO_5$ (CBV: Sm^{3+}) phosphors synthesized namely by solid-state reaction (SSR), combustion (CB) and citrate sol-gel (SG) method to optimize the synthesis procedure and also to enhance the luminescent properties for the first time. X-ray powder diffraction patterns and scanning electron micrographs recorded for the synthesized CBV: Sm^{3+} phosphors to analyse structural and morphological aspects, respectively. The excitation spectra measured by monitoring emission at 649 nm for CBV: Sm^{3+} phosphors reveal significant absorption in ultraviolet (UV), near (n)-UV and blue spectral regions. The comparative photoluminescence spectra measured under 343 nm excitation for differently synthesized CBV: Sm^{3+} phosphors, which exhibit significantly enhanced emission intensity for SG derived phosphor than other adopted methods. Unlike mostly explored Sm^{3+} doped phosphors, emission peak in red spectral region (649 nm) is more intense as compared to the emission peak in orange region (599 nm) in the present work. The energy transfer mechanism responsible for concentration quenching in CBV phosphors is discussed in detail. The CBV: Sm^{3+} phosphors manifest color tunability from orange to orange-red region by modulating excitation from 275 nm (0.567, 0.404) to 343 nm (0.591, 0.399) and finally to 406 nm (0.620, 0.376). The temperature-dependent PL studies indicate appreciable thermal stability of the as-prepared phosphor. Above mentioned results suggest that CBV: Sm^{3+} phosphor has great potential for use in white light-emitting diode (w-LED) applications.

4.1. Introduction

Recent advancements in lighting technologies have endowed sophisticated w-LEDs employing yellow phosphor (YAG: Ce^{3+}) coating on InGaN blue chip at commercial level. However, such w-LEDs exhibit undesirably elevated correlated color temperature (CCT) and poor color rendering index (CRI) due to the scarcity of the red component [140-143]. The possible solutions may be fabricating either trichromatic w-LEDs composed of UV/n-UV chips coated with red (R), green (G) and blue (B) emitting phosphors or dichromatic w-LEDs coated with cyan (C) and orange (O) emitting phosphors [115, 138]. The development of such w-LEDs necessitates the preparation of an eco-benign, chemically and thermally stable red or orange emitting phosphor with efficient absorption in UV and n-UV spectral region. For selecting best option as red/orange component for w-LED application, the captivating properties of Eu^{3+} doped $CaBiVO_5$ (CBV) phosphors presented in previous chapter have impelled the investigation of Sm^{3+} ions doped CBV phosphor. Because when Sm^{3+} ions are doped in an effective host lattice, they are capable of providing emission in the red/orange spectral region under UV, n-UV and blue light excitation due to their characteristic f-f transitions.

Moreover, to enhance the luminescent properties of RE ion doped CBV phosphor, the CBV phosphors are synthesized via SSR, CB and SG synthesis routes. The optimization of synthesis route can cause reduction in size and shape uniformity leading to appreciable enhancement in luminescent properties due to uniform mixing of the precursors [80, 143, 145]. For instance, the purity and morphology of the sample in sol-gel method can be pre-eminently improved by controlling the pH value, inclusion of complexing agents and surfactants, which further improves the photoluminescence (PL) properties of as-synthesized phosphors [146, 147].

The present report elucidates the comparison of structural, morphological and luminescence properties of CBV: Sm^{3+} phosphors, which have been optimised by varying synthesis routes (SSR, CB and SG). Moreover, a detailed discussion has been provided for understanding the energy transfer mechanisms. Further, the possibility to utilize intense red emitting CBV: Sm^{3+} phosphor synthesized via optimized route for w-LEDs and other various luminescent devices has been explored.

4.2. Sample preparation

The CBV phosphors doped with Sm^{3+} ions were synthesized by SSR, CB and SG method as described in section 2.2.1, 2.2.2 and 2.2.3 of chapter 2. The protocol details of SSR, combustion and sol-gel synthesis methods are represented in Fig. 2.1 & 2.2 of chapter 2. The samples prepared using different methods are coded as mentioned in Table 4.1.

Table 4.1. *Sample codes for differently synthesized CBV: Sm^{3+} phosphors at various concentrations*

Sample code	**Sm^{3+} concentration in CBV host (mol%)**	**Synthesis method**
SGS0	0.0	Citrate sol-gel
SGS1	1.0	Citrate sol-gel
SGS2	2.0	Citrate sol-gel
SGS3	3.0	Citrate sol-gel
SGS4	4.0	Citrate sol-gel
SGS5	5.0	Citrate sol-gel
SRS1	1.0	Solid-state reaction
CBS1	1.0	Combustion

4.3. Results and discussion

4.3.1. Thermogravimetric analysis (TGA)

The TGA and derivative thermogravimetric (DTG) curves shown in Fig. 4.1 were used to determine the calcination temperature of powder precursor in the SG method to form pure $CaBiVO_5$ phase. In the TG curve (Fig. 4.1), a large amount of weight loss (41.30%) through two distinct stages was observed while heating the dried gel within the temperature range of 40–800 °C. The first stage (40–147 °C) showing a weight loss of 13.42% accompanied by an endothermic peak in DTG curve at 75 °C can be attributed to evaporation of water and ethanol used in material synthesis. The second stage (147–725 °C) with a weight loss of 27.88% accompanied by two endothermic peaks at 307 and 546 °C in DTG curve represent exhaustion and decomposition of organic species like citric acid, PEG and nitrate precursors [148]. Finally, no weight loss observed after 725 °C would mark the phase forming initiation of $CaBiVO_5$.

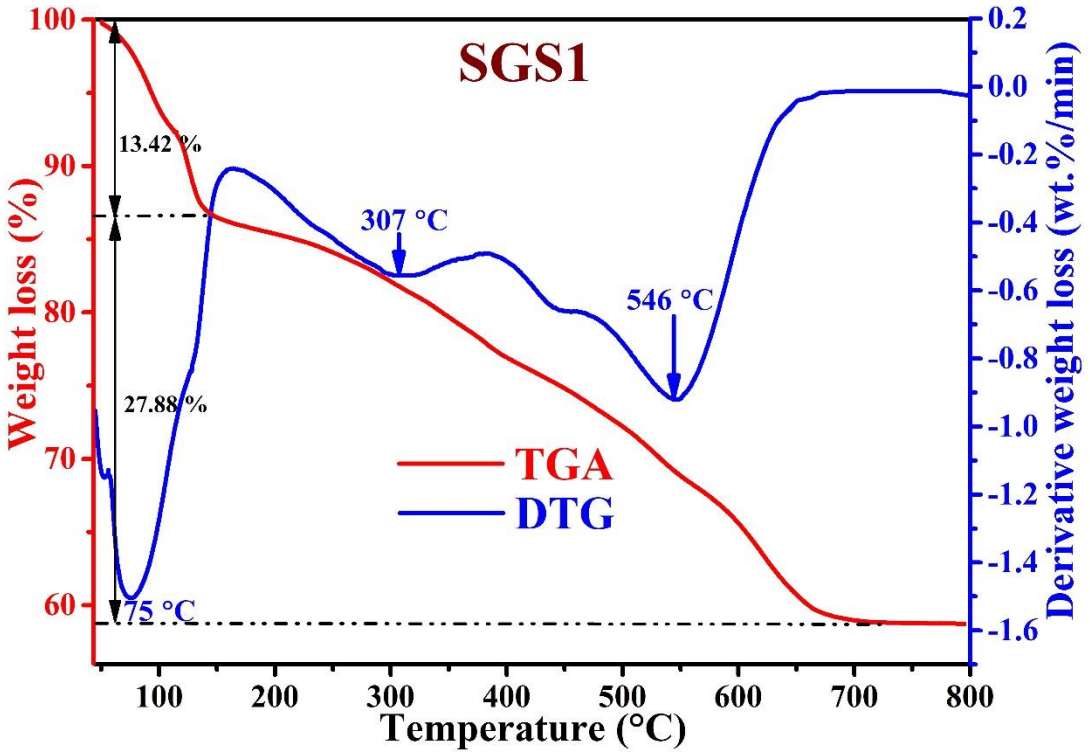

Figure 4.1. *TGA and DTG curves for SGS1 phosphor*

4.3.2. XRD analysis

Fig. 4.2(a) represents the XRD patterns of 1 mol% Sm^{3+} doped CBV (CBV: 1 mol% Sm^{3+}) phosphors prepared through SSR, CB and SG synthesis routes compared with standard JCPDS (card no: 81–1775) pattern of $CaBiVO_5$ crystal structure. Fig. 4.2(b) shows the XRD patterns for SGS2, SGS3, SGS4 and SGS5 with increasing the dopant concentration (Sm^{3+}).

All the XRD peaks in diversely synthesized CBV:1.0 mol% Sm^{3+} can be indexed to the standard JCPDS patterns, indicating pure phase formation of Sm^{3+} doped CBV phosphors via each synthesis route. The absence of any impurity peaks in XRD pattern symbolizes the successful incorporation of Sm^{3+} ions (0.958 Å) in host lattice and replaced by Bi^{3+} ions (0.960 Å) due to similar radii and same valence state. The Rietveld refinement using FullProf suite has been performed on the XRD data for differently synthesized CBV: 1.0 mol% Sm^{3+} phosphors to further assess the phase purity and shown as Fig. 4.2(c), (d) & (e), respectively. The pseudo-Voigt function is employed to simulate the peak shape in the software. The values of lattice parameters (a, b, c, α, β and γ), Wycoff's positions of the atoms and space group referring to the standard data are fed in the software [114]. The refinement results for XRD patterns of CBV: 1.0 mol% Sm^{3+} phosphor synthesized via three different routes are enumerated in Table 4.2. The refinements results do not reveal any significant deviation from the standard data and magnitude of goodness of fit (χ^2) is close to 1, indicating successful single-phase formation of CBV: Sm^{3+} phosphor via all three synthesis routes. The crystal structure of $CaBiVO_5$ synthesized by SG route is modelled with Vesta software using the refined XRD data and shown in Fig. 4.2(f). The crystal structure with orthorhombic symmetry under Pbca space group indicates the expected tetrahedral coordination V^{5+} with oxygen atoms and they are arranged isolated to each other. The CaO_7 polyhedra can be described as a deformed trigonal prism with a rectangular area, which is edge linked and forming layers.

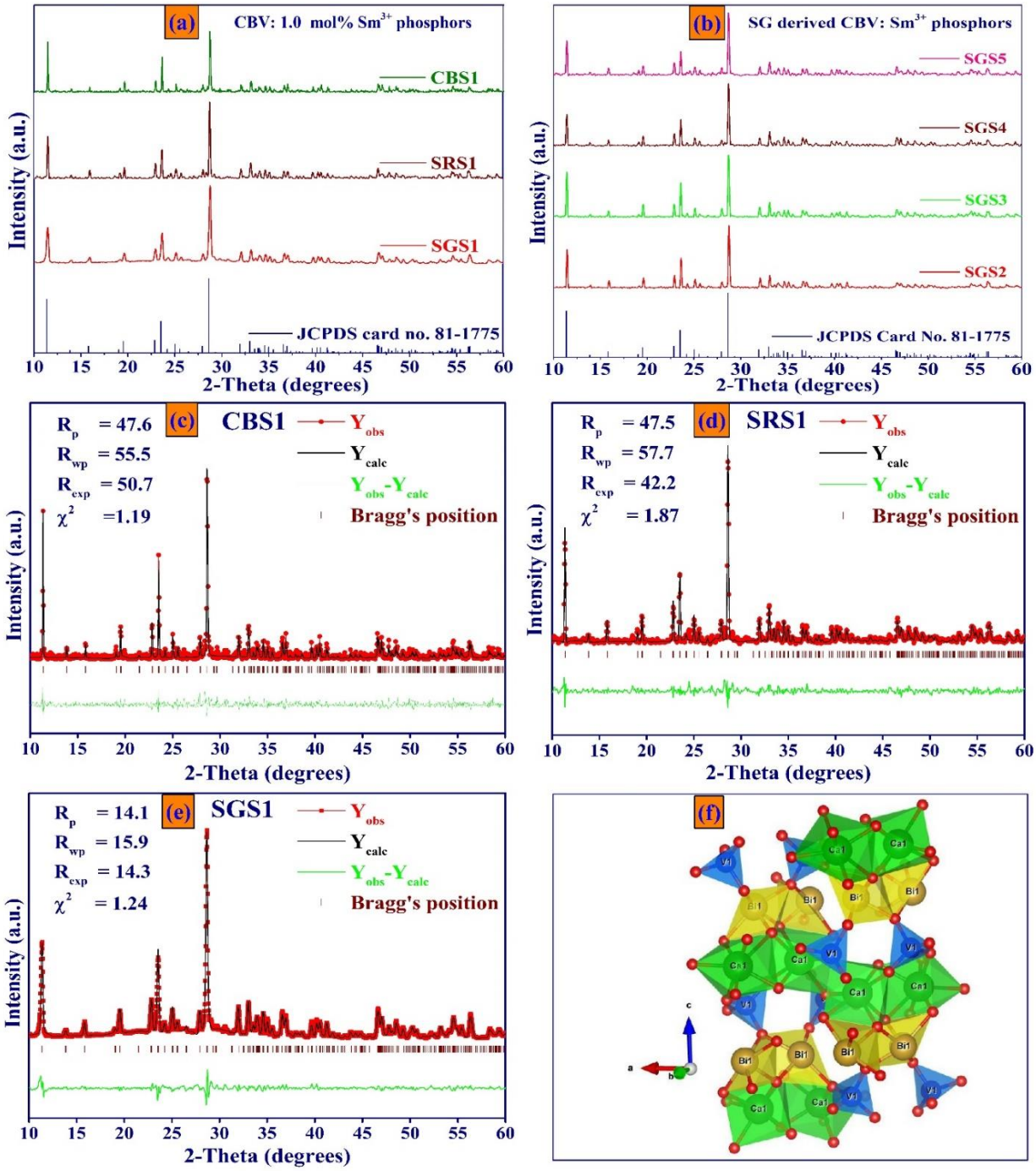

Figure 4.2. *XRD patterns for (a) CBV: 1.0 mol% Sm^{3+} phosphors prepared via SSR, CB and SG methods (i.e. CBS1, SRS1 and SGS1), (b) SGS2, SGS3, SGS4 and SGS5 compared with standard JCPDS data, (c) Rietveld refinement for CBS1, (d) SRS1 and (e) SGS1 phosphors and (f) Crystal structure for SGS1 phosphor*

The 3-D structure of the $CaBiVO_5$ is only possible by the Bi^{3+} ions, which are asymmetrically surrounded by oxygen and form one-sided tetragonal pyramidal linked by edges [114].

Table 4.2. *Rietveld refinement results for differently synthesized 1.0 mol% Sm^{3+} doped CBV phosphor*

Parameters	**SRS1**	**CBS1**	**SGS1**
Structure	Orthorhombic	Orthorhombic	Orthorhombic
Space group	D_{2h}^{15} −Pbca	D_{2h}^{15} −Pbca	D_{2h}^{15} −Pbca
a (Å)	11.0948	11.1970	11.1977
b (Å)	5.3231	5.4267	5.4248
c (Å)	15.4732	15.5712	15.5665
α=β=γ	90°	90°	90°
R_p (%)	47.5	47.6	14.1
R_{wp} (%)	57.7	55.5	15.9
χ^2	1.87	1.19	1.24
V ($Å^3$)	929.143	946.164	945.604
Density (mg/m^3)	4.791	4.562	4.336

Further, the crystallite size (D) can be calculated for differently synthesized CBV: 1.0 mol% Sm^{3+} using the Debye Scherrer's formula mentioned earlier as equation (2.2) of chapter 2. The crystallite sizes evaluated for SRS1, CBS1, SGS1, SGS2, SGS3, SGS4 and SGS5 are 52.69, 47.49, 34.02, 32.47, 30.16, 29.07 and 27.81 nm, respectively. The smaller crystallite size obtained in case of CBV phosphor synthesized by SG route can be attributed due to the inclusion of PEG stimulating the growth process at lower sintering temperature [149]. Moreover, the crystallite size evaluated for SG derived Sm^{3+} doped CBV phosphors decreases with increase in dopant concentration as lattice contraction may occur due to replacement of larger size Bi^{3+} with smaller size Sm^{3+} ions in the crystal lattice [150].

4.3.3. SEM analysis

The SEM micrographs of differently synthesized Sm^{3+} doped CBV phosphors are shown in Fig. 4.3(a–d). The SEM micrograph (Fig. 4.3(a)) of SRS1 shows irregular morphology and grain size is in the range of micrometre (μm). The SEM image of CBS1 (Fig. 4.3(b)) exhibit the porous structured non-uniform particles due to voluminous gas evolution during the combustion process. The phosphors synthesized via SG method showing improved morphologies (Fig. 4.3(c & d)) as the edges are soft and most of the particles are spherically shaped with radii in μm range. SEM images for SGS1 are showing comparably less agglomeration and smaller sized particle that may be due to formation of CBV phosphor at relatively lower temperature. Moreover, citrate and PEG network formation in the SG method helped to improve uniformity in morphology of the SGS1 phosphors. Thus, phosphors synthesized by SG method can be more uniformly coated on UV/n-UV LED chip and consequently may enhance emission intensity.

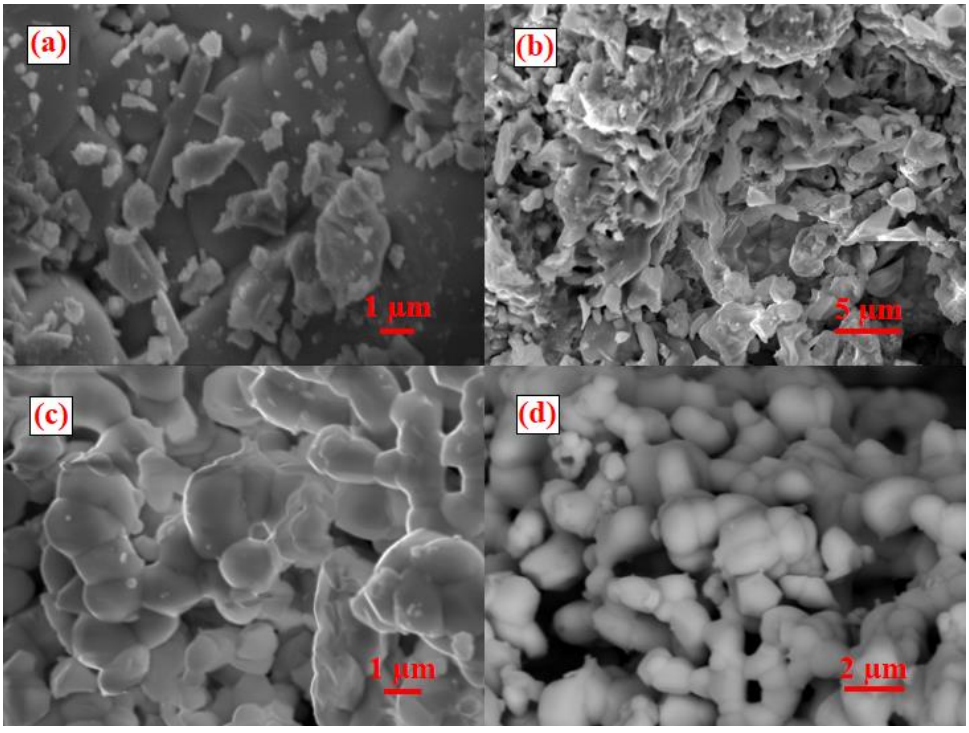

Figure 4.3. *SEM micrographs of CBV: 1.0 mol% Sm^{3+} phosphor synthesized via (a) SSR method, (b) CB method and (c & d) SG method at different resolutions*

4.3.4. Diffuse reflectance spectrum analysis

Fig. 4.4(a) shows the DR spectra of SG derived un-doped and 1.0 mol% Sm^{3+} doped CBV sample in 250-750 nm wavelength range. The DR spectra of un-doped CBV host and Sm^{3+} doped CBV phosphors were found to be in accordance with the excitation spectra. The un-doped (SGS0) sample exhibit significant absorption at 316 nm wavelength is corresponding to the transitions of VO_4 groups. The DR spectrum of SGS1 phosphor shows intense absorption at 343 nm along with few sharp peaks at 406, 466 nm wavelength due to 4f-4f transitions Sm^{3+} ions as explained in the subsequent sections [120, 151]. Also, the optical band gap (E_g) can be estimated from the DR spectra of as-synthesized samples using the Kulbeka Munk's relations as mentioned in section 2.3.5. From the graph between $[F(R)h\nu]^2$ and $h\nu$ plotted using n = ½, the reckoned value of E_g to be 3.04 and 3.17 eV, respectively. Clearly, inclusion of Sm^{3+} ions may cause broadening of the band gap [152].

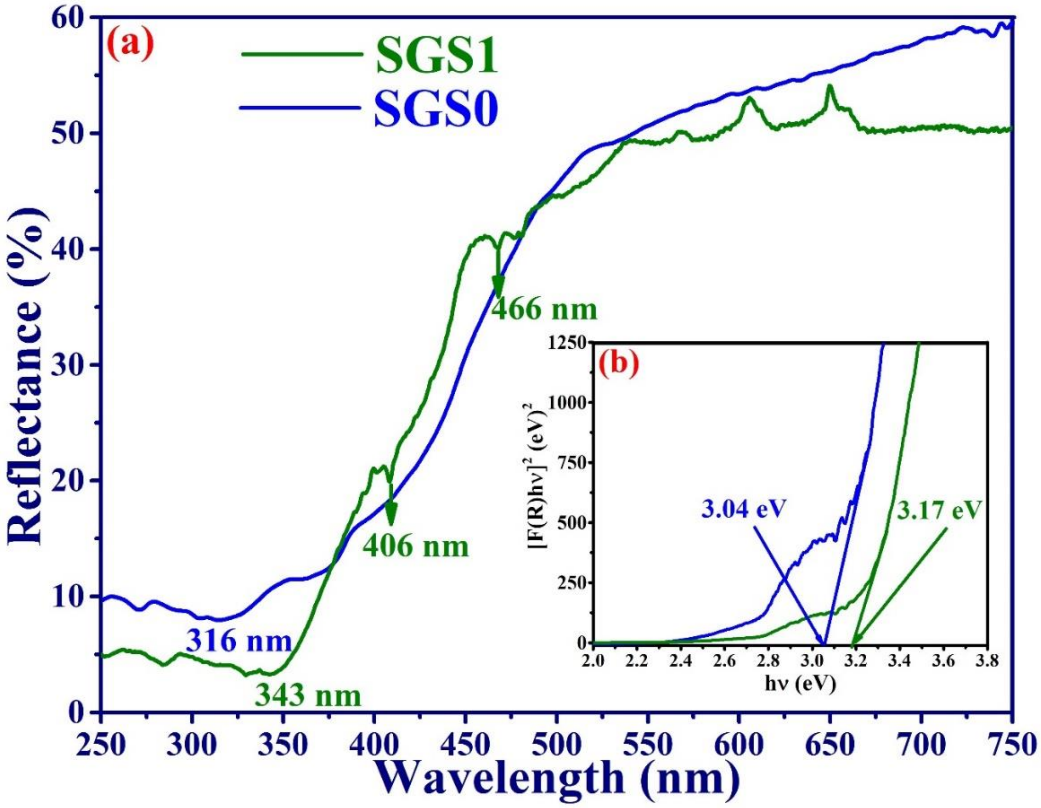

Figure 4.4. *Diffuse reflectance spectra for SGS0 and SGS1 phosphors*

4.3.5. Photoluminescence (PL) analysis

Fig. 4.5(a) shows the excitation spectra of differently synthesized 1.0 mol% Sm^{3+} doped CBV phosphors monitored at 649 nm wavelength. All the excitation spectra composed of an intense broad excitation peak in the range of 200-385 nm and several sharp peaks in the range of 385-500 nm. The broad intense band in the range 200-385 nm wavelength can be clearly understood by deconvoluted graph for SGS1. The deconvoluted graph consists of three intense peaks centred about 275, 316 and 343 nm wavelengths. The short wavelength excitation peaks around 275 and 316 nm are similar to the peaks as shown in excitation spectrum for CBV host (Fig. 3.4(a)) and hence attributed to the transitions of VO_4 group as mentioned in chapter 3. The long wavelength excitation centred about 343 nm can be endorsed to $^6H_{5/2} \rightarrow {}^4D_{7/2}$ transition of Sm^{3+} ions [155]. Further, the peaks located at 391, 406, 418, 441, 466, 477 and 489 nm are due to transitions from $^6H_{5/2}$ to $^4L_{15/2}$, $^4F_{7/2}$, $^4M_{19/2}$, $^4G_{9/2}$, $^4I_{13/2}$, $^4M_{15/2}$ and $^4I_{9/2}$ levels, respectively of Sm^{3+} ions doped CBV lattice [156]. To optimize the synthesis technique, the emission spectra for SGS1, SRS1 and CBS1 have been measured at most intense 343 nm excitation wavelength as shown in Fig. 4.5(b). The emission spectra of all the phosphors resemble in terms of spectral peak positions except variation in the intensities. The emission peaks centred at 566, 606, 649 and 711 nm are attributed to transitions from $^4G_{5/2}$ to ^6H_J (J = 5/2, 7/2, 9/2 and 11/2) levels, respectively [157]. The emission graphs conspicuously indicate that SG derived Sm^{3+} doped CBV phosphors exhibit appreciable enhancement in the PL intensity in comparison with the phosphors synthesized by other methods. By evaluating the integrating intensities, it can be said that the PL intensity of SGS1 is relatively 10.8 times and 2.6 times more than CBS1 and SRS1, respectively. Also, the emission spectrum for Sm^{3+} doped CBV phosphor synthesized by SG method shows broadening of the peaks. The enhanced intensity and broadening of the peaks can be attributed due to the improved morphology and reduction in size, which is also evident in SEM micrographs of SGS1 phosphors. This may be

explained as the introduction of citric acid in SG method supports the grain growth at lower temperature and homogenous mixing leading to the improved morphology. Thus, prepared in smaller size, less agglomerated and homogenous particles leads to less scattering and hence enhanced luminescent properties [85, 158].

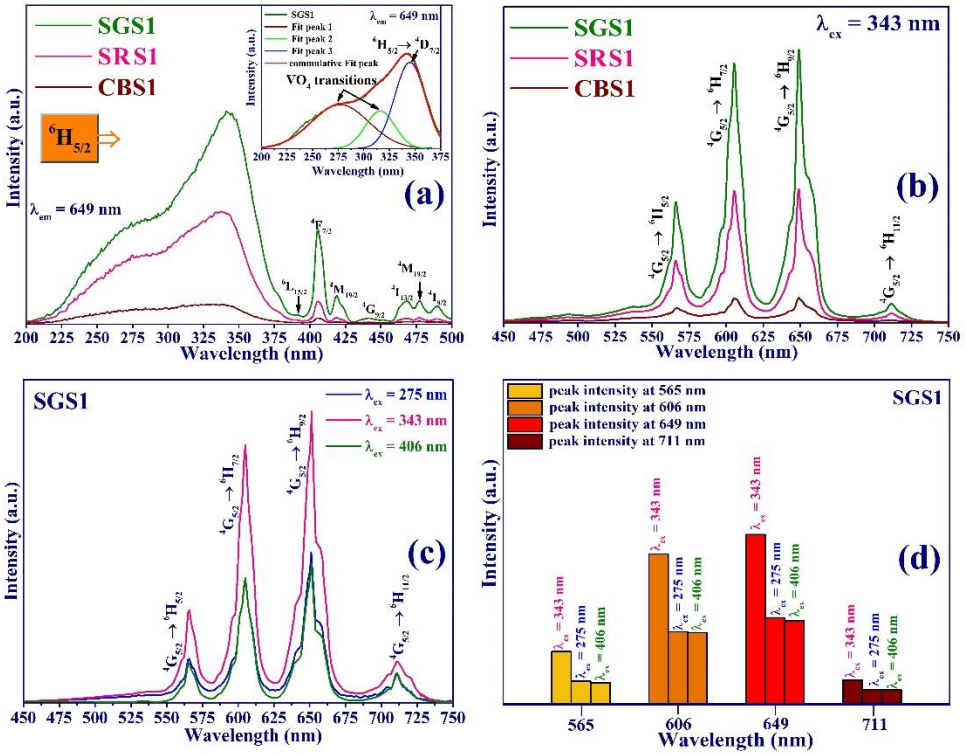

Figure 4.5. *(a) Excitation spectra for SGS1, SRS1 and CBS1 (λ_{em} = 649 nm), Emission spectra of (b) SGS1, SRS1 and CBS1 (λ_{ex} = 343 nm), (c) SGS1 under different excitations and (d) Emission intensity comparison for SGS1 under different excitations*

Further, large surface defects formed due to voluminous and rapid gas evolution in case of combustion method may be the reason for its low emission intensity [159]. Hence, SG method is the optimized route for synthesizing the CBV phosphors for its multifunctional applications. Fig. 4.5(c) shows the comparison of emission intensity of SGS1 phosphors under 275, 343 and 406 nm wavelengths. The emission intensity at 649 nm wavelength for SGS1 under 343 nm excitation is most intense. The emission spectrum under 275 nm excitation exhibits weak broadband ranging from 400 to 680 nm similar to host emission band (as discussed in section 3.3.4. of chapter 3) overlapped with sharp emission peaks due to 4f-4f

transitions of Sm^{3+} ions. The presence of emission peaks corresponding to Sm^{3+} ions under host excitation confirms the energy transfer from host to Sm^{3+} ions. Further, relative emission intensity drawn as a bar graph under different excitations (Fig. 4.5(d)), it is found that the emission intensity corresponding to Sm^{3+} ion transitions is more intense under 343 nm excitation. It may be due to the partial overlap of host excitation band with strong excitation peak ($^6H_{5/2} \rightarrow {}^4D_{7/2}$) of Sm^{3+} ions present at 343 nm wavelength. The emission spectrum (Fig. 4.5(c)) under 406 nm excitation exhibits only emission peaks corresponding to Sm^{3+} ion without any host emission band. Therefore, further the CBV: Sm^{3+} are excited under 406 nm wavelength for further luminescence and thermal stability analysis.

Moreover, $^4G_{5/2} \rightarrow {}^6H_{5/2}$ transition assigned to an emission peak at 566 nm is a magnetic dipole (MD) transition and is independent of crystal field environment. The emission peak at 649 nm attributed to $^4G_{5/2} \rightarrow {}^6H_{9/2}$ transition is an electric dipole (ED) transition thus hypersensitive to crystal field environment. In addition to that, the emission peak corresponding to $^4G_{5/2} \rightarrow {}^6H_{7/2}$ transition at 606 nm is a mixed MD and forced ED transition [160]. Further, the peak centred at 649 nm is found to be most intense in the present study which is less observed in various Sm-doped matrices. A. Hermann et al. [161] have reported that this effect could be ascribed to a change in the local environment symmetry at the Sm^{3+}-occupied sites, which may be the source for emission intensity peak at 649 nm ($^4G_{5/2} \rightarrow {}^6H_{9/2}$) in the host matrix with higher local asymmetry and no inversion symmetry. The asymmetry ratio which is defined as the ratio between integrated intensity of ED to MD transition, which can be employed to estimate local site symmetry. Greater the asymmetry ratio, more would be the distortion from inversion symmetry. In the present case, the reckoned value of asymmetry ratio is 4.15 under 343 nm excitation for SGS1. The high value of asymmetry ratio indicating the occupancy of Sm^{3+} ions at asymmetry sites without inversion centre in the CBV host, which also explains the highest emission intensity at 649 nm in CBV: Sm^{3+} phosphors [158, 161].

Fig. 4.6(a) shows the emission spectra for $Ca_{1-x}BiVO_5$: xSm^{3+} (1.0 mol% ≤ x ≤ 5.0 mol%) phosphor under 406 nm excitation. From the graph, it can be seen that all Sm^{3+} doped CBV phosphors exhibit emission peaks corresponding only to 4f-4f transitions of Sm^{3+} ion with variation in emission intensity. The emission intensity firstly increases up to 2.0 mol% Sm^{3+} ion concentration and then decrease beyond it due to concentration quenching (Fig. 4.6(b)). It may be explained as at higher doping concentration, the neighbouring Sm^{3+}-Sm^{3+} ions become so close that instead of radiative emission, the non-radiative energy transfer amongst themselves become dominant [6]. The non-radiative energy transfer mainly dependent on the critical distance (R_c) between neighbouring Sm^{3+} ions at X_C = 0.02 mol. The evaluated value (22.43 Å) of R_c exceeding far from the critical distance limit (maximum 5 Å) according to the theory given by Van Uitert [131] for energy transfer through exchange interaction. Hence, the non-radiative energy transfer occurs in the present case via multipolar interaction as explained in Dexter's theory. As per the Dexter theory [132], the slope of the linear fitted graph between log (I/x) and log x gives the value of Q, which indicates the type of multipolar interaction. The graph (log (I/x) vs. log x) shown in Fig. 4.6(c) is based on the emission spectra of $CaBi_{1-x}VO_5$: xSm^{3+} excited under 406 nm excitation wavelength and provides the slope value as -1.69. The calculated value of Q is 5.09, which is close to 6, confirms the multipolar interaction to be electric dipole-dipole in nature.

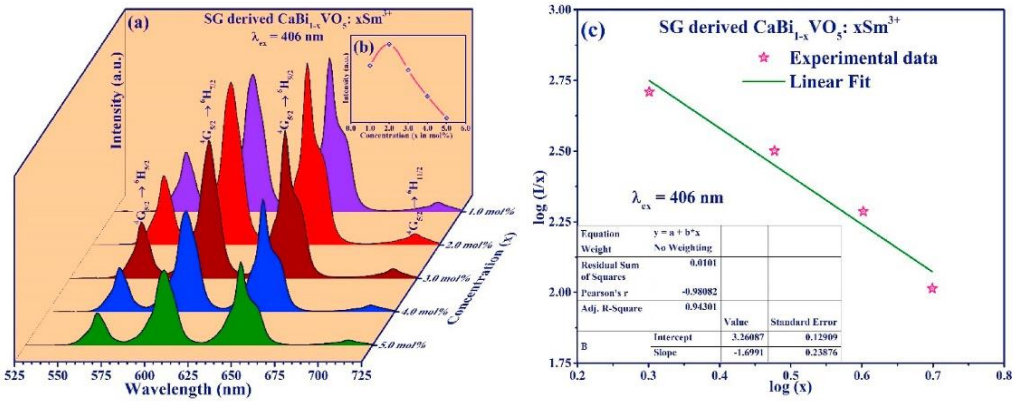

Figure 4.6. *(a) Emission spectra for SG derived CBV: Sm^{3+} phosphors (λ_{ex} = 406 nm), (b) Inset: Variation of emission intensity at 649 nm with Sm^{3+} ion concentration (λ_{ex} = 406 nm) and (c) Dexter plot for SG derived CBV: Sm^{3+} phosphors at λ_{ex} = 406 nm*

The excitation, emission and energy transfer processes can be depicted by partial energy level (EL) diagram as shown in Fig. 4.7 for Sm^{3+} ions doped in CBV host. Under 275 nm excitation (upwards arrows), the $^1T_2$ state of VO_4 groups non-radiatively relaxed (shown as curly arrows) to $^3T_1$ state and then transfers its energy (curved arrow) to $^4G_{5/2}$ level of Sm^{3+} ions. Since $^4G_{5/2}$ level of Sm^{3+} is far above from the consecutive lower energy states, so only radiative transitions (downward arrows) can occur to lower energy level of Sm^{3+} ions providing emission in orange to red spectral region. Further, by absorbing the incident radiation, the Sm^{3+} ions at ground state can be excited to higher states. While relaxing, the energy is released non-radiatively (curly arrows) to $^4G_{5/2}$, and then radiatively (downward arrows) to $^6H_{5/2}$, $^6H_{7/2}$, $^6H_{9/2}$, and $^6H_{11/2}$ energy states. The non-radiative energy transfer can also occur via possible cross-relaxation channels (CRC) and resonance energy transfer (RET) mechanisms, as shown in Fig. 4.7. The possible CRC channels are $(^4G_{5/2} + {}^6H_{5/2}) \rightarrow (^6F_{11/2} + {}^6F_{5/2})$, $(^4G_{5/2} + {}^6H_{5/2}) \rightarrow (^6F_{5/2} + {}^6F_{11/2})$, $(^4G_{5/2} + {}^6H_{5/2}) \rightarrow (^6F_{9/2} + {}^6F_{7/2})$ and $(^4G_{5/2} + {}^6H_{5/2}) \rightarrow (^6F_{7/2} + {}^6F_{9/2})$ [162].

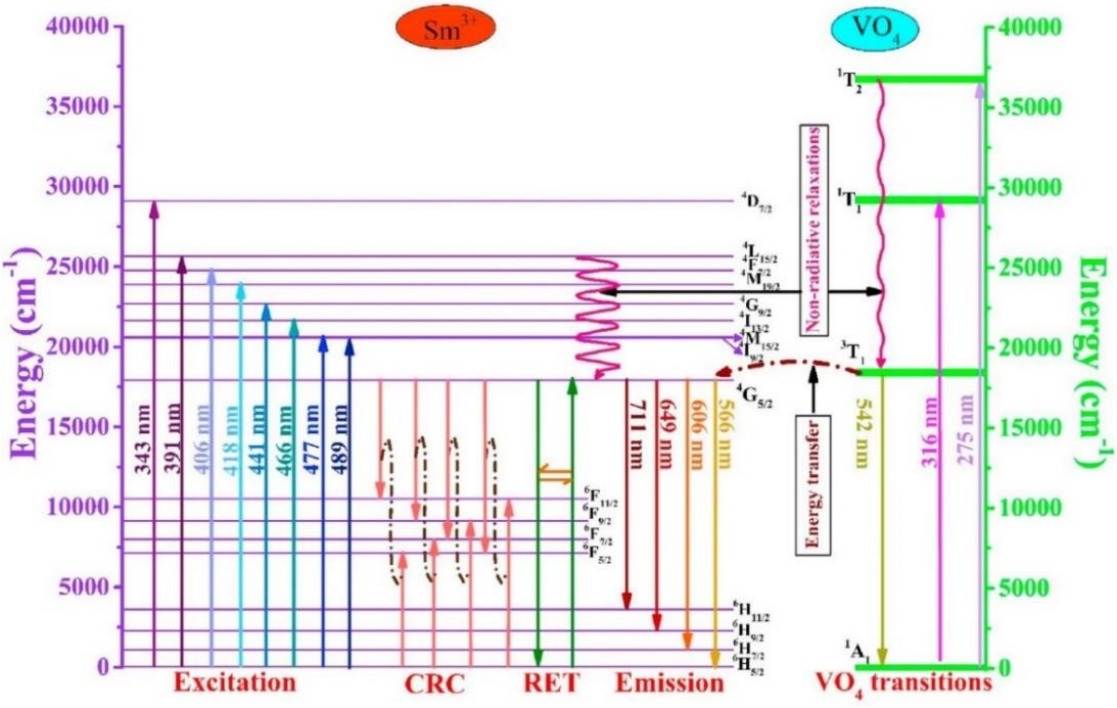

Figure 4.7. *Energy level diagram for Sm^{3+} ions doped in CBV phosphor*

4.3.6. CIE chromaticity coordinates

The CIE chromaticity coordinates and CIE diagram are significant to actualize the exact emission colour of as-synthesized phosphor. Therefore, the CIE coordinates (Fig. 4.8) for the optimised (SGS2) phosphor using emission spectra recorded under 275, 343 and 406 nm excitations, which are found to be (0.567, 0.404), (0.591, 0.399) and (0.620, 0.376), respectively. The CIE diagram displays wavelength dependent color tunability since CIE coordinates shifts from orange to orangish-red region by tuning the excitation wavelength from 275 to 343 and finally to 406 nm. The CIE coordinates for 275 and 343 nm excitation wavelengths are found close to the Nichia corporation fabricated amber LED NSPAR 70BS (0.570, 0.420). The CCT values found to be 1732, 1720 and 1873 K for optimised phosphor (SGS2) under 275, 343 and 406 nm excitations, respectively. In view of the above, the Sm^{3+} doped CBV phosphor is a favourable choice for orange or red emitting component in UV/n-UV pumped warm w-LEDs with required low CCT.

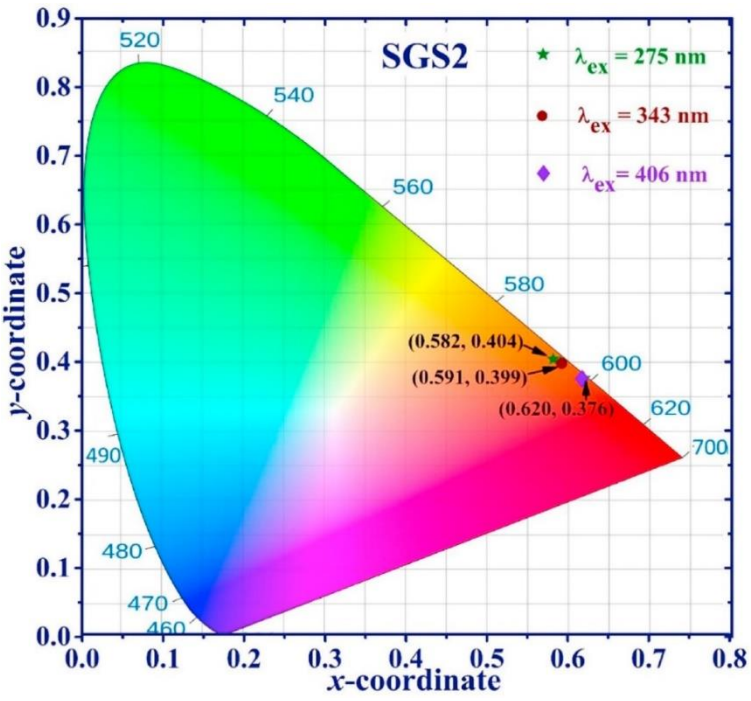

Figure 4.8. *CIE diagram for SGS2 phosphor at λ_{ex} = 275, 343 and 406 nm excitations*

4.3.7. PL Decay analysis

Fig. 4.9(a) represents the PL decay curve for SG derived $CaBi_{1-x}VO_5$: xSm^{3+} (x = 1.0, 2.0 and 5.0 mol%) phosphors recorded at 649 nm ($^4G_{5/2} \rightarrow {}^6H_{9/2}$) wavelength under 343 nm excitation. The decay curves have been tried to fit with various exponential equations. Eventually, it is found to be well-fitted with bi-exponentially as fitted decay curves are shown in Fig. 4.9(a). The average lifetime value (τ_{avg}) of the bi-exponentially fitted decay curves for 1.0, 2.0 and 5.0 mol% Sm^{3+} doped CBV phosphors delivers the average lifetime to be 810.8, 773.4 and 679.0 μs, respectively. The lifetime values decrease with increase in Sm^{3+} ion concentration, indicating the energy transfer between the neighbouring Sm^{3+}-Sm^{3+} ions leading to concentration quenching [158].

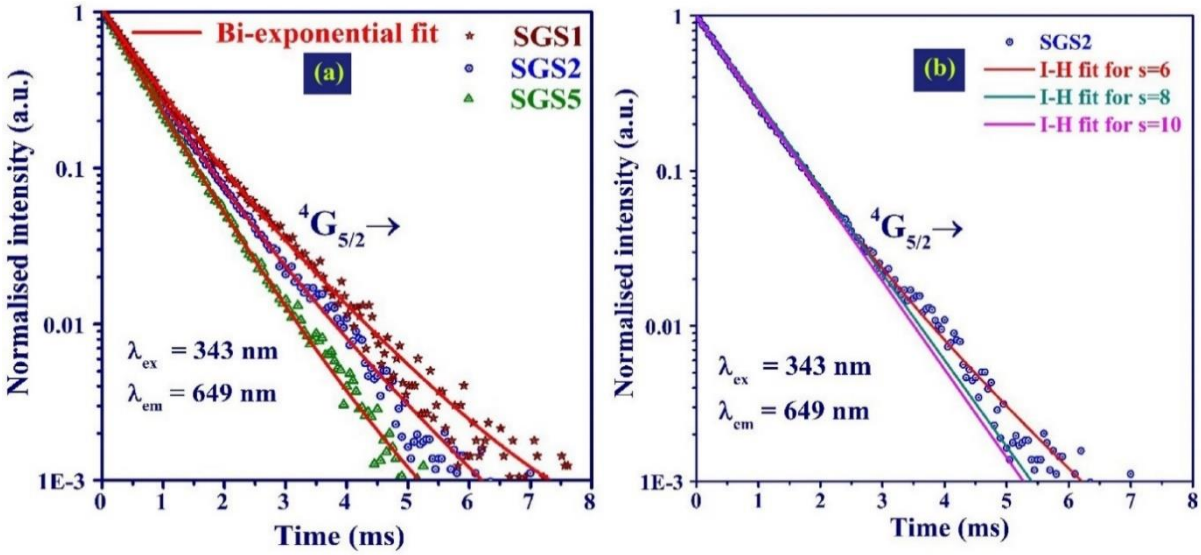

Figure 4.9. *(a) PL decay curves for SGS1, SGS2 and SGS5 phosphors at λ_{ex} = 343 nm and (b) I–H fit for optimised (SGS2) phosphor*

The energy transfer mechanism between Sm^{3+} ions can be well understood by using Inokutti Hirayama (I-H) model. As per the I-H model, energy transfers via multipolar interaction between Sm^{3+} ions is leading to non-exponential nature of decay curves and decay intensity and time can be related as given in equation (1.18) [158]. The value t_o actually is the lifetime of donor without any acceptor (but here, t_o is taken for SGS1), s = 6, 8 and 10 values represents d-d, d-q and q-q type of multipolar interaction and Q is the energy transfer

parameter. The decay curve for optimised (2.0 mol%) Sm^{3+} doped CBV phosphor is well fitted with equation (1.18) for s = 6 as shown in Fig. 4.9(b), which specifies that the energy transfer is due to d-d interaction amongst Sm^{3+} ions and also supporting the results projected by Dexter's theory.

4.3.8. Temperature-dependent PL analysis

To investigate the feasibility of as-synthesized phosphor for w-LEDs applications, temperature-dependent PL of 2.0 mol% Sm^{3+} doped CBV phosphor is studied in the range 323-443 K under 406 nm excitation and shown in Fig. 4.10(a). The CBV: Sm^{3+} phosphors are excited under 406 nm wavelength (red emission) for thermal stability analysis. As seen from Fig. 4.10(a), with an increase in temperature, the spectral profile (emission peak position and FWHM) remains the same except the emission intensity. The emission intensity declines with increase in temperature due to thermal quenching phenomenon. This phenomenon is endorsed to temperature dependent non-radiative relaxations. The rate of non-radiative emission probability (R_{nr})can be written as equation (1.11) [163]. In the formula, ΔE_a denotes the activation energy for thermal quenching and T is the temperature. Accordingly, the R_{nr} will increase with an increase in temperature which subsequently increases the non-radiative relaxation probability from $^4G_{5/2}$ level and thus emission intensity decreases as depicted in Fig. 4.10(a). The emission intensity of 2.0 mol% doped CBV phosphor has retained 85.2 % at 443 K of its initial value at 323 K. Employing the Arrhenius equation (1.12), the activation energy (ΔE_a) i.e. a measure of thermal stability is reckoned for the as-prepared phosphors [163]. According to the equation (1.12), slope evaluated from linear fitted graph between $\ln[(I_O/I_T) - 1]$ and $\frac{1}{k_B T}$ for the $^4G_{5/2} \rightarrow {}^6H_{9/2}$ transition provides the ΔE_a value. The value of ΔE_a is 0.235 eV using the slope of the graph shown in Fig. 4.10(b), which is more than the reported elsewhere [164, 165]. More activation energy of the phosphor indicates more thermal

stability. Consequently, the above-mentioned results indicate that Sm^{3+} doped CBV phosphor possesses appreciable thermal stability and suitable for high powered w-LEDs.

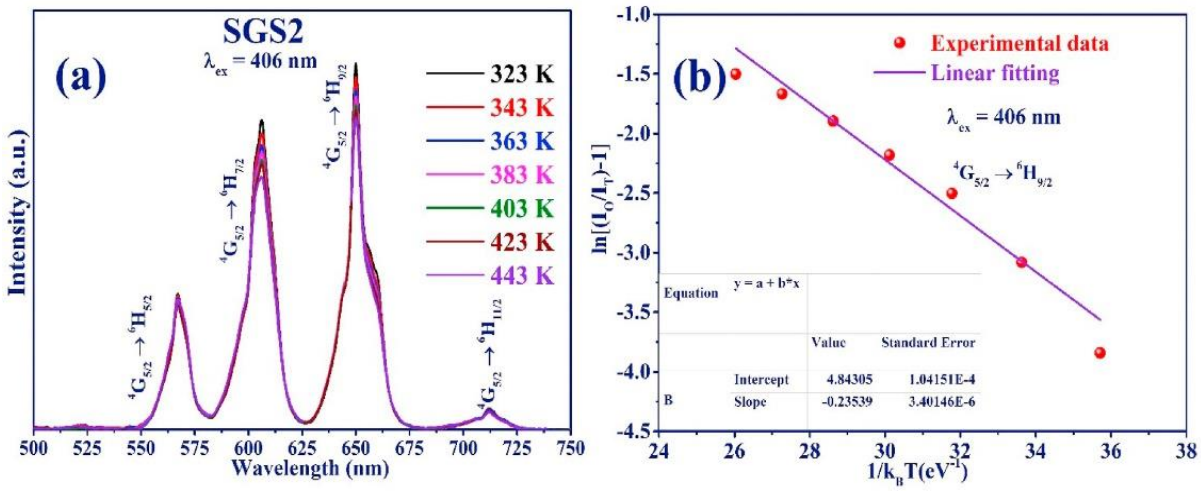

Figure. 4.10. *(a) Temperature dependent PL for SGS2 phosphor under 406 nm excitation and (b) Arrhenius plot for 649 nm emission wavelength under 406 nm excitation*

4.4. Conclusions

In summary, the present work deals with the comparative analysis of structural, morphological and PL properties of Sm^{3+} doped $CaBiVO_5$ phosphors synthesized via three different potential routes (SSR, CB and SG). Though, CBV: Sm^{3+} phosphors successfully synthesized via diverse routes, the diffraction peaks for all synthesized phosphors correspond to the standard JCPDS data (card no: 81-1775). The SEM results reveal that CBV: Sm^{3+} phosphors were synthesized with improved homogeneity and shape regularity at lower reaction temperature via SG method. The emission spectra measured under 275 and 343 nm excitations exhibit sharp bands in orange/orangish-red spectral range along with weak host emission band. While, the emission spectra observed under 406 nm excitation for CBV: xSm^{3+} (1.0 mol% ≤ x ≤ 5.0 mol%) exhibit similar sharp bands with no host emission. The CBV: Sm^{3+} phosphors synthesized via SG method exhibits significant enhancement in emission intensity under n-UV excitation in comparison to other methods. The concentration quenching phenomenon is observed beyond 2.0 mol% Sm^{3+} concentration due to electric dipole-dipole interaction

between Sm^{3+} ions in proximity as revealed by Dexter's theory and I-H model. The CBV: Sm^{3+} phosphor exhibit color tunability as chromaticity coordinates shifts from orange to orangish-red region in CIE diagram by changing excitation wavelength from 275 to 343 and finally to 406 nm. The CIE coordinates under λ_{ex}= 275 nm (0.567, 0.404) and λ_{ex}= 343 nm (0.591, 0.399) are found close to Nichia corporation fabricated amber LED NSPAR 70BS (0.570, 0.420). The lifetime values for $^4G_{5/2}$ level have been calculated with varying concentrations in CBV phosphors and found to be in microseconds (μs) range at λ_{ex}= 343 nm. Further, temperature dependent PL indicates commendable thermal stability of SG derived Sm^{3+} doped CBV phosphor. Based on the comparative studies, SG route is the best suited approach to synthesize thermally stable CBV: Sm^{3+} phosphors with enhanced orange/orangish-red color emission under UV/n-UV excitation for its effective utilisation in w-LEDs applications.

Chapter 5

Spectroscopic and color tunable studies in Dy^{3+}/Eu^{3+} co-doped calcium bismuth vanadate phosphors for lighting applications

Single phase Dy^{3+} activated and Dy^{3+}/Eu^{3+} bi-activated calcium bismuth vanadate (CBV) phosphors are synthesized via citrate-gel method to achieve white light emission and color-tunability. The phase purity and quasi-spherical particle with few agglomerations of the as-prepared CBV phosphors are indicated by structural and morphological characterizations, respectively. The emission spectral properties and energy transfer in Dy^{3+} doped and Dy^{3+}/Eu^{3+} co-doped CBV phosphors have been examined extensively. In this regard, Dy^{3+}/Eu^{3+} co-doped CBV phosphors were pumped by near-ultraviolet (n-UV) light (387 nm) and the maximum energy transfer efficiency value of 87.5% is observed. The Dexter and Reisfeld's approximation applied to emission spectra specifies electric dipolar-dipolar interaction to be accountable for Dy^{3+} to Eu^{3+} energy transfer. In CBV: Dy^{3+} phosphors, co-doping with Eu^{3+} ions facilitates red component that ensues warm white light emission under n-UV/blue light excitation. Moreover, Dy^{3+}/Eu^{3+} co-doped CBV phosphor exhibit flexible color tunability with increasing Eu^{3+} concentration under different excitations. The significant accomplishments like warm white light emission and controllable spectral composition in Dy^{3+}/Eu^{3+} co-doped CBV phosphor by altering the excitation energy and co-dopant (Eu^{3+}) concentration potentiate it as a suitable candidate in the domain of lighting and display devices.

5.1. Introduction

The recent decade has witnessed unprecedented interest in white light emitting diodes (w-LEDs) over conventional lighting devices due to its prolific virtues such as low power consumption, non-toxicity, improved efficiency and advanced durability [166-168]. The commercialized approach for phosphor based w-LEDs includes the yellow phosphor (YAG: Ce^{3+}) coating over blue LED chip [169, 170]. However, such fabricated w-LEDs suffer from deteriorated color rendering index (CRI) and correlated color temperature (CCT) values due to insufficient red component in the combined spectral emissions. Therefore, researchers have been adopting an alternative of coating multi-phase phosphor, i.e., an appropriate composition of RGB (R: red, G: green and B: blue) phosphors on UV/near UV (n-UV) LED. However, a multi-phase phosphor approach leads to depreciated efficiency because of the re-absorption of blue emission by RG phosphors [171, 172]. All such shortcomings can be resolved by adopting another sophisticated approach of coating co-activated single-phase phosphor that can provide warm white light emission. As-prepared co-activated single-phase phosphor can offer excellent color reproducibility, sufficient CCT, spectral tunability, and soothing perception to eyes [173, 174]. Among various available RE ions, Dy^{3+} activated phosphor is predominantly utilized to generate white light as single phase phosphor due to its two prominent emission bands in yellow (Y) and blue (B) spectral region. The fluorescent intensity ratio (Y/B) of these two bands may be adjusted to a precise value for white light generation by modifying Dy^{3+} ion concentration [175]. But due to scarcity of red component, such fabricated w-LEDs may also suffers from low CRI and elevated CCT value. However, co-doping with red emitting ions in such Dy^{3+} doped phosphors can result in cool to warm white light tunability and improvement in CRI values [176]. The red emitting component can be derived from ions which when co-doped in the proposed host lattice shows appreciable spectral overlap of its excitation with Dy^{3+} emission, which are found to be Eu^{3+} ions in the present case. Therefore, the development of

Dy^{3+}/Eu^{3+} co-doped CBV phosphor and exploring involved energy transfer between Dy^{3+} and Eu^{3+} to accomplish spectral tunability via altering excitation energy as well as amount of dopant ion concentration have become a prime motive for the work presented in this chapter.

Presently, a set of Dy^{3+} singly doped and Dy^{3+}/Eu^{3+} doubly doped calcium bismuth vanadate phosphors were successfully synthesized via citrate-gel method. The structural and morphological studies have been done to ascertain the phase purity and particle size/shape of the prepared phosphors. Moreover, the luminescent properties, colorimetric properties and decay dynamics have been thoroughly investigated to explore the involved energy transfer mechanism and potentiality of the as-synthesized CBV phosphors for essential applications such as spectrally and CCT tunable devices as well as w-LEDs.

5.2. Sample preparation

To synthesize CBV ($CaBiVO_5$) phosphors with doping of Dy^{3+} ions and co-doping of Eu^{3+} ions via citrate sol-gel method, the $Eu(NO_3)_3$ and $Dy(NO_3)_3$ are dissolved separately in sufficient amount of de-ionized (DI) water as per the required mole ratios. The starting materials ($Ca(NO_3)_2.4H_2O$ and $Bi(NO_3)_3.5H_2O$) were taken in stoichiometric ratio, which are also dissolved individually in nitric acid. The hot DI water is used to dissolve the NH_4VO_3 powder taken in stoichiometric amount. The detailed procedure is given in section 2.2.2. of the chapter 2 and flow chart of synthesis is represented in Fig. 2.2 The samples were labelled as CD0, CD1, CD2, CD3, CD4 and CD5 for 0.0, 1.0, 2.0, 3.0, 4.0, and 5.0 mol% doping of Dy^{3+} ions in CBV host, respectively. The sample name CD1E1 is mentioned for 1.0-1.0 mol% co-doping of Dy^{3+}-Eu^{3+} ions in CBV host, respectively. The synthesized samples are named as CDE1, CDE3, CDE5, CDE7 and CDE8 are designated for 4.0 mol% Dy^{3+} fixed doping with respective co-doping of 1.0, 3.0, 5.0, 7.0 and 8.0 mol% of Eu^{3+} ions in CBV phosphors.

5.3. Results and discussion

5.3.1. XRD analysis

The representative XRD patterns for un-doped (CD0), Dy^{3+} doped (CD1 and CD4) and Dy^{3+}/Eu^{3+} doubly doped CBV phosphors (CDE1, CDE7 and CDE8) are displayed in Fig. 5.1. All the diffraction patterns are found consistent with the standard XRD profile of $CaBiVO_5$ (JCPDS file no.: 81-1775) and no noteworthy impurity peaks were detected. The non-existence of any extra diffraction peaks in all the represented XRD patterns confirm the pure phase formation of calcium bismuth vanadate phosphor with orthorhombic structure in D_{2h}^{15}-Pbca space group. Further, the full agreement of diffraction patterns of differently doped CBV phosphors with the standard XRD profile of $CaBiVO_5$ implies that the varying dopant (Dy^{3+}) and co-dopant (Eu^{3+}) ion concentrations had not induced any structural changes.

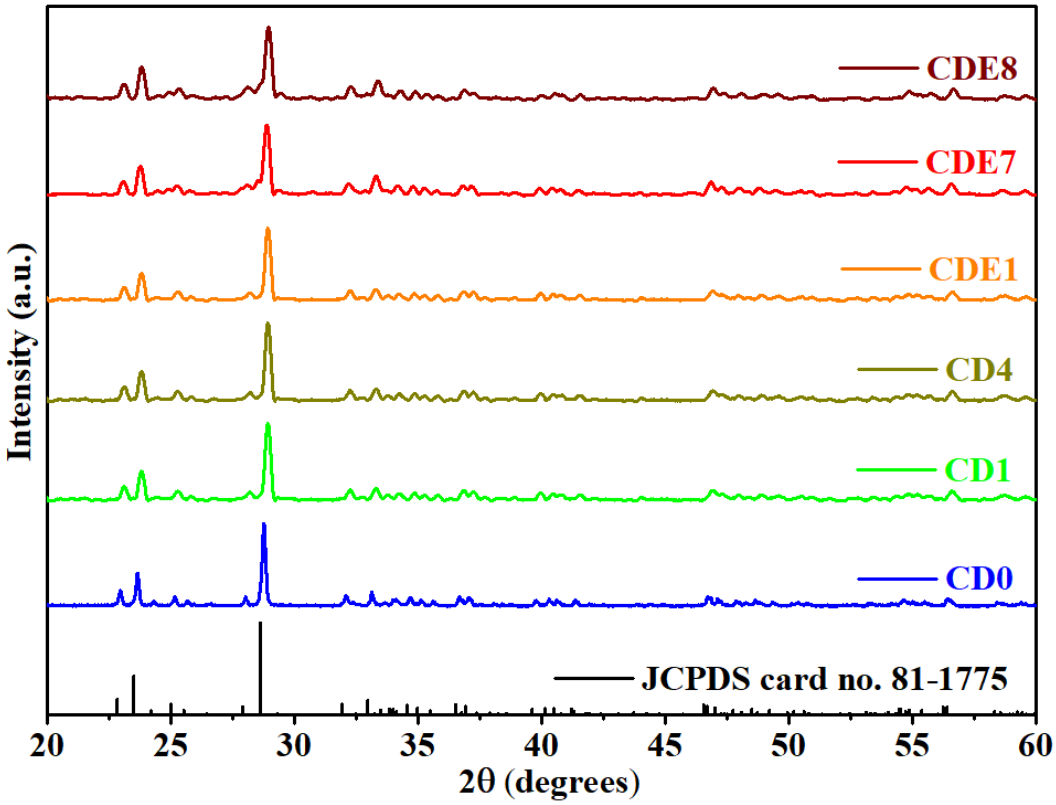

Figure 5.1. *XRD patterns for un-doped (CD0), Dy^{3+} singly doped (CD1 and CD4) and Dy^{3+}/Eu^{3+} co-doped (CDE1, CDE7 and CDE8) CBV phosphors*

As a result, the successful incorporation of Dy^{3+} (ionic radii = 0.912 Å) and Eu^{3+} (ionic radii = 0.947 Å) ions at six coordinated Bi^{3+} (ionic radii = 1.03 Å) sites is expected due to similar ionic radii and same valence state. Moreover, the crystallite sizes estimated using equation (2.2) for CD0, CD1, CD4, CDE1, CDE7 and CDE8 are 26.4, 24.3, 23.8, 22.2, 21.3 and 20.6 nm, respectively. The crystallite size declines with an increase in doping concentrations due to the lattice contraction effect as dopants/co-dopants (Dy^{3+} or Eu^{3+}) of smaller radii have substituted the cations (Bi^{3+}) with larger ionic radii [177].

5.3.2. Morphological observations

Fig. 5.2 represents the SEM image of CDE1, revealing the surface morphology of as-synthesized Dy^{3+}/Eu^{3+} co-doped CBV phosphor. The surface morphology shows mostly spherical grains with clear textural boundaries. Some of the particles coalesced together to forms chunks with a size of not more than few micrometres. The micrometre-sized particle formation further reinforces the potential utility of synthesized Dy^{3+}/Eu^{3+} doped CBV phosphor in commercial LEDs.

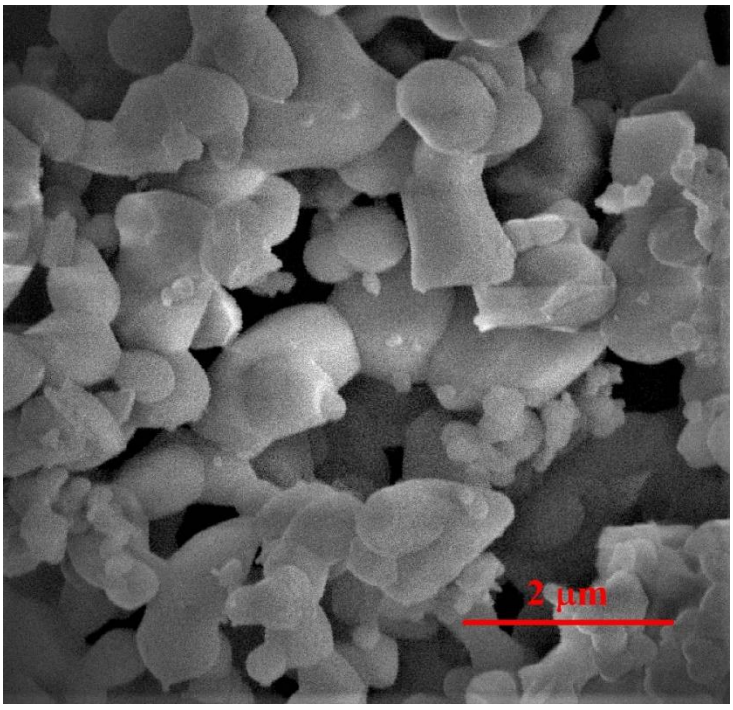

Figure 5.2. *SEM image of CDE1 sample*

5.3.3. Photoluminescence properties

The photoluminescence studies for CBV phosphors with Dy^{3+} doping and Dy^{3+}/Eu^{3+} co-doping are performed by measuring the excitation and emission spectra. Fig. 5.3 depicts the excitation spectral profiles of $CaBi_{1-x}VO_5$: xDy^{3+} (x = 1.0 - 5.0 mol%) observed for 574 nm emission wavelength. The excitation spectra exhibit an intense broad-band and several sharp peaks in the spectral range of 250-500 nm. The spectral bands observed in the UV to n-UV region can be attributed to the host (CBV) band as discussed in the chapter 3 [73]. The sharp excitation peak at 353 nm observed to be embedded on host excitation band in n-UV region can be attributed to Dy^{3+} ions ($^6H_{15/2} \rightarrow {}^6P_{7/2}$). Moreover, other peaks located at 366, 387, 426, 455, 474 nm attributed to the Dy^{3+} transitions from the lowest state ($^6H_{15/2}$) to multiple respective higher states $^6P_{5/2}$, $^4I_{13/2}$, $^4G_{11/2}$, $^4I_{15/2}$ and $^4F_{9/2}$, respectively [178, 179].

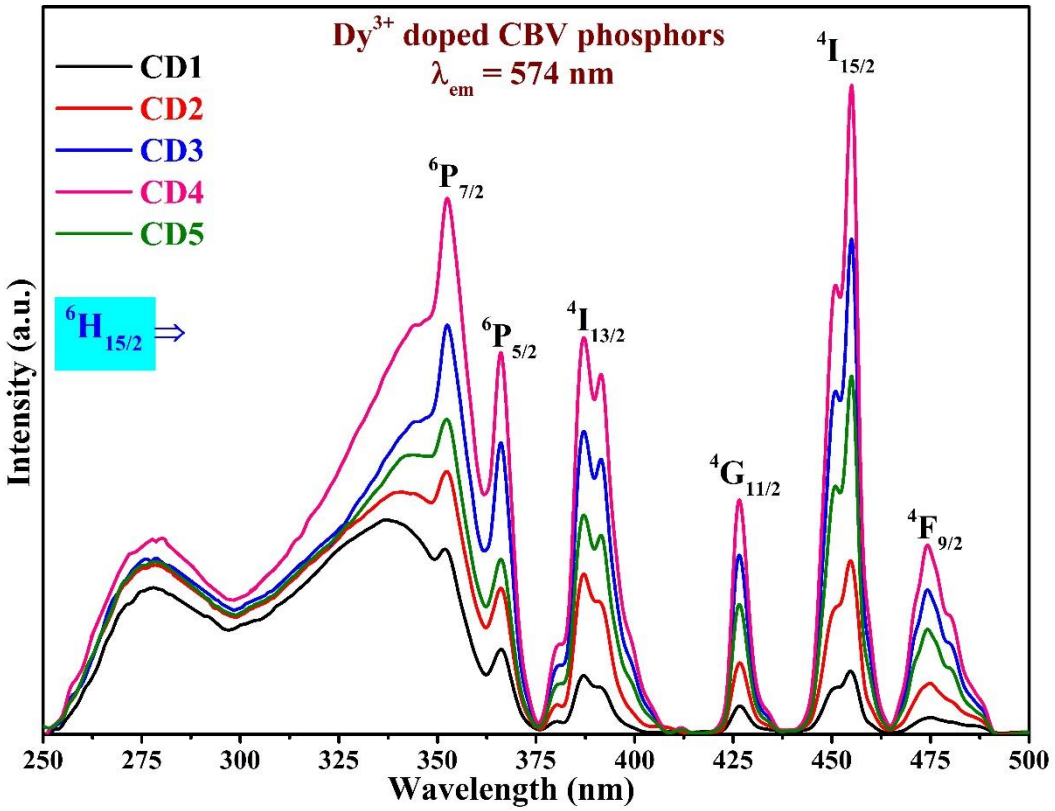

Figure 5.3. *Excitation spectra of CD1-CD5 samples by monitoring emission at 574 nm wavelength*

Among all the peaks, the excitation peak accommodating the highest intensity is situated at 455 nm wavelength illustrating the maximum absorption possible at this specific wavelength. Therefore, the emission spectral studies of all CBV: Dy^{3+} phosphors have been accomplished for 455 nm excitation wavelength. Moreover, to study emission properties of Dy^{3+} doped CBV phosphors under the effect of host excitation, the CBV: Dy^{3+} phosphors are being excited at the second most intense peak located at 353 nm (n-UV region), which is a combination of host excitation and Dy^{3+} transition. Fig. 5.4 (a) depicts the PL spectra recorded for $CaBi_{1-x}VO_5$: xDy^{3+} (x = 1.0 - 5.0 mol%) phosphors under 353 nm excitation. It exhibits two strong emission bands at 488 nm (blue: B), 574 nm (yellow: Y) and a very feeble band at 668 nm (red: R) credited to Dy^{3+} transitions (i.e. $^4F_{9/2} \rightarrow {}^6H_J$, the value of J is 15/2, 13/2 and 11/2, respectively) [179].

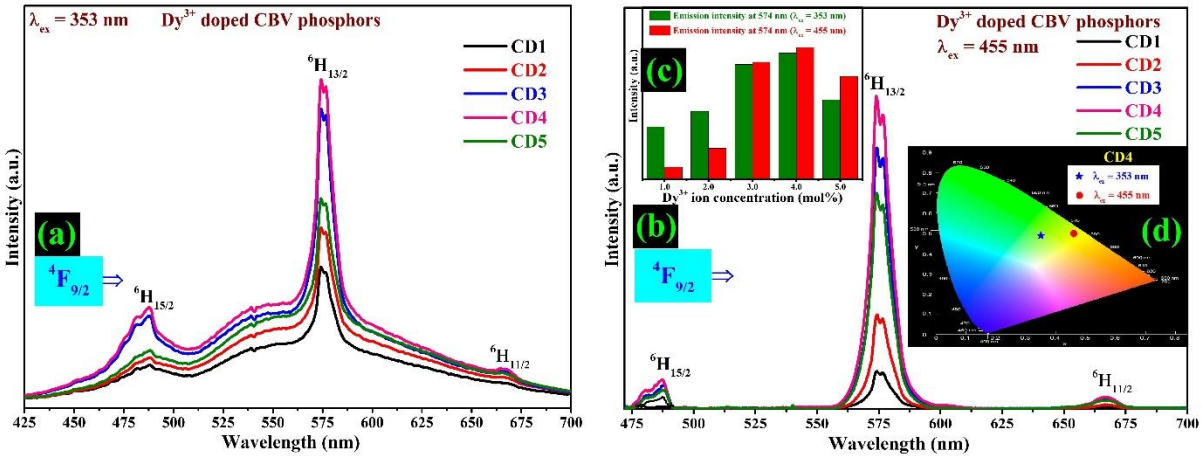

Figure 5.4. *Emission spectra of CD1-CD5 phosphors under excitations at (a) 353 nm and (b) 455 nm, (c) Emission intensity variation with different concentrations of Dy^{3+} ions and (d) Color coordinates of the CD4 under different excitation wavelengths*

Above mentioned sharp bands corresponding to Dy^{3+} ions are observed to be embedded on a weak and broad emission band with maxima approximately at 542 nm ascribed to (CBV) host reported in chapter 3 [73]. Further, Fig. 5.4 (b) shows the emission spectra for CD1-CD5 phosphors under 455 nm excitation. The emission spectra for all the Dy^{3+} activated CBV phosphors under 455 nm excitation exhibit peaks solely attributed to the Dy^{3+} transitions.

Moreover, it can be observed that the peaks exhibit splitting into maximum $J + \frac{1}{2}$ number of stark components in the blue and yellow spectral regions owing to the crystal field around the Dy^{3+} ions [180, 181]. The emission peaks situated at 488 (B) and 574 nm (Y) individually correspond to allowed magnetic dipolar (MD) and forced electric dipolar (ED) transitions, respectively [24, 25]. The integrated intensity ratio of peaks due to ED and MD transitions is called as asymmetry ratio. The observed prominence of peak due to ED transition ($^4F_{9/2} \rightarrow {}^6H_{13/2}$) in the emission spectra and asymmetry ratio for all the Dy^{3+} doped CBV phosphor greater than unity under 455 nm excitation, suggest that the Dy^{3+} ions are located at lattice sites with no inversion symmetry in the CBV host matrix [76]. Further, it is conspicuous from the Fig. 5.4(c) that the luminescence intensity enhances with increment in Dy^{3+} ions concentration till 4.0 mol% and declines beyond it for both the excitations (353 and 455 nm) due to the well-known concentration quenching process. At higher ion concentrations (beyond 4.0 mol%), the absorbed energy is probably transferred non-radiatively among activator (Dy^{3+}) ions due to decreased distance in-between them instead of releasing it radiatively [182]. Hence, 4.0 mol% of Dy^{3+} ion concentration is found to be the optimized for CBV host matrix with emission color falls in greenish-yellow (λ_{ex} =353 nm) and yellowish (λ_{ex} = 455 nm) region (Fig. 5.4(d)). Such Dy^{3+} ion singly doped CBV phosphors exhibit a very less intense red emission. Therefore, Eu^{3+} ions have been co-doped in the optimized Dy^{3+} (4.0 mol%) doped CBV phosphors for enhancing red component to obtain pure white light with improved CRI and also to achieve color-tunability.

Fig. 5.5 represents the excitation spectra of CD1E1 (1.0 mol% Dy^{3+} and 1.0 mol% Eu^{3+} co-doped CBV) phosphors observed for most intense emission wavelengths of Dy^{3+} (574 nm) and Eu^{3+} (613 nm). The excitation spectrum of CD1E1 phosphor observed for 574 nm emission wavelength exhibit broad and sharp excitation bands as discussed above. Furthermore, the excitation spectrum by monitoring emission at 613 nm includes broad bands and few sharp

peaks in 250-500 nm range. The broad bands are due to CBV host (275 & 316 nm) and an overlap of CBV host band with ligand to metal (O^{2-} to Eu^{3+}) charge transfer band (342 nm). The sharp peaks are credited to Eu^{3+} transitions from ground state i.e. $^7F_0$ to $^5L_7$ (382 nm), $^5L_6$ (393 nm) and $^5D_2$ (464 nm) excited states of Eu^{3+} ions [73]. Moreover, the inset of Fig. 5.5 represents the pre-requisite for Dy^{3+} to Eu^{3+} energy transfer, i.e., the spectral overlap of sensitizer (Dy^{3+}) emission ($^4F_{9/2} \rightarrow {}^6H_{15/2}$) and activator ($Eu^{3+}$) excitation ($^7F_0 \rightarrow {}^5D_2$). The co-doped CBV phosphors have been excited under various wavelengths such as 353, 387, 455 and 464 nm lying in n-UV and blue spectral regions to reveal energy transfer and color-tunability in Dy^{3+}/Eu^{3+} bi-activated CBV phosphors. The effective absorption in n-UV and blue spectral regions for CD1E1 phosphor suggests the potential utilization of this phosphor as n-UV and blue LEDs as a pumping source.

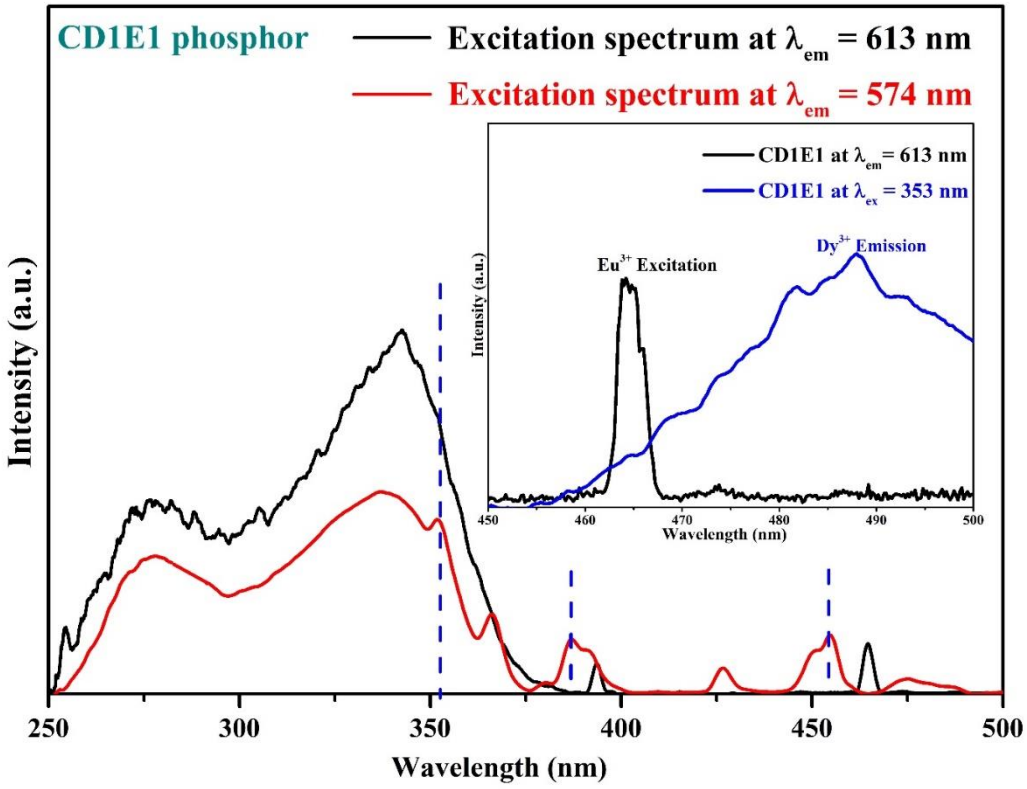

Figure 5.5. *The excitation spectra for CD1E1 phosphor for observing emission at 574 and 613 nm wavelengths (Inset: Spectral overlap of sensitizer (Dy^{3+}) emission and acceptor (Eu^{3+}) excitation)*

Fig. 5.6 (a-d) represents emission spectra of CDE (Dy^{3+}/Eu^{3+} bi-activated CBV) phosphors under 353, 387, 455 and 464 nm excitations, respectively, in which the Dy^{3+} ion concentrations are fixed at its optimal value (4.0 mol%) and Eu^{3+} ion concentrations have been varied between 1.0 - 8.0 mol% range. The emission spectra exhibit various bands in blue (B), yellow (Y), orange (O) and red (R) regions of the visible spectrum ascribed to the transitions between the levels of Dy^{3+} and Eu^{3+} ions. The emission bands exhibited at 488, 574 and 668 nm wavelengths can be ascribed to Dy^{3+} transitions ($^4F_{9/2} \rightarrow {}^6H_J$), as discussed earlier. Except that, the emission peaks observed in the co-doped samples at 537, 580, 593, 613, 653 and 704 nm wavelengths are credited to distinctive transitions of Eu^{3+} ions from $^5D_1$ and $^5D_0$ levels to lower levels [73]. The $^5D_0 \rightarrow {}^7F_2$ (in red region) is an ED allowed transition characterized as hypersensitive transition and strongly affected by the crystal field in the local environment. While $^5D_0 \rightarrow {}^7F_1$ (in orange region) is an MD allowed transition and is non-sensitive to the crystal field created by the ligand atoms. Further, it is clear from the Fig. 5.6 (a-d) that the excitation wavelengths and Eu^{3+} ion concentration can significantly influence the emission intensity of peaks corresponding to Dy^{3+} and Eu^{3+} ion. Under 353 nm excitation (Fig. 5.6(a)), which is a combined excitation wavelength of host, Dy^{3+} ions and ligand to metal (O^{2-} to Eu^{3+}) charge transfer band, the emission spectra is dominated by Eu^{3+} emission, but also emission band due to the host and several peaks due to Dy^{3+} ions are observed [73, 183]. Under 353 nm excitation, the Eu^{3+} emission is observed to be increasing with increase in Eu^{3+} concentration due to combined effect of increased absorption probability by Eu^{3+} ions and energy transfer from Dy^{3+} ions to Eu^{3+} ions at this excitation wavelength. The energy transfer from Dy^{3+} to Eu^{3+} ions is more evident under 387 and 455 nm excitations (which are purely Dy^{3+} excitations (as depicted in Fig. 5.6 (b&c)). Under 387 and 455 nm excitations, the Dy^{3+} emission is dominating initially with respect to emission due to Eu^{3+} ions and afterwards the Dy^{3+} emission decreases while Eu^{3+} emission increases with increase in Eu^{3+} ion concentration. This

observation can be explained as the effect of energy transfer from the sensitizer (Dy^{3+}) to activator (Eu^{3+}) ion [176]. Whereas under 464 nm excitation (Fig. 5.6(d)), emission spectra exhibit peaks purely due to Eu^{3+} ions confirming there is no back energy transfer from Eu^{3+} to Dy^{3+} ions. Under all excitation wavelengths, the Eu^{3+} emission is observed to be increasing till 7.0 mol% concentration of Eu^{3+} ions and decreases beyond it due to concentration quenching. Hence, it is conspicuous from Fig. 5.6(a-d) that the emission intensity of peaks derived from different energy levels of Dy^{3+} and Eu^{3+} ions is variable under different excitation wavelengths and different concentrations of Eu^{3+} ions. Therefore, color tunabilty can be accomplished either via host to RE ion energy transfer or by varying the excitation wavelengths and ion concentrations of Eu^{3+} (activator).

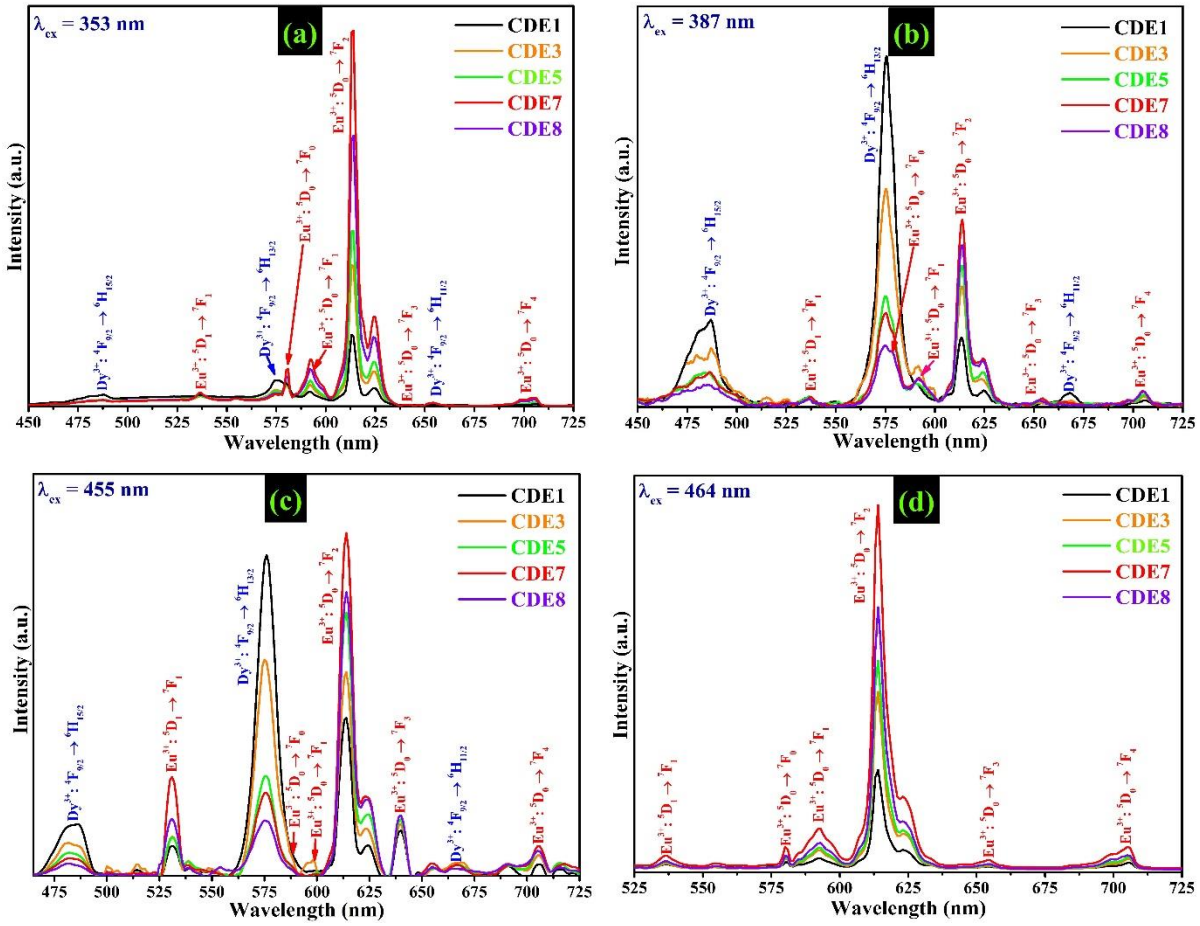

Figure 5.6. *(a-d) Emission spectra of CDE1, CDE3, CDE5, CDE7 and CDE8 samples under different excitation wavelengths (λ_{ex} = 353, 387, 455 and 464 nm)*

Fig. 5.7 epitomizes an energy level scheme for depicting the various PL and energy transfer processes mentioned above. When the light (UV/n-UV/blue range) incident on CBV: Dy^{3+}/Eu^{3+} phosphors, the energy may be taken up the host and it may get excited to $^1T_1$. Then host might either transfers its energy to closer lying $^6P_{7/2}$ level of Dy^{3+} as well as $^5L_7$ of Eu^{3+} ions (shown as a horizontally curved arrow in Fig. 5.7) or non-raditively relax to $^3T_1$ level and then emit radiatively to reach $^1A_1$ level. Through direct excitation of Dy^{3+} ions (387 or 455 nm) or indirect excitation via host, it may elevate to its excited states and emits blue and yellow light after few non-radiative relaxations. The energy levels ($^4I_{15/2}$ and $^4F_{9/2}$) of Dy^{3+} ions are close to $^5D_2$ and $^5D_1$ energy levels of Eu^{3+} ions, respectively [156]. Hence energy transfer may take place from excited states of Dy^{3+} ions to Eu^{3+} ions in CDE phosphors via phonon facilitated non-radiative relaxation and finally, radiative transitions in Eu^{3+} ions occur to provide red color emission [179].

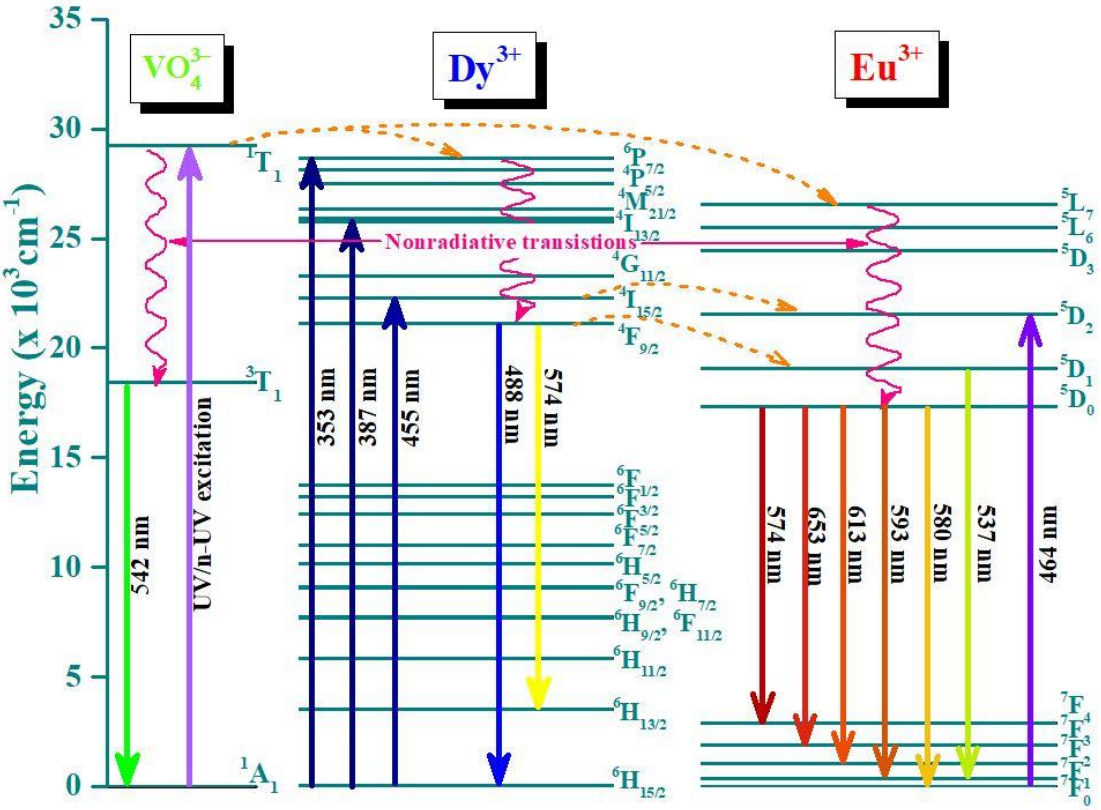

Figure 5.7. *Energy level diagram demonstrating energy transfers in CBV: Dy^{3+}/Eu^{3+} phosphors*

Different processes, namely exchange interaction or multipole-multipole interactions, may be responsible for non-radiative energy transfers from a donor (Dy^{3+}) to an acceptor (Eu^{3+}) ion. The pre-requisite for exchange interaction to take place is that the value of critical distance should be 5 Å or below. The critical distance ($R_{Dy\text{-}Eu}$) can be evaluated using the below-mentioned formula [73]:

$$R_{Dy-Eu} = 2\left(\frac{3V}{4\pi N X_c}\right)^{1/3} \quad (5.1)$$

where volume (V), number of cations (N) are fixed for a unit cell. For the present case, V= 946.22 $Å^3$ and N=8. The critical concentration (X_c) is taken as sum of optimized Dy^{3+} (4.0 mol% fixed) and Eu^{3+} ion concentration (3.0 mol%) at which Dy^{3+} emission intensity remained almost half of its origingal value i.e. X_c = 7.0 mol% [169, 184, 185]. Thus, the calculated R_c value comes out to be 14.77 Å confirming the occurrence of multipole-multipole interaction. To recognize the multipole-multipole interaction type, Dexter theory and Reisfeld's approximation can be used. It delivers the general dependence of quantum efficiency of Dy^{3+} ions without and with Eu^{3+} ion, respectively on the total (Dy^{3+} and Eu^{3+}) ion concentrations ($C_{Dy^{3+}+Eu^{3+}}$) (equation (1.15)) [56]. The value of 'n' signifying the multipolar interaction type, may take values as 6 (dipolar-dipolar: d-d), 8 (dipolar-quadrupolar: d-q) and 10 (quadrupolar-quadrupolar: q-q). The ratio of quantum efficiencies ($\frac{\eta_{s0}}{\eta_s}$) of Dy^{3+} emission without and with Eu^{3+} ions can be estimated by associated ratio of emission intensities ($\frac{I_{s0}}{I_s}$) as shown in equation (1.16) [183]. Here, I_{s0} and I_s are the intensities of emission peak due to Dy^{3+} ions ($^4F_{9/2} \rightarrow {}^6H_{13/2}$) without and with Eu^{3+} ions, respectively. The graphs of $\frac{I_{s0}}{I_s}$ versus $C_{Dy^{3+}+Eu^{3+}}^{n/3}$ corresponding to the value of n to be 6, 8, and 10 are shown in Fig. 5.8. It discloses that the best linear fit is with n = 6 suggesting the involvement of d-d interactions for Dy^{3+} to Eu^{3+} energy transfer. The associated energy transfer efficiency (η_{ET}) from donor (Dy^{3+}) to

acceptor (Eu^{3+}) can be evaluated using the equation (1.17) [183]. The efficiencies of energy transfer for CDE1, CDE3, CDE5, CDE7 and CDE8 found to be 26.9, 54.5, 77.1, 80.6 and 87.5% under 387 nm excitation, respectively.

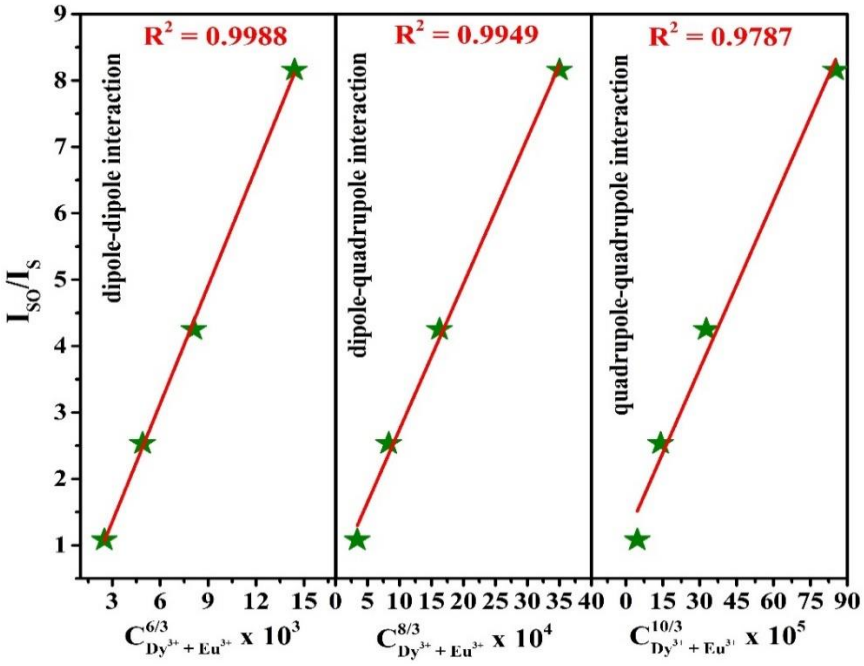

Figure 5.8. *Plot of* $\frac{I_{S0}}{I_S}$ *versus* $C^{n/3}_{Dy^{3+}+Eu^{3+}}$

5.3.4. Chromaticity coordinates

To assess the potentiality of white light emission and flexibility of color tunability in Dy^{3+}/Eu^{3+} bi-activated CBV phosphors, color coordinates from the emission data have been evaluated and marked in CIE 1931 diagram (Fig. 5.9) [39, 40]. The color coordinates for the optimized Dy^{3+} doped CBV phosphor (CD4) are found to be (0.35, 0.49) and (0.46, 0.50) under 353 and 455 nm excitations, respectively. The reckoned CIE coordinates for CD4 phosphor are plotted in the CIE diagram shown in Fig. 5.9 (b & d), respectively. Fig. 5.9(a) shows the multiple color emission from CDE1 phosphor such as greenish yellow (353 & 455 nm) to almost white (387 nm) and then red (464 nm) by modulating the excitation wavelengths. Moreover, the reckoned color coordinates (Table 5.1) for CDE phosphors under 353, 387 and 455 nm excitations (shown in Fig. 5.9 (b-d)) are found to be shifting towards red region by

varying co-dopant (Eu^{3+}) ion concentration. The achieved color-tunability due to $Dy^{3+} \rightarrow Eu^{3+}$ energy transfer is advantageous for diversified applications.

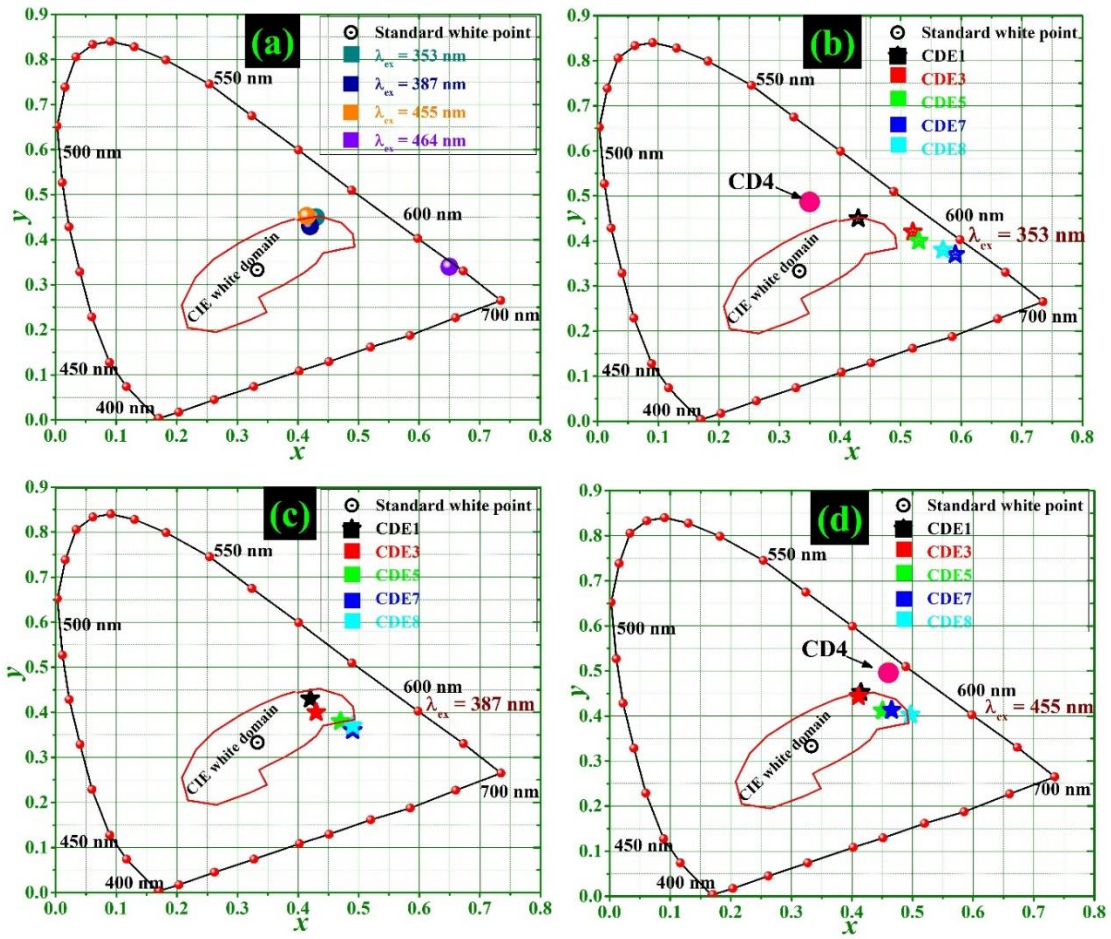

Figure 5.9. *CIE coordinates of (a) CDE1 under different excitations (353, 387, 455 and 464 nm), (b) CDE1-CDE8 phosphors under 387 nm excitation and (c & d) CD4 and CDE1-CDE8 phosphors under 353 and 455 nm excitations, respectively.*

Under 387 and 455 nm excitations, the color coordinates lie within CIE white domain indicating suitable applicability of Dy^{3+}/Eu^{3+} co-doped CBV phosphors in n-UV/blue light pumped w-LEDs. While color coordinates for all CDE phosphors under 464 nm wavelength are not showing any color variability and lie in pure red region (0.65, 0.34), which is also confirming no back transfer of energy from Eu^{3+} to Dy^{3+} as mentioned earlier. Further, Table 5.1 provides the CCT values of the as-prepared CBV phosphors under different wavelengths and increasing Eu^{3+} concentrations. The CCT values for CD4 (Singly Dy^{3+} doped) under 353 and 455 nm excitations are found to be 5140 and 3220 K, respectively. But the CCT

values of CDE phosphors under different excitations (mentioned in Table 5.1) are tunable and indicating warm white light emission via co-doping Eu^{3+} ions. Above mentioned colorimetric properties of the as-prepared CBV: Dy^{3+}/Eu^{3+} phosphors accomplish their utility in white lighting and color tunable devices employing n-UV/ blue LED as an excitation source.

Table 5.1. *CIE colour coordinates and CCT values for Dy^{3+} doped and Dy^{3+}/Eu^{3+} co-doped CBV phosphors under different excitations*

Parameter	Excitation Wavelength (nm)	Sample code				
		CDE1	**CDE3**	**CDE5**	**CDE7**	**CDE8**
CIE Coordinates (x, y)	**353**	(0.43, 0.45)	(0.52,0.42)	(0.53, 0.40)	(0.59, 0.37)	(0.57, 0.38)
	387	(0.42, 0.43)	(0.43, 0.40)	(0.47, 0.38)	(0.49, 0.36)	(0.49, 0.37)
	455	(0.41, 0.45)	(0.41,0.44)	(0.45, 0.41)	(0.46, 0.41)	(0.49, 0.40)
CCT (K)	**353**	3451	2081	1897	1762	1720
	387	3376	3105	2274	1974	1941
	455	4290	3971	3710	2212	2150

5.3.5. Decay curve analysis

Fig. 5.10 shows the decay plots of CD4, CDE1, CDE3, CDE5, CDE7 and CDE8 phosphors for $^4F_{9/2}$ level (Dy^{3+}) under 387 nm. The decay curves are most accurately fitted with bi-exponential equation. Using the fitting results, the values of average lifetime for $^4F_{9/2}$ level of Dy^{3+} (Table 5.2) under 387 nm excitation for CBV: Dy^{3+}/Eu^{3+} phosphors indicate a downtrend with increasing Eu^{3+} ion concentration confirming Dy^{3+} to Eu^{3+} energy transfer. The energy transfer probability rate (P) of dipolar-dipolar energy transfer can be evaluated using decay time values without (τ_0) and with (τ) doping of Eu^{3+} ions in CBV phosphors as per the equation [184]:

$$P = 1/\tau - 1/\tau_0 \quad (5.2)$$

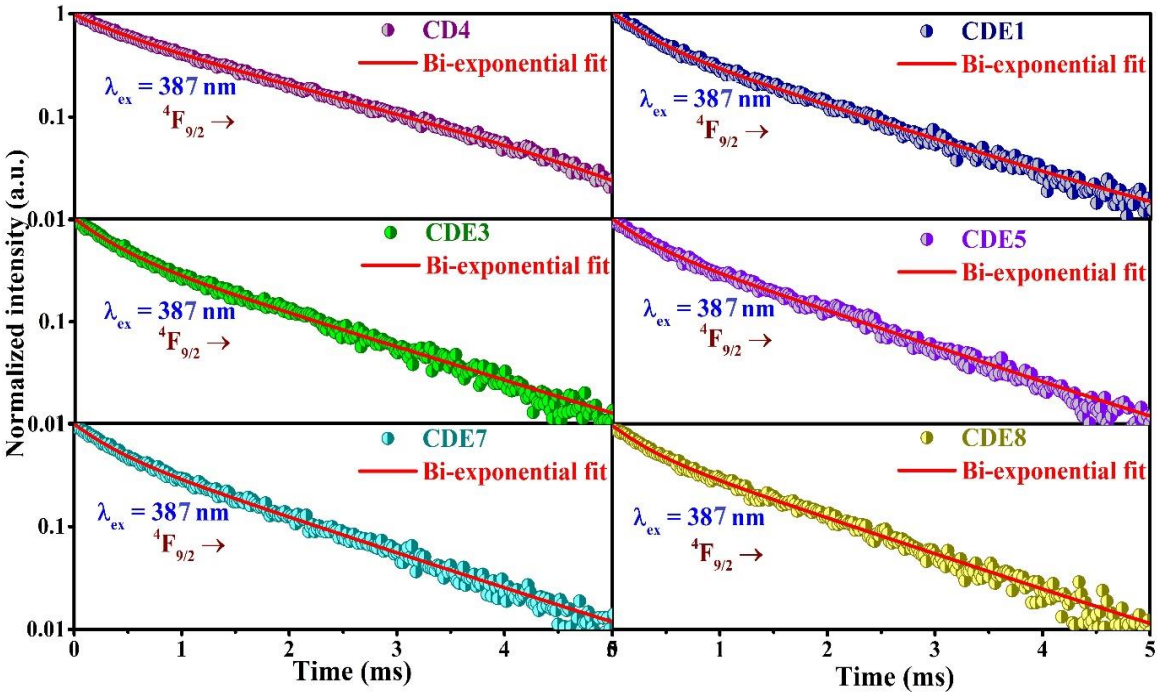

Figure 5.10. *The decay plots CD4, CDE1, CDE3, CDE5, CDE7 and CDE8 phosphors for $^4F_{9/2}$ level under λ_{ex} = 387 nm excitation*

The calculated energy transfer probability rates with varying Eu^{3+} doping concentration in CDE phosphors are given in the Table. 5.2. The lifetime values and energy transfer probabilities for CDE1, CDE3, CDE5, CDE7 and CDE8 phosphors have been plotted in Fig. 5.11. The energy transfer probability rates are shown to improve and lifetime reduced with enhancement of Eu^{3+} ion concentration in CBV phosphors.

Table 5.2. *Average lifetime, quantum efficiency and energy transfer probability rates for different Dy^{3+} doped and Dy^{3+}/Eu^{3+} co-doped CBV phosphors*

Sample code	Average decay time (μs)	Energy transfer probability rate (× 10^3 s^{-1}) (P)
CD4	137	-
CDE1	126	0.62
CDE3	124	0.76
CDE5	123	0.84
CDE7	122	0.92
CDE8	120	1.06

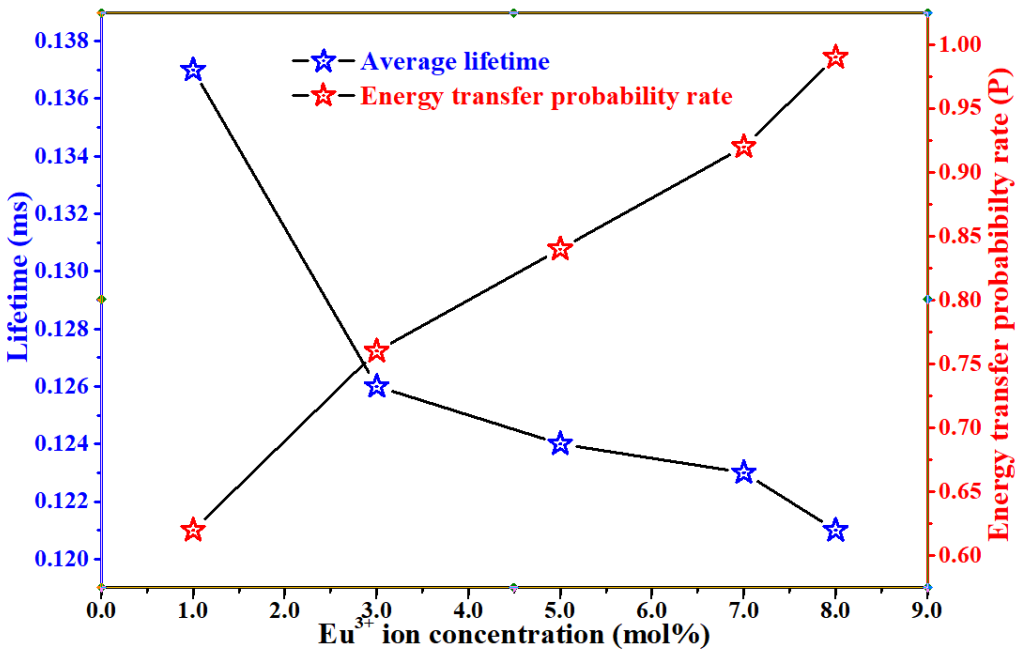

Figure 5.11. *The decay time vs. energy transfer probability rate with increasing Eu^{3+} ion concentrations (λ_{ex} = 387 and λ_{em} = 574 nm)*

5.4. Conclusions

A set of Dy^{3+} activated and Dy^{3+}/Eu^{3+} bi-activated CBV phosphors were prepared via citrate sol-gel technique. The XRD analysis indicate pure orthorhombic structure formation for CBV: Dy^{3+}/Eu^{3+} phosphors since all the diffraction patterns are well agreed with JCPDS standard data having card no. 81-1775. The SEM micrograph discloses a mixture of round and few agglomerated micro-range structures with soft edges. The emission spectra observed for Dy^{3+} activated CBV phosphors under different excitations exhibit intense blue and yellow emission bands. For Dy^{3+}/Eu^{3+} co-doped CBV phosphors, emission color tunability observed from greenish-yellow to red via white region by controlling co-dopant concentration and excitation wavelengths. Moreover, Dexter & Reisfeld's approximation reveals that the Dy^{3+} to Eu^{3+} energy transfer takes place via dipolar-dipolar interaction. The decay plots are most accurately fitted with bi-exponential equations and reveal a reduction in decay time values with

a rise in concentrations of Eu^{3+} ions. All the above mentioned research outcomes illustrate that Dy^{3+} singly doped and Dy^{3+}/Eu^{3+} doubly doped CBV phosphors are the potential candidates for w-LEDs and color tunable display devices.

Chapter 6

Development of deep red emitting $CaBiVO_5$: Pr^{3+} phosphors for multi-functional optoelectronic applications

Orthorhombic Pr^{3+} doped calcium bismuth vanadate (CBV: Pr^{3+}) phosphors have been synthesized successfully via a citrate sol-gel method. The single phase formation of CBV: Pr^{3+} phosphor has been endorsed by X-ray diffraction (XRD) analysis. The scanning electron microscopy (SEM) image reveals dense particle packaging with the quasi-spherical shape for the prepared CBV: Pr^{3+} phosphors. Under blue light excitation, CBV: Pr^{3+} phosphors exhibit intense red emission bands located at 608 and 656 nm wavelengths, overlapping with the absorption spectrum of P_R phytochrome, which is present in plants. To achieve the maximum red intensity, the Pr^{3+} ion concentration is optimized to be 1.25 mol% in the CBV host, after which the emission intensity ceases due to concentration quenching. Dexter's theory disclosed the possibility of d-d multipolar interaction amongst Pr^{3+} ions at higher concentrations of Pr^{3+} ions in the CBV host. The CIE coordinates are found to be positioned in the pure red region for CBV: Pr^{3+} phosphor and in the proximity of red-emitting commercial phosphor. The temperature-dependent spectral studies manifest substantial thermal stability of the as-synthesized phosphor. All the studies mentioned above specify the tremendous potentiality of thermally stable CBV: Pr^{3+} phosphor in agricultural lighting and w-LED applications.

6.1. Introduction

The ongoing energy crises, drought threats and increasing food demands have led the interest of masses towards indoor plant cultivation equipped with smart lighting systems. For plant growth under such controlled systems, lighting devices emitting specifically in blue (B), red (R), and far-red (FR) spectral region is an indispensable requirement. Such an advanced lighting system may drive photosynthesis and also beneficial for germination, flowering, fruitages and other crucial morphogenesis of plants [65, 66]. Apart from chlorophyll (a photosynthetic pigment), two photo-interconvertible phytochromes/photoreceptors (P_R and P_{FR}) exhibiting different absorption spectra are also present in plants. The P_R absorbs red light in the daytime to convert into P_{FR}, whereas in the night, P_{FR} absorbs FR light to convert it into P_R. The P_R and P_{FR} play crucial roles in plant growth and flowering. For instance, the red light absorption by P_R could alter flowering process ahead of scheduled time in long-day plants. In contrast, sensitization of P_{FR} via FR illumination could alter gene expression of plant structure and stimulate the growth. The different red to FR light ratios usually led to various physiological variations in plants from vegetative to floral development. Therefore, artificial lighting with an adjustable R to FR light ratio is paramount for controlling the flowering and physiological changes in plants [66, 68]. In recent times, phosphor converted light emitting diodes (pc-LEDs) are being perceived as smart lighting sources with the capability of controlling spectral composition via phosphor coated over the LED chip [63, 64, 186]. The emission from pc-LED matching well with plant photoreceptors (P_R and P_{FR}) can offer ideal production in plant growth systems. Besides this, pc-LED delivers numerous advantages over prevailing lighting sources (incandescent, metal halide and high-pressure lamps) such as environmental protection, improved energy efficiency, smaller size, advanced control capabilities, longer service time and reduced radiated heat [70, 71, 187]. In general, pc-LEDs fabricated by coupling with FR emitting Mn^{4+}-doped phosphors and other red phosphors may

exhibit an emission overlapped with the absorption spectrum of phytochromes. Such fabricated pc-LEDs can aid to control the duration of sunlight sensed by plants, which can regulate the flowering time of plants [66, 68, 188-190]. Therefore, it is of great significance to develop eco-friendly phosphors emitting red light under n-UV/blue light excitation for promoting regulated plant growth. Recently, Pr^{3+} doped red emitting materials and their application for artificial lighting in plant growth systems are applied in various fields, such as solar cells, white (w)-LEDs, fingerprint sensing, and biological imaging etc. [191-194][19–22] In particular, commercial w-LED fabricated using yellow-emitting phosphors coated on blue LED chip lacks red color component leading to its low color rendering index (CRI). It was previously demonstrated that red (600–660 nm) phosphor addition could enhance CRI of such w-LEDs [66, 195-197]. Therefore, Pr^{3+} doped proposed CBV host may be promising to fabricate w-LED with high CRI and plant growth LED.

In this report, Pr^{3+} doped calcium bismuth vanadate ($CaBiVO_5$: CBV) phosphor was synthesized by the citrate-gel method. The optimization of Pr^{3+} doping concentration, energy transfer, chromaticity coordinates, color purity and thermal stability for CBV: Pr^{3+} phosphors also have been studied in detail to probe the possibility of utilizing this phosphor in agriculture lighting applications.

6.2. Sample preparation

Pr^{3+} doped $CaBiVO_5$ phosphors were successfully synthesized by the citrate sol-gel method. All the precursors ($Ca(NO_3)_2$, $Bi(NO_3)_3$, NH_4VO_3 and Pr_6O_{11}) from Sigma Aldrich were used for synthesis. The computed amount of Pr_6O_{11} according to the required mole percentage was mixed with HNO_3 to form its nitrate solution. The detailed procedure is mentioned and displayed as a flow chart in section 2.2.3. and Fig. 2.2, respectively. All the

CBV: Pr^{3+} phosphors with varying dopant concentrations are synthesized via citrate sol-gel method and designated as listed in Table. 6.1.

Table 6.1. *Sample codes for citrate sol-gel synthesized Pr^{3+} doped $CaBiVO_5$ phosphors*

$CaBi_{1-x}VO_5$: xPr^{3+} phosphor	**Sample code**
x = 0.0 mol%	CP0
x = 0.25 mol%	CP1
x = 0.5 mol%	CP2
x = 1.0 mol%	CP3
x = 1.25 mol%	CP4
x = 1.5 mol%	CP5

6.3. Results and discussion

6.3.1 Structural Analysis

The XRD patterns for un-doped (CP0) and Pr^{3+} doped CBV samples (CP1-5) are shown in Fig. 6.1(a) along with JCPDS standardized data of $CaBiVO_5$ with card No.: 81-1775 for comparison. The diffraction peaks of un-doped and Pr^{3+} doped CBV (CP1-5) samples can be wholly matched with JCPDS card standard data of $CaBiVO_5$. No mixed-phase or diffraction peaks for any residual precursors are observed, which indicates that as-synthesized samples consist of a single orthorhombic phase of $CaBiVO_5$ and successful incorporation of Pr^{3+} ions ($R_{Pr^{3+}}$ = 0.99 Å; coordination number (CN) = 6) in CBV host by replacing Bi^{3+} ($R_{Bi^{3+}}$= 1.03 Å; CN = 6) ions are owing to the same valence state and similar ionic radii. For evaluating the lattice parameters and confirming phase purity, the structural refinement for the as-prepared CP3 phosphor was carried out at FullProf suite employing the Rietveld method. The standard values for lattice parameters and Wyckoff's positions of various atoms are served into software mentioned elsewhere [114]. The pseudo-Voigt function for simulating peak profile and the

linear interpolation amid customary background data points with adjustable heights have opted in FullProf software.

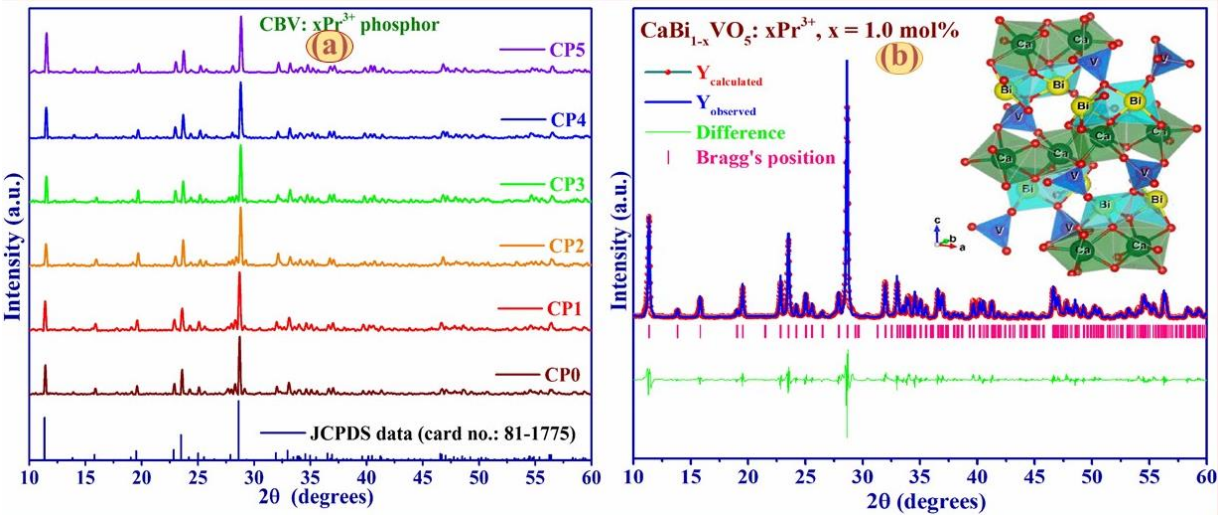

Figure 6.1. *(a) X-ray diffraction pattern of citrate sol-gel synthesized un-doped (CP0) and Pr^{3+} doped CBV samples at different Pr^{3+} concentrations (CP1- CP5) and (b) Rietveld refinement of 1.0 mol% Pr^{3+} doped CBV phosphor (CP3) (Inset: Crystal structure for CP3)*

Fig. 6.1 (b) epitomizes the calculated and experimental diffraction data as well as the difference between them. By comparing the calculated and experimental patterns, it is observed that every diffraction peak agrees well without the presence of any impurity phase, confirming the phase purity of citrate sol-gel synthesized CBV sample. The refinement analysis provides the reliability factor (R_p = 10.5 and R_{wp} = 13.8) and goodness of fit (χ^2) = 2.23 for CP3, which does not exceed the acceptable error limit and thereby suggesting the refinement results are reliable. The resultant crystallographic data and refined parameters for CP3 phosphor are summarized in Table 6.2. The crystal structure is modelled by feeding the obtained refined data of CP3 into Vesta software (inset of Fig. 6.1 (b)). The crystal structure composed of orthorhombic symmetry, having D_{15}^{2h}–Pbca space group. In the structure, vanadium (V) atoms form tetrahedrally coordinated (V^{5+}) bonds with the oxygen atom. The calcium (Ca) atoms are seven coordinated with oxygen atoms forming CaO_7 polyhedra, which are linked along edges to form layers. The three-dimensional structure is formed via asymmetrically surrounded

Bi^{3+} ions by oxygen atoms. The reckoned values of crystallite site for un-doped (CP0) and Pr^{3+} doped CBV (CP1-5) samples are 36.16, 24.02, 22.98, 22.01, 21.58 and 20.82 nm, respectively.

Table 6.2. *Refinement results for CP3 phosphor*

Sample	**CP3**
Structure	Orthorhombic
Space group	D_{15}^{2h}−Pbca
a (Å)	11.1996
b (Å)	5.4258
c (Å)	15.5515
α=β=γ	90 °
N	8
R_p	10.5
R_{wp}	13.8
χ^2	2.23
V ($Å^3$)	946.25
Density (mg/m^3)	4.99

As observed, the crystallite size decreases with the doping of Pr^{3+} ions, which may be ascribed to compression produced in unit cell volume as the smaller sized dopants are substituting the larger sized cations (Bi^{3+}) [198, 199].

6.3.2. Morphological Studies

Fig. 6.2 reveals morphology and microstructures of the citrate sol-gel synthesized 1.0 mol% Pr^{3+} doped CBV phosphor. The SEM image shows that as-prepared CBV phosphor comprising aggregation of quasi-spherically shaped particles with sizes varying in a narrow range from 0.5 to 2 μm. The surfaces of the as-synthesized microcrystalline particles are smooth and regular, which may lead to less scattering and are appropriate for coating on a LED chip to provide an intense emission [200].

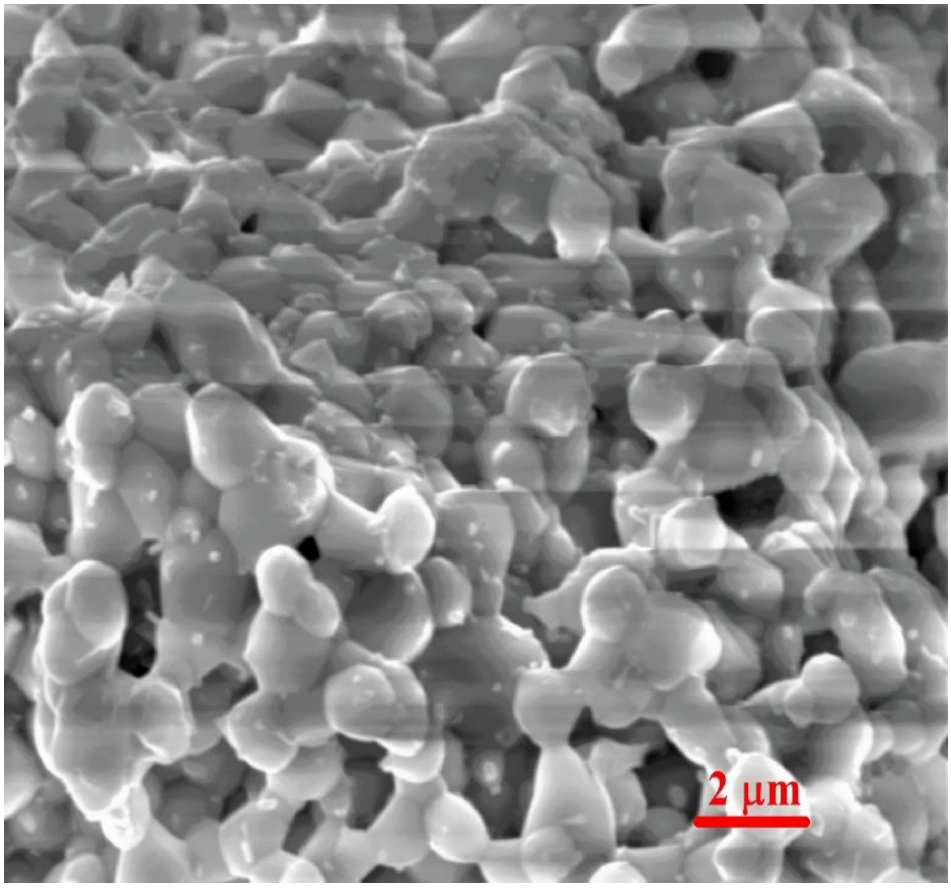

Figure 6.2. *SEM image of the citrate sol-gel synthesized 1.0 mol% Pr^{3+} doped CBV phosphor*

6.3.3. Optical properties

Fig. 6.3 shows the diffuse reflectance spectrum for 1.0 mol% Pr^{3+} doped CBV phosphor. The spectrum possesses sharp bands located at 450, 473, 490 and 608 nm due to transitions of Pr^{3+}, which will be discussed in succeeding sections.

From the plot of $[F(R_\infty)h\nu]^{1/n}$ vs. hν, the values of E_g have been reckoned by linear graphical region extended to zero [201]. In the present case, the data is plotted with the value of n = ½ (shown as the inset of Fig. 6.3) and the evaluated E_g value is found to be 3.2 eV for electronically direct allowed transitions.

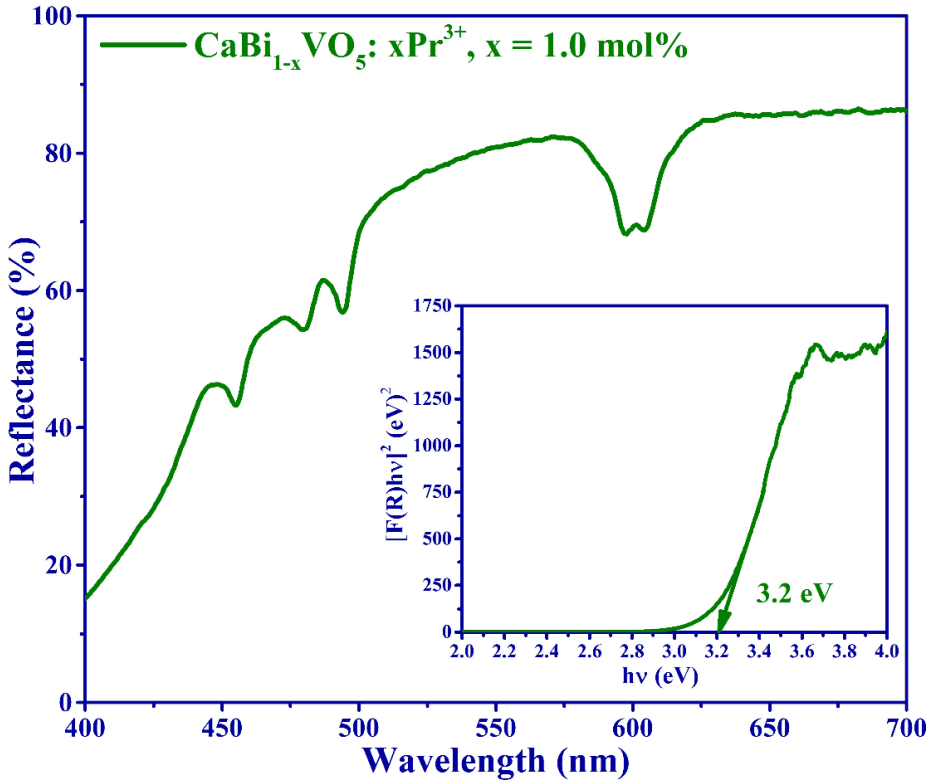

Figure 6.3. *Diffuse reflectance spectrum of 1.0 mol% Pr^{3+} doped CBV phosphor*

6.3.4. Photoluminescence properties

Fig. 6.4 represents the excitation spectrum for 1.0 mol% Pr^{3+} doped CBV phosphor monitored emission at a wavelength of 608 nm. The CBV: Pr^{3+} phosphor exhibits intense excitation at 450, 473 and 490 nm wavelengths, which can be ascribed to Pr^{3+} transitions viz. $^3H_4 \rightarrow {}^3P_2$, $^3P_1$ and $^3P_0$, respectively [202]. The most intense excitation peak is centred at 473 nm, indicating that the highest absorption is possible at this wavelength. Hence, it is selected as the excitation wavelength to pump all the CBV: Pr^{3+} phosphors. Moreover, the intense excitation bands in the blue region support the potential utilization of CBV: Pr^{3+} phosphor in fabricating InGaN (blue) LED excited pc-LEDs. Additionally, the blue-emitting InGaN chip can serve the dual purpose viz. excitation source for CBV: Pr^{3+} phosphors and a blue light supplement for plant growth.

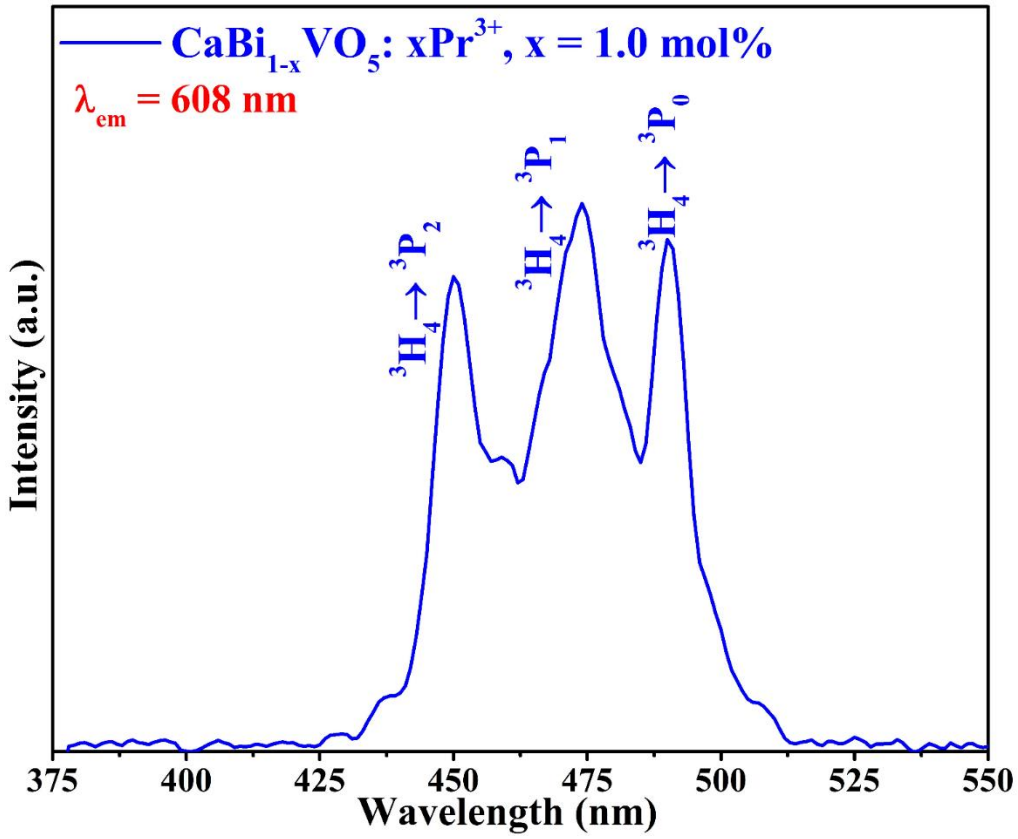

Figure 6.4. *Excitation spectrum for 1.0 mol% Pr^{3+} doped CBV phosphor monitored at 608 nm emission wavelength*

Fig. 6.5 (a) represents the emission spectra for CBV: Pr^{3+} phosphors pumped with the most intense excitation wavelength (473 nm). The emission spectra reveals various sharp bands located at 533, 547, 583, 608, 620, 656, 680, 693 nm attributed to $^3P_1 \rightarrow {}^3H_5$, $^3P_0 \rightarrow {}^3H_5$, $^3P_1 \rightarrow {}^3H_6$, $^1D_2 \rightarrow {}^3H_4$, $^3P_0 \rightarrow {}^3H_6$, $^3P_0 \rightarrow {}^3F_2$, $^3P_0 \rightarrow {}^3F_3$ and $^1D_2 \rightarrow {}^3H_5$ transitions of Pr^{3+} ions, respectively [156, 202-207]. The emission peak located at 608 nm ($^1D_2 \rightarrow {}^3H_4$) dominates among all the peaks present in the emission spectra. In the present case, there is a possibility of inhomogeneous crystal field and low symmetry around Pr^{3+} ions, which may be ascribed to minute Ca/Bi disordered ratio in the CBV lattice structure [122, 207]. The low symmetry sites around Pr^{3+} ion can mix the opposite parity into 4f configurational levels, consequently increasing the probability of $^1D_2 \rightarrow {}^3H_4$ transition of Pr^{3+} ions [122, 206]. Moreover, the emission at 656 nm is attributed to the hypersensitive $^3P_0 \rightarrow {}^3F_2$ transition of Pr^{3+} ($\Delta S = 0$, $\Delta J = 2$; S = spin angular momentum, J = total angular momentum), which is a forced

electric dipole transition, and strongly dependent on the field environment around Pr^{3+} ions [204]. Further, Fig. 6.5 (a) epitomizes the improvement in red emission intensity of CBV: Pr^{3+} phosphor with increasing concentration of Pr^{3+} ions up to 1.25 mol%.

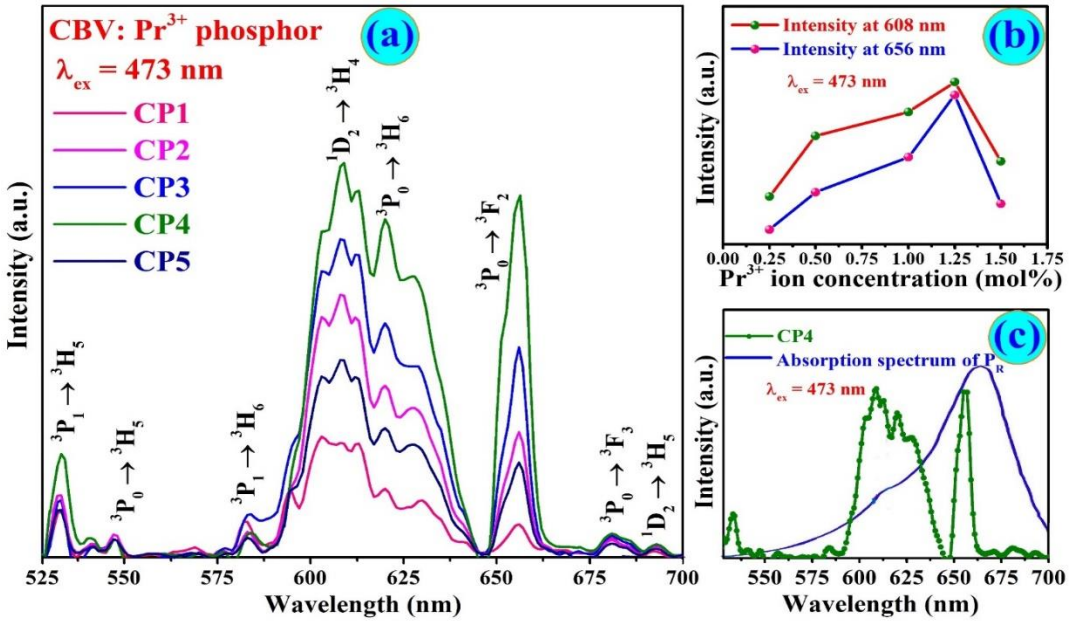

Figure 6.5. *(a) Emission spectra for CBV: Pr^{3+} phosphors under 473 nm excitation, (b) Variation of intensity at different emission wavelengths with Pr^{3+} ion concentration and (c) Spectral overlap of CBV: Pr^{3+} emission with the absorption spectrum of P_R phytochrome*

Fig. 6.5 (b) clearly shows that the emission intensity at 608 and 656 nm wavelengths under 473 nm excitation reaches a maximum at 1.25 mol% (optimized concentration) of Pr^{3+} ions and decreases contrarily with increasing Pr^{3+} concentration owing to concentration quenching phenomenon. Fig. 6.5 (c) embodies the emission of Pr^{3+} doped CBV phosphor overlapping the absorption spectrum of P_R phytochromes, which stimulate crucial processes in plants such as germination of seeds, flower induction, unrolling of leaves and so on. Aforementioned findings clearly indicate that Pr^{3+} doped CBV phosphor has favorable characteristics to be utilized in indoor agricultural pc-LEDs.

Further, to explore the reason for concentration quenching, the theory given by G. Blasse has been referred [208]. According to it, the luminescence quenching ensued from increased probability of non-radiative energy transfers between activators located in proximity

at higher concentrations. The concentration quenching may happen via either exchange interaction or multipolar interaction, which apparently depends on critical distance (R_c). In the present case, using $X_c = 0.0125$, the R_c is reckoned to be 26.24 Å. The evaluated value of R_c is far greater than 5 Å, discarding the possibility of exchange interaction. Subsequently, energy transfer can only be considered via multipolar interaction. The mentioned interaction between activators ions can possibly be of electric dipolar-dipolar (d-d), dipolar-quadrupolar (d-q) and quadrupolar-quadrupolar (q-q) type. For the present case, log (I/x) values as a function of log (x) are plotted and linear fitted (Fig. 6.6), which provide the slope value to be 1.99.

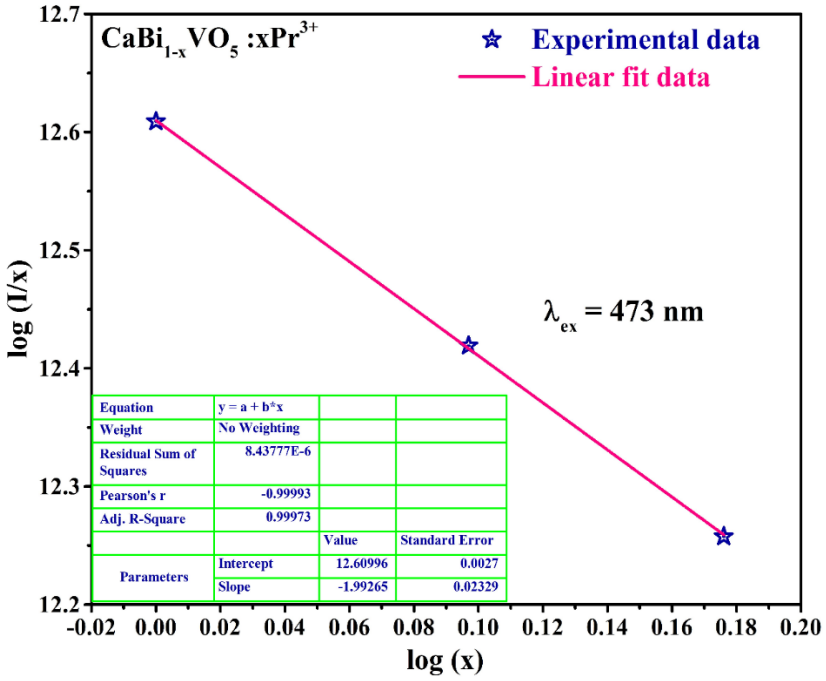

Figure 6.6. *Dexter's plot for Pr^{3+} ions in CBV phosphor*

Using the slope value, the value of Q has been evaluated to be 5.97, which discloses that the concentration quenching in CBV: Pr^{3+} phosphors is via dipole-dipole interaction. Fig. 6.7 represents the energy level (EL) diagram to illustrate the excitation, emission and possible non-radiative pathways in Pr^{3+} doped CBV phosphors. The incident light on CBV: Pr^{3+} phosphor pump Pr^{3+} ions from the ground state ($^3H_4$) to the higher existing state ($^3P_1$) (process: ①). Then, Pr^{3+} ions at $^3P_1$ energy state non-radiatively (process: ②) relaxed to the emitting level $^1D_2$. Eventually, Pr^{3+} ion doped in CBV lattice provide emission (process: ③)

in the visible region at 533 ($^3P_1 \rightarrow {}^3H_5$), 547 ($^3P_0 \rightarrow {}^3H_5$), 583 ($^3P_1 \rightarrow {}^3H_6$), 608 ($^1D_2 \rightarrow {}^3H_4$), 620 ($^3P_0 \rightarrow {}^3H_6$), 656 ($^3P_0 \rightarrow {}^3F_2$), 680 ($^3P_0 \rightarrow {}^3F_3$) and 693 nm ($^1D_2 \rightarrow {}^3H_5$) wavelengths, respectively. Moreover, there are three possible pathways for relaxations, including phonon-assisted NR transitions between $^3P_0$ and $^1D_2$ (NR) and cross-relaxation channels (CR1: $^3P_0 + {}^3H_4 \rightarrow {}^3H_6 + {}^1D_2$ and CR2: $^3P_0 + {}^3H_4 \rightarrow {}^1D_2 + {}^3H_6$)[195]. Apart from this, there is another possible cross relaxation channel namely CR3: $^1D_2 + {}^3H_4 \rightarrow {}^1G_4 + {}^3F_4$. All the possible cross relaxations are represented as process ④ in Fig. 6.7.

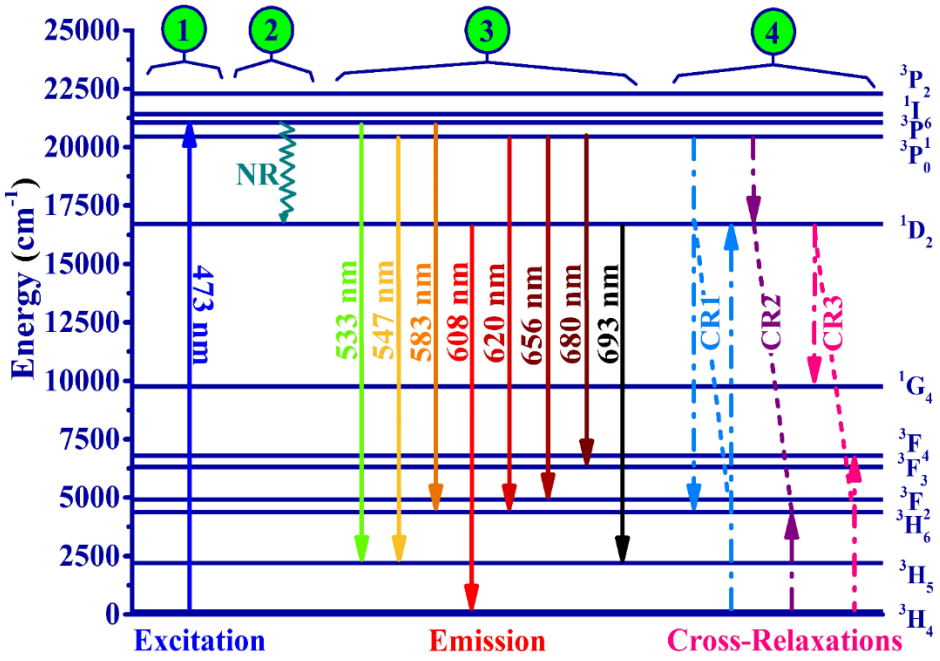

Figure 6.7. *Partial energy level diagram for Pr^{3+} ion doped CBV phosphor*

6.3.5. Chromaticity properties

The Commission International de I' Eclairage (CIE) 1931 parameters such as chromaticity coordinates (x, y) and color correlated temperature (CCT) can be computed using the emission spectral data to realize the colorimetric properties of the phosphor. The evaluated values of chromaticity coordinates (x, y) are denoted on the CIE 1931 diagram to reveal the color tone of the emission. The chromaticity coordinates for all as-prepared Pr^{3+} doped CBV phosphors for emission data for obtained 473 nm excitation wavelength have been enlisted in

Table 6.3. Fig. 6.8 represents the chromaticity coordinates (0.660, 0.339) marked in the CIE 1931 chromaticity diagram for the optimized Pr^{3+} doped CBV (CP4) phosphor excited with 473 nm wavelength located in the red region.

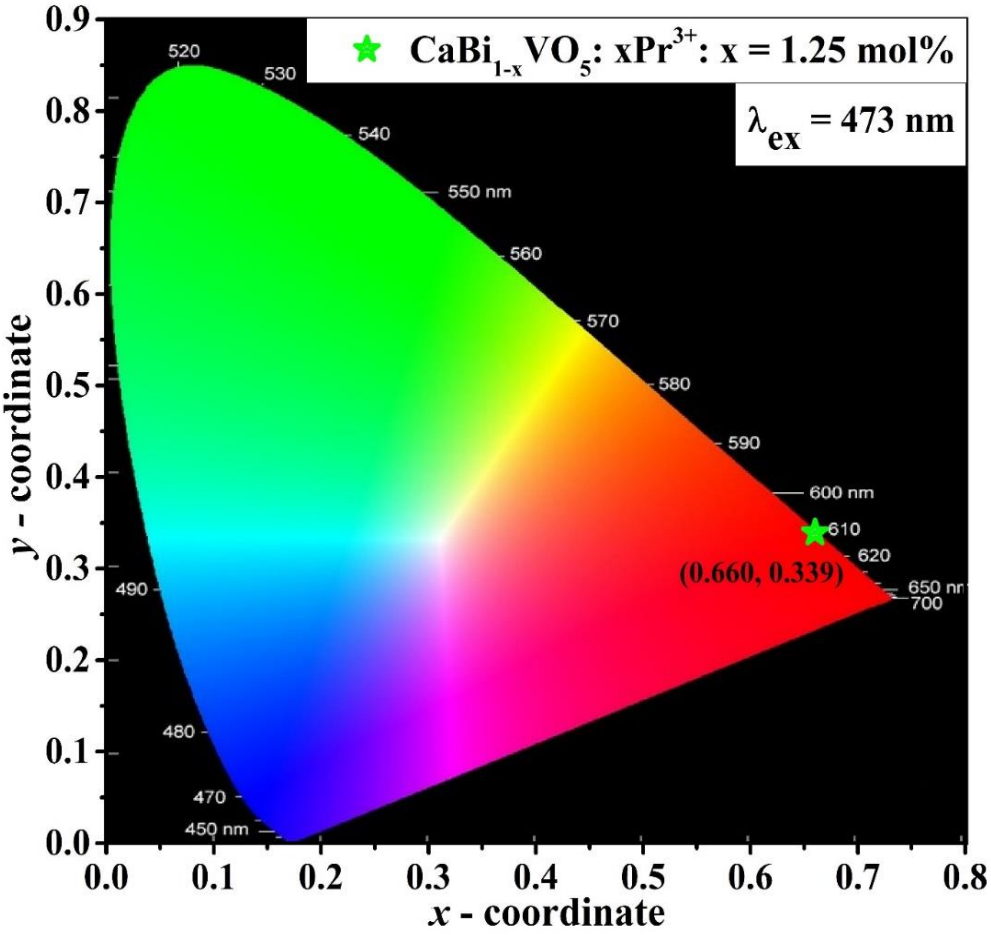

Figure. 6.8. *CIE chromaticity diagram for the optimized CBV: Pr^{3+} phosphor*

The calculated chromaticity coordinates of Pr^{3+} doped CBV phosphor are found proximal to the red-emitting commercial phosphor Y_2O_2S: Eu^{3+} coordinates (x= 0.622 and y= 0.351) and the CIE coordinates standardized by National Television Standard Committee (NTSC) (i.e. x = 0.670, y = 0.330). The calculated CCT value is 3043 K for emission data measured for λ_{ex} = 473 nm for CP4 phosphor. The CCT values for all the as-synthesized samples have been listed in Table 6.3. Moreover, the evaluated color purity for the CP4 phosphor under 473 nm excitation is 99.70 %. The color purity value indicates that CBV: Pr^{3+}

phosphors emit highly pure red light under blue light excitation. Thus, the computed colorimetric properties demonstrate the potential utility of optimized CBV: Pr^{3+} phosphor as a red component in blue light excited w-LEDs to utilize for agricultural lighting.

Table 6.3. *CIE coordinates, CCT and lifetime values for Pr^{3+} doped CBV phosphors*

Sample	CIE coordinates (x, y)	CCT values (K)	Lifetime (μs)
CP1	(0.602, 0.393)	1732	22.64
CP2	(0.611, 0.385)	1778	22.39
CP3	(0.642, 0.356)	2323	22.13
CP4	(0.660, 0.339)	3043	21.37
CP5	(0.629, 0.367)	2031	20.41

6.3.6. Thermal stability

Among major essential requisites for phosphors to be applicable in LED applications, sustaining the emission intensity even at higher temperatures is also an essential requirement. For investigating the viability of 1.25 mol% Pr^{3+} doped CBV phosphor for LED application, the PL measurement under 473 nm excitation is done in 303-463 K temperature range and shown in Fig. 6.9 (a). Fig. 6.9 (b) (shown as inset) represents temperature dependence of the relative intensity for CBV: Pr^{3+} phosphors at 608 nm under 473 nm excitation with respect to the intensity at 303 K. Fig. 6.9 (a&b) conspicuously speaks that the emission intensity of CBV: Pr^{3+} phosphor at 608 nm under 473 nm excitation manifests a decreasing trend with a rise in temperature owing to thermal quenching phenomenon. Furthermore, the graph between $\ln[(I_O/I_T) - 1]$ and $1/k_BT$ (Fig. 6.9 (c)) for the $^1D_2 \rightarrow {}^3H_4$ transition in CBV: Pr^{3+} phosphor is a linear graph with slope 0.2166, which provide the value of activation energy (ΔE_a). The

obtained value of ΔE_a (0.2166 eV) demonstrate the better thermal stability of the CBV: Pr^{3+} phosphor than the Pr^{3+} doped phosphors reported earlier [209-210].

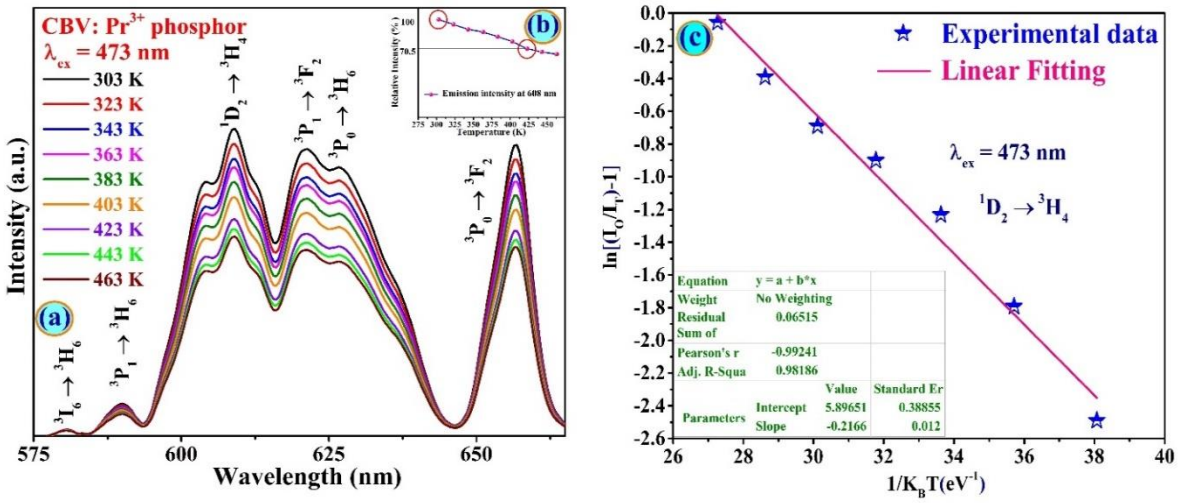

Figure 6.9. *(a) Temperature dependent PL for optimized CBV: Pr^{3+} phosphor under 473 nm excitation (b) Emission intensity at 608 nm wavelength for CP4 phosphor with varying temperature and (c) Graph between $ln(I_O/I_T\text{-}1)$ and $1/K_BT$*

6.4. Conclusions

The present work elucidates the synthesis of the pure phase CBV: Pr^{3+} phosphors via citrate sol-gel method. The XRD analysis provided the single phase confirmation of $CaBiVO_5$ with an orthorhombic crystal structure as the obtained patterns demonstrate full agreement with the JCPDS standardized data (card no:81-1775). The SEM result manifests quasi-spherical shape with size falling in a narrow range (0.5 to 2 µm) for CBV: Pr^{3+} phosphors synthesized via citrate sol-gel method beneficial for better coating over LED chip. The excitation spectrum observed by monitoring emission at 608 nm exhibit an intense band in the blue spectral region. The CBV: Pr^{3+} phosphors under blue light excitation exhibit intense red emission at 608, 620 and 656 nm wavelengths. The emission spectrum of CBV: Pr^{3+} phosphor is demonstrated to be overlapping with the absorption of P_R phytochrome. Moreover, the Pr^{3+} concentration dependence on emission intensity reveals that the maximum emission intensity is achieved at

1.25 mol% concentration of Pr^{3+} in CBV lattice, beyond which there is a decrease in emission intensity caused by concentration quenching. The Dexter's theory employed on emission data indicates the d-d multipolar interaction between neighbouring Pr^{3+} ions at higher concentration, which is the potential reason for concentration quenching. The CIE coordinates for the optimized CBV: Pr^{3+} phosphor (0.660, 0.339) occupy pure red region of CIE 1931 diagram and found proximal to the red emitting commercial phosphor Y_2O_2S: Eu^{3+} (0.622, 0.351) as well as NTSC standard values (0.670, 0.330). Also, the temperature dependent emission spectral data demonstrate admirable thermal stability for the as-synthesized phosphor. Based on duly mentioned studies, thermally stable deep red emitting CBV: Pr^{3+} phosphors have great potential to utilize for plant growth and white LED application.

Chapter 7
Summary and future scope

This chapter summarizes the relevant conclusions and present status of the research work. The general outcomes of the thesis are focused on the development of thermally stable new vanadate based phosphors with improved multi-color and white light emission by effective excitation via UV/n-UV and blue light for solid state lighting applications. The developed phosphors exhibit emission properties in spectral range pre-requisite for w-LEDs and agricultural lighting. The scope of the future research work is also discussed in this chapter.

7.1. Summary of the work

The main emphasis of this thesis work is to synthesize and characterize RE ions doped CaBiVO5 phosphor to be utilized in solid state lighting applications for general illumination and indoor plant cultivation system. Multicolor (orange, red, deep-red, white light) emitting pure phase CBV phosphors were successfully synthesized via solid state reaction (SSR), combustion (CB) and citrate sol-gel (SG) methods by incorporating Sm^{3+}, Eu^{3+}, Pr^{3+} and Dy^{3+} ions) as dopants. Significant attention towards the enhancement in emission properties has been investigated via varying synthesis technique, increasing dopant concentrations and co-doping.

As discussed in the previous chapters, the overwhelming interest in pc-LEDs has been perceived recently due to their idiosyncratic properties such as improved energy efficiency, longevity, eco-friendliness and captivating luminescence features. Such sophisticated pc-LEDs have found versatile applications in display devices, safety signals, bio-sensors, bio-medical treatments and artificial lighting for general illumination as well as controlled plant growth [211]. In this regard, new phosphor with improved luminescent features need to be developed. Pursuing the above mentioned motivation for developing new phosphors and extensive investigation on its structural, morphological and photo-luminescent properties, single phase Eu^{3+} doped CBV phosphors synthesized successfully by SSR method to achieve intense and pure red emission under 464 nm excitation. As-obtained intense red light emitting phosphor can be coupled with blue and green phosphors to achieve multi-phase white light emission under excitation of UV/n-UV LED. Alternatively, the Eu^{3+} doped CBV phosphor can be co-doped with commercial YAG: Ce^{3+} phosphor and coated over blue (InGaN) chip to develop high CRI and low CCT w-LEDs as commercial red phosphor exhibit poor chemical stability and poor absorption [212]. It is pertinent to mention that as-prepared Sm^{3+} ion doped CBV phosphors also exhibit intense red emission which is reported rarely in other research papers. Therefore, to select best option for red emitting phosphor in terms of better emission and color-

purity, Sm^{3+} doped CBV phosphors have been prepared via SSR method. Furthermore, other synthesis methods like combustion (CB) and citrate sol-gel (SG) methods were employed to optimize the synthesis method for CBV phosphor. The optimized synthesis process is observed as citrate sol-gel method by analysing the structural, morphological and luminescent properties. The improved morphology and significant luminescence enhancement was observed in citrate sol-gel synthesized CBV phosphor in comparison with other methods. Further, for single phase phosphor to generate white light, Dy^{3+} doped and Dy^{3+}/Eu^{3+} co-doped CBV phosphors (accomplishing the pre-requisite property of efficient spectral overlap between Dy^{3+} emission and Eu^{3+} excitation) were synthesized via citrate sol-gel method. In addition, Pr^{3+} doped CBV phosphors have been synthesized for its multifunctional applications in w-LEDs and agricultural lighting particularly for the sensitization of the phytochromes (P_R) present in the plants. All these results allow us to conclude that calcium bismuth vanadate doped with different RE ions is a potential candidate for its utility in w-LEDs and agricultural lighting applications

7.1.1. Important findings

The thermal analysis of un-sintered $CaBiVO_5$ powder was accomplished to analyse its crystallization temperature. The pure phase orthorhombic $CaBiVO_5$ has been synthesized via solid state reaction (SSR) method. The crystallization of CBV phosphor began beyond 750 °C. Therefore, these samples were sintered at 950 °C to achieve pure phase of $CaBiVO_5$ in SSR method. Moreover, the single phase formation of $CaBiVO_5$ phosphor has been achieved via different synthesis routes such CB and SG method. The sintering temperature has reduced to 850 and 800 °C during CB and SG method, respectively. The XRD patterns for all the prepared samples were in complete agreement with the standard JCPDS card no. 81-1775 signifies the pure phase formation with orthorhombic structure. The structural properties of differently synthesized CBV phosphors doped with various RE ions were investigated to analyse

crystallinity, phase purity, crystallite size and existing strain using XRD technique. Also Rietveld refinement calculations on observed XRD data have been performed to confirm phase purity. The morphological analysis of RE doped $CaBiVO_5$ was accomplished by recording SEM images. Among the three synthesis methods discussed in the previous chapters, SSR, and CB methods show irregular agglomerated particles and SG synthesized phosphors shows homogeneous regular morphology of particles.

Moving forward to the photoluminescence properties of the RE doped $CaBiVO_5$ phosphors, the salient features of the current thesis are summarized as:

The excitation spectra for $CaBi_{1-x}VO_5$: xEu^{3+} (x = 1.0-6.0 mol%) shows various excitation bands located in UV, n-UV and blue region. Due to the presence of self-luminescent vanadate host, the excitation spectra is extended over UV/n-UV range (220-385 nm). The PL spectra display distinct and intense red emission centred at 613 nm wavelength due to $^5D_0 \rightarrow {}^7F_2$ transition of Eu^{3+} for all the $CaBi_{1-x}VO_5$: xEu^{3+} (x = 1.0 - 6.0 mol%) phosphors, when excited with n-UV and blue light. While under host excitation, a weak band approximately centred at 542 nm attributed to CBV host is observed along with sharp Eu^{3+} emission peaks. The host to Eu^{3+} energy transfer under host excitation enables CBV: Eu^{3+} phosphor to exhibit attractive color tunability by varying Eu^{3+} ion concentration under host excitation. The concentration quenching phenomenon has been observed due to which luminescence intensity decreases beyond 4.0 mol% concentration (optimized) of Eu^{3+} ions. The CIE chromaticity coordinates (0.640, 0.354) of the optimized Eu^{3+} doped CBV phosphor excited under 464 nm wavelength are found to be close with commercial red phosphor Y_2O_2S: Eu^{3+} (x= 0.622 and y= 0.351) and with the coordinates designated by NTSC. The PL decay study reveals the single and bi-exponential behaviour of the decay curves with decay time in micro-second range. All the above mentioned results, support CBV: Eu^{3+} phosphor's utilization as a potential red emitting phosphor in lighting applications.

The study of optical properties via diffuse reflectance spectrum provides the band gap (E_g) values to be 3.04 and 3.17 eV for un-doped and Sm^{3+} doped CBV phosphor, respectively. Further, the PL studies have been done to characterize the luminescent properties of CBV: Sm^{3+} phosphors. The excitation spectra measured by monitoring emission at 649 nm ($^4G_{5/2} \rightarrow {}^6H_{9/2}$: Sm^{3+} transition) for CBV: Sm^{3+} phosphors reveal significant absorption in ultraviolet (UV), near (n)-UV and blue spectral regions. The comparative photoluminescence (PL) spectra measured under n-UV (343 nm) excitation for differently synthesized CBV: Sm^{3+} phosphors exhibit significantly enhanced emission intensity for SG derived phosphor than other adopted methods. The PL spectra for SG derived 1.0 mol% Sm^{3+} doped CBV phosphor at λ_{ex} = 275 and 343 nm exhibit sharp peaks located at 566 ($^4G_{5/2} \rightarrow {}^6H_{9/2}$), 606 ($^4G_{5/2} \rightarrow {}^6H_{9/2}$) and 649 nm ($^4G_{5/2} \rightarrow {}^6H_{9/2}$) along with the weak host emission broadband and for λ_{ex} = 406 nm ($^6H_{5/2} \rightarrow {}^4F_{7/2}$: Sm^{3+} transition), similar sharp peaks of Sm^{3+} transitions are observed without any host emission. Unlike mostly explored Sm^{3+} doped phosphors, emission peak in red spectral region (649 nm) is more intense as compared to the emission peak in orange region (599 nm) in the present work. The concentration quenching phenomenon is observed beyond 2.0 mol% Sm^{3+} concentration due to electric dipole-dipole interaction between Sm^{3+} ions in proximity as revealed by Dexter's theory and I–H model. The CBV: Sm^{3+} phosphors manifest color tunability from orange to orange-red region by modulating excitation from 275 nm (0.567, 0.404) to 343 nm (0.591, 0.399) and finally to 406 nm (0.620, 0.376). The CIE coordinates under λ_{ex} = 275 nm (0.567, 0.404) and λ_{ex} = 343 nm (0.591, 0.399) are found close to Nichia corporation fabricated amber LED NSPAR 70BS (0.570, 0.420). The lifetime values for $^4G_{5/2}$ level have been calculated with varying concentrations in CBV phosphors and found to be in microseconds (μs) range at λ_{ex} = 343 nm. The temperature-dependent PL studies indicate appreciable thermal stability of the as-prepared phosphor. The emission intensity of 2.0 mol% doped CBV phosphor has retained 85.2% at 443 K of its initial

value at 323 K. Above mentioned results suggest that CBV: Sm^{3+} phosphor has great potential for use in white light-emitting diode (w-LED) applications.

For single phase white light emission, a set of Dy^{3+} activated and Dy^{3+}/Eu^{3+} bi-activated CBV phosphors were prepared successfully via citrate sol-gel technique. The emission spectra for Dy^{3+} activated CBV phosphor observed for different excitations exhibit intense blue and yellow emission bands due to $^4F_{9/2} \rightarrow {}^6H_J$ (J = 15/2 and 13/2, respectively) Dy^{3+} transitions. The Dy^{3+} concentration has been optimized as 4.0 mol%, beyond which the emission declines due to concentration quenching. For Dy^{3+}/Eu^{3+} co-doped CBV phosphors, emission color tunability observed from greenish-yellow to red via white region by controlling co-dopant concentration and excitation wavelength. The decay plots for Dy^{3+}/Eu^{3+} co-doped CBV phosphors are most accurately fitted with bi-exponential equations and reveal a reduction in lifetime values (for $^4F_{9/2}$ level) with a rise in concentrations of Eu^{3+} ion. Based on the Dexter theory & Reisfeld's approximation, dipolar-dipolar interaction is identified to be accountable for Dy^{3+} to Eu^{3+} energy transfer in CBV phosphors. All these outcomes illustrate that the Dy^{3+} singly doped and Dy^{3+}/Eu^{3+} doubly doped CBV phosphor is a potential candidate for w-LEDs and smart display devices.

Moreover, pure phase CBV: Pr^{3+} phosphors with orthorhombic crystal structure synthesized successfully via citrate sol-gel method for agricultural lighting application as confirmed by XRD analysis. The CBV: Pr^{3+} phosphors under blue light excitation exhibit intense red emission at 608 nm ($^1D_2 \rightarrow {}^3H_4$), 620 nm ($^3P_0 \rightarrow {}^3H_6$) and 656 nm ($^3P_0 \rightarrow {}^3F_2$) wavelengths. The emission spectrum of optimized (CBV: xPr^{3+}, x = 1.25 mol%) phosphor is demonstrated to be overlapping with the absorption of P_R phytochrome. The CIE coordinates for the optimized CBV: Pr^{3+} phosphor (0.660, 0.339) occupy pure red region of CIE 1931 diagram and found proximal to the red emitting commercial phosphor Y_2O_2S: Eu^{3+} (0.622, 0.351) as well as NTSC standard values (0.670, 0.330). Based on duly mentioned studies,

thermally stable CBV: Pr^{3+} phosphors have great potential for their utilization in LED applications for plant growth and white light emission.

All the above-mentioned significant outcomes confirm that RE doped/co-doped $CaBiVO_5$ phosphors developed in the thesis accomplish their potential utility for w-LEDs and agricultural lighting applications.

7.2. Future scope of the work

- To enhance the luminescence properties for suitable RE^{3+} doped $CaBiVO_5$ phosphor using suitable fluxes (for ex: NH_4X, NaX and KX etc., where X = halides)
- To explore other synthesis methods such as hydrothermal method to improve the particle morphology, reduce the particle size to nano-regime which in turn further may improve the luminescence properties
- To extend the utility of this phosphor for versatile applications such as agricultural lighting, solar cells, thermal and fingerprint sensing etc.
- To fabricate prototype pc-LEDs using optimized phosphor for the above mentioned applications

References

[1] C.C. Lin, A. Meijerink, R.-S. Liu, J. Phys. Chem. Lett. 7 (2016) 495–503.

[2] M. Shang, C. Li, J. Lin, Chem. Soc. Rev. 43 (2014) 1372–1386.

[3] D. Macisaac, G. Kanner, G. Anderson, Phys. Teach. 37 (1999) 520–525.

[4] G. Annadurai, S.M. Moses, V. Sivakumar, Superlattices Microstruct. 93 (2016) 57–66.

[5] C. Ronda, Luminescence From Theory to Applications, WILEY-VCH Verlag GmbH & Co. KGaA, Weinheim, 2008, 1-3.

[6] G. Blasse, Philips Res. 24 (1969) 131–144.

[7] K. Binnemans, Chem. Rev. 109 (2009) 4283–4374.

[8] C.N. Banwell, Fundamentals of Molecular Spectroscopy, Third Ed., McGraw-Hill International (UK) Limited, 1972, 238.

[9] C. Parker, W.T. Rees, RSC Adv. 87 (1962) 83–111.

[10] N. Hafsi, H. Bouridah, Optik (Stuttg). 168 (2018) 244–252.

[11] H. Xu, Q. Sun, Z. An, Y. Wei, X. Liu, Coord. Chem. Rev. 293–294 (2015) 228–249.

[12] L.V.S. França, L.C. Oliveira, O. Baffa, Meas. J. Int. Meas. Confed. 134 (2019) 492– 499.

[13] M. Koshimizu, T. Yanagida, K. Shinsho, S. Yanagisawa, Y. Fujimoto, H. Yagi, T. Yanagitani, K. Asai, Nucl. Instruments Methods Phys. Res. Sect. B Beam Interact. with Mater. Atoms 435 (2018) 285–289.

[14] N. Siraj, B. El-zahab, S. Hamdan, T.E. Karam, L.H. Haber, M. Li, S.O. Fakayode, S. Das, B. Valle, R.M. Strongin, G. Patonay, H.O. Sintim, G.A. Baker, A. Powe, M. Lowry, J.O. Karolin, C.D. Geddes, I.M. Warner, Anal. Chem. 88 (2016) 170–202.

[15] B.C. Lima, L.A. Gómez-Malagón, A.S.L. Gomes, J.A.M. Garcia, L.R.P. Kassab, J. Electron. Mater. 46 (2017) 6750–6755.

[16] Y. Zhao, L. Wondraczek, A. Mermet, M. Peng, Q. Zhang, J. Qiu, Opt. Express 23 (2015) 12423.

[17] S. W. S. Mckeever, Thermoluminescence of solids, Cambridge Solid State Science Series, Cambridge University Press, 1985, 1-19.

[18] T. Jüstel, H. Nikol, C. Ronda, Angew. Chemie - Int. Ed. 37 (1998) 3084–3103.

[19] B.L. Abrams, P.H. Holloway, Chem. Rev. 104 (2004) 5783–5802.

[20] F. Wang, X. Liu, Chem. Soc. Rev. 38 (2009) 976.

[21] L. Zhang, Y. Xia, X. Shen, W. Wei, Mater. Res. Express 4 (2017) 075201.

[22] X. Cheng, D. Guo, S. Feng et al., Opt. Mater. 49 (2015) 32-38.

[23] H. Zhang, X. Fu, S. Niu et al., Solid State Comm. 132 (2004) 527-531.

[24] C.J. Summers, B. Wagner, H. Menkara, Proc. Third Int. Conf. Solid State Light. 5187 (2004) 123–132.

[25] K. Li, M. Shang, H. Lian, J. Lin, J. Mater. Chem. C 4 (2016) 5507–5530.

[26] S. V Eliseeva, J.-C.G. Buenzli, Chem. Soc. Rev. 39 (2010) 189–227.

[27] X. Huang, S. Han, W. Huang, X. Liu, Chem. Soc. Rev. 42 (2013) 173–201.

[28] B. Tian, B. Chen, Y. Tian, X. Li, J. Zhang, J. Sun, H. Zhong, L. Cheng, S. Fu, H. Zhong, Y. Wang, X. Zhang, H. Xia, R. Hua, J. Mater. Chem. C 1 (2013) 2338–2344.

[29] John A. DeLuca, J. Chem. Educ. 57 (1980) 541.

[30] A.E. Hughes, J. Phys. Colloques 28 (1967) C4-55 – C4-65.

[31] S. Ye, F. Xiao, Y.X. Pan, Y.Y. Ma, Q.Y. Zhang, Mater. Sci. Eng. R: Repts. 71 (2010) 1-34.

[32] J. Solé, L. Bausa, D. Jaque, An Introduction to the Optical Spectroscopy of Inorganic Solids, John Wiley & Sons 2005, 181-183.

[33] A. Ruivo, V.S.F. Muralha, H. Águas, A.P. de Matos, C.A.T. Laia, J. Quant. Spectrosc. Radiat. Transf. 134 (2014) 29–38.

[34] D.R. Dreyer, S. Park, C.W. Bielawski, R.S. Ruoff, Chem. Soc. Rev. 39 (2010) 189–227.

[35] S. Saha, S. Das, U.K. Ghorai, N. Mazumder, D. Ganguly, K.K. Chattopadhyay, J. Phys. Chem. C 119 (2015) 16824–16835.

[36] M. V Dacosta, S. Doughan, Y. Han, U.J. Krull, Anal. Chim. Acta 832 (2014) 1–33.

[37] A. Kalaji, M. Mikami, A.K. Cheetham, Chem. Mater. 26 (2014) 3966–3975.

[38] M. De Jong, D. Biner, K.W. Kra, L. Seijo, J. Phys. Chem. Lett. 7 (2016) 2730–2734.

[39] M.P. Hehlen, M.G. Brik, K.W. Krämer, J. Lumin. 136 (2013) 221–239.

[40] Y. Zhang, W. Gong, G. Ning, New J. Chem. 40 (2016) 10136–10143.

[41] M. Hatanaka, S. Yabushita, Theor. Chem. Acc. 133 (2014) 1517–1531.

[42] J. Sucher, Reports Prog. Phys. 41 (1978) 1781–1837.

[43] J.G. Bu, S. V Eliseeva, Basics of Lanthanide Photophysics, Springer, Berlin, Heidelberg, 2010, Chapter 2.

[44] S. V Eliseeva, J.-C.G. Bünzli, Chem. Soc. Rev. 39 (2010) 189–227.

[45] J. Mckittrick, M.E. Hannah, A. Piquette, J.K. Han, J.I. Choi, M. Anc, M. Galvez, H. Lugauer, J.B. Talbot, K.C. Mishra, ECS J. Solid State Sci. Technol. 2 (2013) 3119– 3131.

[46] N.C. George, K.A. Denault, R. Seshadri, Annu. Rev. Mater. Res. 43 (2013) 481–501.

[47] P. Dorenbos, J. Lumin 111 (2005) 84-104.

[48] L. Yang, Y. Wan, Y. Huang, C. Chen, H. Jin, J. Alloys Compd. 684 (2016) 40–46.

[49] B. Tian, B. Chen, Y. Tian, X. Li, J. Zhang, J. Sun, H. Zhong, L. Cheng, S. Fu, H. Zhong, Y. Wang, X. Zhang, H. Xia, R. Hua, J. Mater. Chem. C 1 (2013) 2338–2344.

[50] J.C.G. Bünzli, C. Piguet, Chem. Soc. Rev. 34 (2005) 1048–1077.

[51] Y. Il Jeon, L. Krishna Bharat, J.S. Yu, J. Alloys Compd. 620 (2015) 263–268.

[52] W.P. Lustig, F. Wang, S.J. Teat, Z. Hu, Q. Gong, J. Li, Inorg. Chem. 55 (2016) 7250–7256.

[53] T. Suehiro, ACS Appl. Mater. Interfaces 3 (2011) 811–816.

[54] Y. Wei, L. Cao, L. Lv, G. Li, J. Hao, J. Gao, C. Su, Chem. Mater. Mater. 30 (2018) 2389–2399.

[55] C. Grieco, K.F. Hirsekorn, A.T. Heitsch, A.C. Thomas, M.H. Mcadon, B.A. Vanchura, M.M. Romanelli, L.L. Brehm, A. Leugers, A.N. Sokolov, J.B. Asbury, ACS Appl. Mater. Interfaces 9 (2017) 12547–12555.

[56] J. Du, D. Xu, X. Gao, S. Ji, H. Li, J. Sun, Optik (Stuttg). 147 (2017) 290–299.

[57] H. Yu, D. Deng, D. Zhou, W. Yuan, Q. Zhao, Y. Hua, J. Mater. Chem. C 3 (2013) 5577–5582.

[58] Y. Chang, C. Liang, S. Yan, Y. Chang, J. Phys. Chem. C 3 (2010) 3645–3652.

[59] C. Chiu, C. Liu, S. Huang, T.-M. Chen, J. Electrochem. Soc. 154 (2007) J181–J184.

[60] P. Rekha Rani, M. Venkateswarlu, S. Mahamuda, K. Swapna, N. Deopa, A.S. Rao, J. Alloys Compd. 787 (2019) 503–518.

[61] N. Guo, Y. Huang, H. You, M. Yang, Y. Song, K. Liu, Y. Zheng, Inorg. Chem. 49 (2010) 10907–10913.

[62] E. Darko, P. Heydarizadeh, MR Sabzalian, Philos Trans R Soc B., 369 (2014) 2013–2020.

[63] A. Agarwal, SD. Gupta Curr Biotechnol, 5 (2016) 28–43.

[64] G. Tamulaitis, P. Duchovskis, Z. Bliznikas, *et al*, J. Phys D Appl Phys., 38 (2005) 3182–3187.

[65] Y. Zhang, Y. Huang, M. Li, et al, J. Am Ceram Soc., 43 (2020) 4373–4383.

[66] A. Zhang, M. Jia, Z. Sun, et al., J. Alloys Compd. 782 (2019) 203–208.

[67] Z. Zhou, J. Zheng, R. Shi, et al., Appl. Mater. Interfaces 9 (2017) 6177–6185.

[68] J. Xiang, J. Chen, N. Zhang, H. Yao, C. Guo, Dye Pigment 154 (2018) 257–262.

[69] D. Huang, P. Dang, X. Xiao, et al., New J. Chem. 44 (2020) 6132–6172.

[70] RC. Morrow, LED lighting in horticulture. HortScience. 43 (2008) 1947–1950.

[71] M. Xia, S. Gu, C. Zhou, et al., RSC Adv. 9 (2019) 9244–9252.

[72] X. Huang, H. Guo, Ceram Int. 44 (2018) 10340–10344.

[73] H. Kaur, M. Jayasimhadri, Ceram Int. 45 (2019) 15385–15393.

[74] V.B. Pawade, H.C. Swart, S.J. Dhoble, Renew. Sustain. Energy Rev. 52 (2015) 596– 612.

[75] Y. Zhang, D. Geng, X. Li, J. Fan, K. Li, H. Lian, M. Shang, J. Lin, J. Phys. Chem. C 118 (2014) 17983–17991.

[76] U. Caldiño, A. Lira, A.N. Meza-Rocha, I. Camarillo, R. Lozada-Morales, J. Lumin. 194

(2018) 231–239.

[78] V. Uma, K. Maheshvaran, K. Marimuthu, G. Muralidharan, J. Lumin. 176 (2016) 15– 24.

[79] K. Li, V. R. Deun, Dye Pigment. 155 (2018) 258–264.

[80] R. Singh, S. J. Dhoble, Bull Mater Sci. 34 (2011) 557–562.

[81] H. Chen, J. Zhou, H. Zhang, Z. Hu, Opt Mater (Amst). 89 (2019) 132–137.

[82] D. Song, C. Guo, T. Li, Ceram Int. 41 (2015) 6518–6524.

[83] C. Zhang, J. Lin, Chem. Soc. Rev. 41 (2012) 7938–7961.

[84] H. Terraschke, C. Wickleder, Chem. Rev. 115 (2015) 11352–11378.

[85] R.K. Tamrakar, D.P. Bisen, N. Brahme, J. Radiat. Res. Appl. Sci. 7 (2014) 550–559.

[86] C.C. Lin, R. Liu, J. Phys. Chem. Lett. 2 (2011) 1268–1277.

[87] S. Som, S. Das, S. Dutta, H.G. Visser, M.K. Pandey, P. Kumar, R.K. Dubey, S.K. Sharma, RSC Adv. 5 (2015) 70887–70898.

[88] Z.M. Chen, S.X. Jiang, R.H. Guo, B.J. Xin, D.G. Miao, Mater. Technol. Adv. Perform. Mater. 29 (2014) 198–203.

[89] T. Qian, B. Fan, H. Wang, S. Zhu, Chem. Phys. Lett. 715 (2019) 34–39.

[90] J.K. Han, J.I. Choi, A. Piquette, M. Hannah, M. Anc, M. Galvez, J.B. Talbot, J. Mckittrick, ECS J. Solid State Sci. Technol. 2 (2013) 3138–3147.

[91] A.E. Danks, S.R. Hall, Z. Schnepp, Mater. Horizons 3 (2016) 91–112.

[92] G. Paul, Principles and Applications of Thermal Analysis, Ist editio, Blackwell, 2008.

[93] B.D. Cullity, M. Cohen, Elements of X-RAY DIFFRACTION, 2nd ed., Addison Wesley Publishing Company Inc., 1978.

[94] S. Amelinckx, Wiley InterScience (Online service), Electron Microscopy : Principles and Fundamentals, VCH, 1997, Chapter 2.

[95] W. Zhou, Z.L. Wang, eds., Scanning Microscopy for Nanotechnology, Springer New York, New York, NY, 2007, Chapter 1.

[96] R.W. Frei, H. Zeitlin, C R C Crit. Rev. Anal. Chem. 2 (1971) 179–246.

[97] J.R. Lakowicz, Principles of Fluorescence Spectroscopy, Springer, 2006, 27-61.

[98] G. G. Guilbault, Fluorescence, theory, instrumentation and practice published by Marcel Dekker, Inc., New Yo.

[99] J. McKittrick, L.E. Shea-Rohwer, J. Am. Ceram. Soc. 97 (2014) 1327–1352.

[100] T. Takeda, R.J. Xie, T. Suehiro, N. Hirosaki, Prog. Solid State Chem. 51 (2018) 41–51.

[101] K. Jha, A.K. Vishwakarma, M. Jayasimhadri, D. Haranath, J. Alloys Compd. 719 (2017) 116–124.

[102] P. Pust, V. Weiler, C. Hecht, A. Tücks, A.S. Wochnik, A.K. Henb, D. Wiechert, C. Scheu, P.J. Schmidt, W. Schnick, Nat. Mater. 13 (2014) 891–896.

[103] B.V. Ratnam, M. Jayasimhadri, K. Jang, Spectrochim. Acta - Part A Mol. Biomol. Spectrosc. 132 (2014) 563–567.

[104] I. Ahemen, Dilip, K. De, A.N. Amah, Appl. Phys. Res. 6 (2014) 95–108.

[105] S. Nakamura, Mater. Res. Bull. 22 (1997) 29–35.

[106] G. Blasse, M.G.J. van Leur, Mater. Res. Bull. 20 (1985) 1037–1045.

[107] G. Blasse, A. Bril, Appl. Phys. Lett. 11 (1967) 53–55.

[108] J.S. Kim, P.E. Jeon, Y.H. Park, J.C. Choi, H.L. Park, G.C. Kim, T.W. Kim, Appl. Phys. Lett. 85 (2004) 3696–3698.

[109] R. Saraf, C. Shivakumara, S. Behera, H. Nagabhushana, N. Dhananjaya, RSC Adv. 5 (2015) 4109–4120.

[110] S.K. Mahesh, P.P. Rao, M. Thomas, T.L. Francis, P. Koshy, Inorg. Chem. 52 (2013) 13304–13313.

[111] V.R. Bandi, B.K. Grandhe, K. Jang, H.S. Lee, D.S. Shin, S.S. Yi, J.H. Jeong, J. Alloys Compd. 512 (2012) 264–269.

[112] S. Neeraj, N. Kijima, A.. Cheetham, Chem. Phys. Lett. 387 (2004) 2–6.

[113] S. Kaur, M. Jayasimhadri, A.S. Rao, J. Alloys Compd. 697 (2017) 367–373.

[114] J. Boje and Hk.Muller-bushbaum, Zeitschrift Fur Anorg. Und Allg. Chemie. 619 (1993) 521–524.

[115] A.K. Vishwakarma, M. Jayasimhadri, J. Lumin. 176 (2016) 112–117.

[116] V. Mote, Y. Purushotham, B. Dole, J. Theor. Appl. Phys. 6 (2012) 6-13.

[117] A.N. Mallika, A.R. Reddy, K.S. Babu, C. Sujatha, K.V. Reddy, Opt. Mater. (Amst). 36 (2014) 879–884.

[118] S. Muthukumaran, R. Gopalakrishnan, Opt. Mater. (Amst). 34 (2012) 1946–1953.

[119] L. Qin, D.L. Wei, Y. Huang, C. Qin, P. Cai, S. Il Kim, H.J. Seo, Mater. Chem. Phys. 147 (2014) 1195–1203.

[120] H. Ronde and G.Blasse, J. Inorg. Nucl. Chem. 40 (1978) 215–219

[121] X. Huang, H. Guo, Dye. Pigment. 154 (2018) 82–86.

[122] Z. Pei, A. van Dijken, A. Vink, G. Blasse, J. Alloys Compd. 204 (1994) 243–246

[123] W.T. Carnall, P.R. Fields, K. Rajnak, J. Chem. Phys. 49 (1968) 4450.

[124] Z. Zhu, Z. Guo, Z. Sun, Z. Wu, L. Zhou, X. Zhang, Ceram. Int. 44 (2018) 16514–16521.

[125] F. Wang, C. Liu, Z. Zhou, P. Jia, J. Lin, J. Rare Earths. 30 (2012) 202–204.

[126] Y. Li, X. Wei, H. Chen, G. Pang, Y. Pan, L. Gong, L. Zhu, G. Zhu, Y. Ji, J. Lumin. 168 (2015) 124–129.

[127] A.K. Parchur, R.S. Ningthoujam, RSC Adv. 2 (2012) 10859–10868.

[128] A.K. Vishwakarma, K. Jha, M. Jayasimhadri, A.S. Rao, K. Jang, B. Sivaiah, D. Haranath, J. Alloys Compd. 622 (2015) 97–101.

[129] G. Blasse, J. Chem. Phys. 46 (1967) 2583–2585.

[130] L. Zhang, H. Zhong, X. Li, L. Cheng, L. Yao, J. Sun, J. Zhang, R. Hua, B. Chen, Phys. B Condens. Matter. 407 (2012) 68–72.

[131] L.G. Van Uitert, , J. Electrochem. Soc. 114 (1967) 1048–1053.

[132] D.L. Dexter, J. Chem. Phys. 21 (1953) 836–850.

[133] Q. Xu, J. Sun, D. Cui, Q. Di, J. Zeng, J. Lumin. 158 (2015) 301–305.

[134] T. Hasegawa, Y. Abe, A. Koizumi, T. Ueda, K. Toda, M. Sato, 57 (2018) 857-866

[135] H.J. Woo, S. Gandhi, M. Jayasimhadri, D.S. Shin, H.S. Lee, K. Jang, Sensors Actuators, B Chem. 241 (2017) 1106–1110.

[136] C.S. McCamy, coordinates, Color Res. Appl. 17 (1992) 142–144.

[137] S. Gai, P. Yang, D. Wang, C. Li, N. Niu, F. He, X. Li, CrystEngComm. 13 (2011) 5480–5487.

[138] Z.H. Ju, R.P. Wei, J.X. Ma, C.R. Pang, W.S. Liu, J. Alloys Compd. 507 (2010) 133–136.

[139] S. Kaur, A.S. Rao, M. Jayasimhadri, J. Lumin. 202 (2018) 461–468.

[140] Y.H. Kim, N.S.M. Viswanath, S. Unithrattil, H.J. Kim, W. Bin Im, ECS J. Solid State

Sci. Technol. 7 (2018) R3134–R3147.

[141] U. Farooq, Z. Zhao, Z. Sui, C. Gao, R. Dai, Z. Wang, Z. Zhang, J. Alloys Compd. 778 (2019) 942–950.

[142] X. Mi, J. Sun, P. Zhou, H. Zhou, D. Song, K. Li, M. Shang, J. Lin, J. Mater. Chem. (2015) 4471–4481.

[143] B. Guo, Z.W. Zhang, D.G. Jiang, Y.N. Li, X.Y. Sun, J. Lumin. 206 (2019) 244–249.

[144] A.K. Vishwakarma, K. Jha, M. Jayasimhadri, Opt. Mater. (Amst). 96 (2019) 109301.

[145] A. Singh, H.L. Vishwakarma, Mater. Sci. Pol. 33 (2015) 751–759.

[146] S.S. Pitale, M. Gohain, I.M. Nagpure, O.M. Ntwaeaborwa, B.C.B. Bezuidenhoudt, H.C. Swart, Phys. B Condens. Matter 407 (2012) 1485–1488.

[147] P. Pookmanee, S. Kojinok, S. Phanichphant, J. Met. Mater. Miner. 22 (2012) 49–53.

[148] N. Kaczorowska, A. Szczeszak, S. Lis, J. Lumin. 200 (2018) 59–65.

[149] T. Thirugnanam, J. Nanomater. 2013 (2013) 1-7.

[150] S. Mavengere, J.S. Kim, Appl. Surf. Sci. 444 (2018) 491–496.

[151] X. Zhang, Z. Zhu, Z. Guo, F. Mo, Z. chao Wu, Dye. Pigment. 156 (2018) 67–73.

[152] B.Y. Huang, B.L. Feng, L. Luo, C.L. Han, Y.T. He, Z.R. Qiu, 212 (2016) 71–77.

[153] T. Srikumar, Ch. Srinivasa Rao, Y. Gandhi, N. Venkatramaiah, V. Ravikumar, N. Veeraiah, J. Phys. Chem. Solids 72 (2011) 190-200.

[154] J. Huang, A.W. Sleight, J. Solid State Chem. 97 (1992) 228–232.

[155] Y. Ruangtaweep, P. Yasaka, J. Kaewkhao, Mater. Today Proc. 5 (2018) 10984–10989.

[156] W.T. Carnall, P.R. Fields, K. Rajnak, J. Chem. Phys. 49 (1968) 4424–4442.

[157] L.A. Jacob, S. Sisira, K. Thomas, D. Alexander, P.R. Biju, N.V. Unnikrishnan, C. Joseph, J. Solid State Chem. 280 (2019) 120998.

[158] S. Kaur, A.S. Rao, M. Jayasimhadri, B. Sivaiah, D. Haranath, J. Alloys Compd. 802 (2019) 129–138.

[159] K. V. Dabre, S.J. Dhoble, RSC Adv. 5 (2015) 60409–60418.

[160] W. Zhang, Y. Zhang, S. Ouyang, Z. Zhang, H. Xia, Mater. Lett. 160 (2015) 459–462.

[161] A. Hermann, D. Friedrich, T. Zschekel, C. Russel, J. Lumin. 214 (2019) 116550.

[162] J.C.G. Bünzli, C. Piguet, Chem. Soc. Rev. 34 (2005) 1048–1077.

[163] D.K. Singh, J. Manam, Appl. Phys. A Mater. Sci. Process. 124 (2018) 1–15.

[164] J. Sun, D. Cui, J. Am. Ceram. Soc. 97 (2014) 843–847.

[165] L. Mei, H. Liu, L. Liao, Y. Zhang, R.V. Kumar, Sci. Rep. 7 (2017) 3–10.

[166] I. Charak, M. Manhas, A. K. Bedyal, S. Singh, A. Srivastava, H. C. Swart, V. Kumar, J. Alloys Compds. 869 (2021) 159363.

[167] X. Huang, J. Liang, S. Rtimi, B. Devakumar, Z. Zhang Chem. Eng. J. 405 (2021) 126950.

[168] D. Prakashbabu, H. B. Ramalingam, R. Hari Krishna, B. M. Nagabhushana, C. Shivakumara, K. Munirathnam, S. Ponkumar, J. lumin. 192 (2017) 496-503.

[169] K. H. Kwon, W. B. Im, H. S. Jang, H. S. Yoo, D. Y. Jeon, Inorg. Chem. 48 (2009) 11525–11532.

[170] L. Zhao, D. Wang, C. Chen, Y. Wang, Mater. Res. Bull. 70 (2015) 817–821.

[171] A. M. Kłonkowski, W. Wiczk, K. Szczodrowski, D. Wileńska, N. Górecka, M. Szyszkowska, J. Alloys Compd. 705 (2017) 539–549.

[172] D. Wileńska, K. Szczodrowski, S. Mahlik, B. Kukliński, M. Grinberg, A.M. Kłonkowski, J. Lumin. 166 (2015) 54–59.

[173] X. F. Wang, Q. Yang, G. G. Wang, X. Z. Wang, J. C. Han, RSC Adv. 5 (2015) 92988–92994.

[174] H. Guan, Y. Sheng, C. Xu, Y. Dai, X. Xie, H. Zou, Phys. Chem. Chem. Phys. 18 (2016) 19807–19819.

[175] R. S. Yadav, Monika, E. Rai, L. P. Purohit, S. B. Rai, J. Lumin. 217 (2020) 116810.

[176] M. Vijayakumar, K. Marimuthu, J. Lumin. 178 (2016) 414–424.

[177] P. Ghosh, A. Kar, and A. Patra, J. Appl. Phys. 108 (2010) 113506.

[178] Z. Yang, H. Dong, X. Liang, C. Hou, L. Liu, F. Lu, Dalton Trans. 43 (2014) 11474-11477.

[179] H. Guan, Y. Song, P. Ma, M. Chang, J. Chen, Y. Wang, B. Yuan, H. Zou, RSC Adv. 6 (2016) 53444–53453.

[180] J. L. Fry, H. H. Caspers, H. E. Rast, S. A. Miller, J. Chem. Phys. 48 (1968) 2342–2348.

[181] P. Karthikeyan, S. Arunkumar, K. Annapoorani, K. Marimuthu, Spectrochim. Acta - Part A Mol. Biomol. Spectrosc. 193 (2018) 422–431.

[182] P. Du, J.S. Yu, J. Alloys Compd. 653 (2015) 468–473.

[183] Y. Li, X. Wei, H. Chen, et al., J. Lumin 168 (2015) 124-129.

[184] X. Wu, Y. Jiao, O. Hai, Q. Ren, F. Lin, H. Li, J. Alloys Compds. 730 (2018) 521-527.

[185] G. V. Lokeshwara Reddy, L. Rama Moorthy, P. Packiyaraj, B. C. Jamaliah, Opt. Mater. 35 (2013) 2138-2145

[186] E. Darko, P. Heydarizadeh, MR. Sabzalian, Philos Trans R Soc B. 369 (2014) 2013–2020.

[187] X. Li Chen, X. Z. Xue, W. Z. Xue, et al. Sci Hortic (Amsterdam). 200 (2016) 111–118.

[188] S. Wang, Y. Xu, T. Chen, et al. Chem Eng J. 3 (2020) 125912.

[189] T. Jishi, K. Kimura, R. Matsuda, K. Fujiwara, Sci Hortic (Amsterdam). 198 (2016) 227–232.

[190] L. Shi, Y. J. Han, Z. X. Ji, J. Lumin. 218 (2020) 116828.

[191] D. Xu, P. Yu, L. Tian, J. Rare Earths. 36 (2018) 243–247.

[192] N. Deopa, AS. Rao, S. Mahamuda, et al., J. Alloys Compd. 708 (2017) 911–921.

[193] H. Seong, W. Bin, D. Chin, D. Young, S. Surk, J. Lumin. 126 (2007) 371–377.

[194] Z. Zhou, N. Zhang, J. Chen, X. Zhou, MS. Molokeev, C. Guo, J. Ind Eng Chem. 65 (2018) 411–417.

[195] P. Du, JS. Yu, Dye Pigment. 147 (2017) 16–23.

[196] J. Chen, Z. Ma, Y. Sua, et al., Optica. 6 (2019) 1244-1246.

[197] Q. Lu, J. Li, D. Wang, Curr Appl Phys. 13 (2013) 1506–1511.

[198] A. Nakrela, N. Benramdane, A. Bouzidi, Z. Kebbab, M. Medles, C. Mathieu, Results Phys. 6 (2016) 133–138.

[199] GL. Pearson, J. Bardeen, Phys Rev. 75 (1949) 865–883.

[200] Deepali, R. Bisi, Vandana, H. Kaur, M. Jayasimhadri, J. Mater Sci Mater Electron. 32 (2021) 1650-1658.

[201] V. Singh, M. Seshadri, MS. Pathak, N. Singh, Spectrochim Acta Part A Mol Biomol

Spectrosc. 217 (2019) 315–321.

[202] D. Peng, H. Sun, X. Wang, J. Zhang, M. Tang, X. Yao, Mater. Sci. Eng. B 176 (2011) 1513–1516.

[203] HR. Shih, KT. Liu, LG. Teoh, LK. Wei, YS. Chang, Microelectron Eng. 148 (2015) 10-13.

[204] L. Li, HY. Wu, J. Alloys Compd. 702 (2017) 106–119.

[205] S. Zhang, Y. Hu, L. Chen, G. Ju, T. Wang, Z. Wang, RSC Adv. 5 (2015) 37172–37179.

[206] L. Angelini, M. Inês, B. Bernardi, A. Mesquita, Scr Mater. 157 (2018) 15–18.

[207] D. V. R. Murthy, BC Jamalaiah, T. Sasikala, et al., 405 (2010) 1095–1100.

[208] H. Sun, Q. Zhang, X. Wang, Y. Zhang Ceram Int. 40 (2014) 15669–15675.

[209] K. Fiaczyk, S. Omagari, A. Meijerink, A. Zych, J. Lumin. 198 (2018) 63-170.

[210] P. Li, M. Peng, X. Yin, Z. Ma, G. Dong, Q. Zhang, et al, Opt Express. 21 (2013) 18943-18948.

[211] C.H. Huang, T.M. Chen, Inorg. Chem. 50 (2011) 5725–5730.

[212] Q. Cheng, F. Ren, Q. Lin, H. Tong, X. Miao, J. Alloys Compd. 772 (2018) 905–911.